ATLAS CONF Note
ATLAS-CONF-2019-005
March 20, 2019

Combined measurements of Higgs boson production and decay using up to 80 fb^{-1} of proton–proton collision data at $\sqrt{s} = 13$ TeV collected with the ATLAS experiment

The ATLAS Collaboration

Combined measurements of Higgs boson production cross sections and branching fractions are presented. The combination is based on the analyses of the Higgs boson decay modes $H \to \gamma\gamma$, ZZ^*, WW^*, $\tau\tau$, $b\bar{b}$, $\mu\mu$, searches for decays into invisible final states, and on measurements of off-shell Higgs boson production. Up to 79.8 fb^{-1} of proton–proton collision data collected at $\sqrt{s} = 13$ TeV with the ATLAS detector are used. Results are presented for the gluon fusion and vector-boson fusion processes, and for associated production with vector bosons or top quarks. The combined measurement yields an observed (expected) significance for the vector-boson fusion production process of 6.5σ (5.3σ). This single-experiment observation follows an earlier observation in the combination of ATLAS and CMS measurements. Measurements in kinematic regions defined within the simplified template cross section framework are also shown. The results are interpreted in terms of modifiers applied to the Standard Model couplings of the Higgs boson to other particles, and are used to set exclusion limits on parameters in two Higgs doublet models and in the simplified Minimal Supersymmetric Standard Model. No significant deviations from Standard Model predictions are observed.

ATLAS-CONF-2019-005
21 March 2019

1 Introduction

Following the discovery of the Higgs boson H by the ATLAS [1] and CMS [2] experiments, its properties have been probed using proton–proton (pp) collision data produced by the Large Hadron Collider (LHC) at CERN. The coupling properties of the Higgs boson to other Standard Model (SM) particles, such as its production cross sections in pp collisions and decay branching ratios, can be precisely computed within the SM, given the value of the Higgs boson mass. Measurements of these properties can therefore provide stringent tests of the validity of the SM.

Higgs boson production and decay rates have been determined using the Run 1 dataset, through the combination of ATLAS and CMS measurements [3]. More recently, these measurements have been extended using the Run 2 dataset recorded by the ATLAS detector during 2015, 2016 and 2017, using up to 79.8 fb^{-1} of proton–proton collision data produced by the LHC. They include analyses targeting the $H\to\gamma\gamma$ and $H\to ZZ^*\to 4\ell$[1] decay channels following the same methodology as the ones presented respectively in Ref. [4] and Ref. [5], with improved selections for Higgs boson production in association with a top–antitop pair, described in Ref. [6]; analyses targeting the $H \to WW^*$ [7] and $H \to \tau\tau$ [8] decay channels; analyses targeting $H \to b\bar{b}$ in associated production with a weak vector boson $V = W$ or Z (VH) [9, 10] and in the weak vector-boson fusion (VBF) production process [11]; two analyses targeting associated production with a top–antitop pair ($t\bar{t}H$) [6, 12, 13]; an analysis targeting the $H \to \mu\mu$ decay channel following the same methodology as presented in Ref. [14], applied to the larger 2015–2017 input dataset; three analyses targeting Higgs decays to invisible final states [15–17]; and an analysis targeting off-shell production of Higgs bosons [18]. This note presents measurements of Higgs boson properties at $\sqrt{s} = 13$ TeV obtained in the combination of these results, using similar techniques as in Ref. [3]. A Higgs boson mass value of $m_H = 125.09$ GeV, corresponding to the central value of the combination of ATLAS and CMS measurements in Run 1 [19], is used for SM predictions. The uncertainty on the measured Higgs boson mass is considered in the $H\to\gamma\gamma$ and $H\to ZZ^*\to 4\ell$ analyses. Similar measurements [20–24], as well as their combination [25], have been reported by the CMS collaboration.

All the input analyses except for those targeting $H \to \mu\mu$ and the VBF, $H \to b\bar{b}$ processes use a parameterization of the Higgs boson signal yields based on the Stage 1 simplified template cross section (STXS) framework [26, 27] described in Section 6.1. These cross sections are defined in the fiducial region $|y_H| < 2.5$, where y_H is the Higgs boson rapidity, partitioned within each Higgs boson production process into multiple kinematic regions based on the transverse momentum of the Higgs boson, the number of associated jets, and the transverse momentum of associated W or Z bosons. The analyses targeting $H \to \mu\mu$ and VBF, $H \to b\bar{b}$ use a coarser description based on the Higgs boson production mode only.

The note is structured as follows: Section 2 describes the data and simulation samples and Section 3 presents the analyses in individual decay channels which are used as inputs to the combination. Section 4 provides a short description of the statistical procedures. The measurement of the signal strength μ, defined as the ratio of the total Higgs boson signal yield to its SM prediction, is presented in Section 5.1. Measurements of the cross sections of the main production processes within $|y_H| < 2.5$, assuming SM predictions for the branching ratios, are then shown in Section 5.2. The production modes considered are gluon fusion (ggF), VBF, VH, $t\bar{t}H$ and associated production with a single top quark (tH). Measurements of cross sections times branching ratios for Higgs boson production and decay processes are shown in Section 5.3. Section 5.4 presents a parametrization where the measured quantities are the cross section times branching ratio of the process $gg \to H \to ZZ^*$, together with ratios of production cross sections

---

[1] Throughout the note ℓ denotes the light leptons e and μ.

and ratios of branching fractions. Common systematic uncertainties and modeling assumptions partially cancel in these ratios, reducing the model dependence of the result. Section 6 presents results in the STXS framework. Potential deviations from SM predictions are then probed in a framework of multiplicative modifiers κ applied to the SM values of Higgs boson couplings [28], presented in Section 7. Finally, Section 8 presents an interpretation of the data within two benchmark models of beyond the SM (BSM) phenomena. Indirect limits on model parameters are set following a methodology similar to that of Ref. [29]. Section 9 summarizes the results.

2 Data and simulated samples

The results of this note are based on proton–proton collision data collected by the ATLAS experiment[2] [30, 31] in 2015, 2016 and 2017, with the LHC operating at a center-of-mass energy of 13 TeV. The integrated luminosities of the datasets used in each analysis are shown in Table 1. The analyses are described in Section 3.

Table 1: Integrated luminosity of the dataset used for each input analysis to the combination.

Analysis	Integrated luminosity (fb^{-1})
$H \to \gamma\gamma$ (including $t\bar{t}H$, $H \to \gamma\gamma$)	79.8
$H \to ZZ^* \to 4\ell$ (including $t\bar{t}H$, $H \to ZZ^* \to 4\ell$)	79.8
$H \to WW^* \to e\nu\mu\nu$	36.1
$H \to \tau\tau$	36.1
VH, $H \to b\bar{b}$	79.8
VBF, $H \to b\bar{b}$	24.5 – 30.6
$H \to \mu\mu$	79.8
$t\bar{t}H$, $H \to b\bar{b}$ and $t\bar{t}H$ multilepton	36.1
$H \to$ invisible	36.1
Off-shell $H \to ZZ^* \to 4\ell$ and $H \to ZZ^* \to 2\ell 2\nu$	36.1

The simulated Higgs boson samples used to describe the signal processes are described below. For each Higgs boson decay mode, the branching fraction used corresponds to the higher-order state-of-the-art theoretical calculations [26]. The simulated background samples vary channel by channel and are described in the individual references for the input analyses.

Most analyses use a consistent set of Higgs boson signal samples which is described in the following paragraphs. Exceptions thereto are the VBF, $H \to b\bar{b}$ and off-shell production analyses, described in Sections 3.5 and 3.9 respectively, and the measurements targeting decays of the Higgs boson to invisible final states described in Section 3.8. The samples used for these analyses are described separately at the end of this section.

---

[2] ATLAS uses a right-handed coordinate system with its origin at the nominal interaction point (IP) in the centre of the detector and the z-axis along the beam pipe. The x-axis points from the IP to the centre of the LHC ring, and the y-axis points upwards. Cylindrical coordinates (r, ϕ) are used in the transverse plane, ϕ being the azimuthal angle around the z-axis. The pseudorapidity is defined in terms of the polar angle θ as $\eta = -\ln\tan(\theta/2)$. Angular distance is measured in units of $\Delta R \equiv \sqrt{(\Delta\eta)^2 + (\Delta\phi)^2}$.

Higgs boson production via gluon fusion is simulated using the Powheg Box [32–35] NNLOPS implementation [36, 37]. The event generator uses HNNLO [38] to reweight the inclusive Higgs boson rapidity distribution produced by the next-to-leading order (NLO) generation of $pp \rightarrow H +$ parton, with the scale of each parton emission determined using the MiNLO procedure [39]. The PDF4LHC15 [40] parton distribution functions (PDFs) are used for the central prediction and uncertainty. The sample is normalized such that it reproduces the total cross section predicted by a next-to-next-to-next-to-leading-order ($\mathrm{N^3LO}$) QCD calculation with NLO electroweak corrections applied [26, 41–44]. The NNLOPS generator reproduces the Higgs boson p_T distribution predicted by the next-to-next-to-leading-order (NNLO) plus next-to-next-to-leading logarithm (NNLL) calculation of Hres2.3 [45], which includes the effects of top- and bottom-quark masses and uses dynamical renormalization and factorization scales.

The VBF production process is simulated to NLO accuracy in QCD using the Powheg Box [46] generator with the PDF4LHC15 set of PDFs. The sample is normalized to an approximate-NNLO QCD cross section with NLO electroweak corrections applied [26, 47–49].

The $qq \rightarrow VH$ production processes are simulated to NLO accuracy in QCD using Powheg Box, GoSam [50] and MiNLO [51, 52] generators with the PDF4LHC15 set of PDFs. The samples are normalized to cross sections calculated at NNLO in QCD with NLO electroweak corrections [53, 54]. The $gg \rightarrow ZH$ process is generated only at leading order (LO), using Powheg Box and NLO PDFs and normalized to an NLO computation with next-to-leading-logarithm (NLL) corrections [26, 55].

Higgs boson production in association with a top–antitop pair is simulated at NLO accuracy in QCD using the Powheg Box generator with the PDF4LHC15 set of PDFs for the $H\rightarrow\gamma\gamma$ and $H\rightarrow ZZ^*\rightarrow 4\ell$ decay processes. For other Higgs boson decays, the MadGraph5_aMC@NLO [56] generator is used with the NNPDF3.0 [57] set of PDFs. In both cases the sample is normalized to a calculation with NLO QCD and electroweak corrections [26, 58–61].

In addition to the primary Higgs boson processes, separate samples are used to model lower-rate processes. Higgs boson production in association with a bottom–antibottom pair ($b\bar{b}H$) is simulated using MadGraph5_aMC@NLO [62] with NNPDF2.3LO PDFs and is normalized to a cross section calculated to NNLO in QCD [26, 63–65]. The sample includes the effect of interference with the ggF production mechanism. Higgs boson production in association with a single top quark and a W boson (tHW) is produced at LO accuracy using MadGraph5_aMC@NLO with the CTEQ6L1 PDF set [66]. Finally, Higgs boson production in association with a single top quark in the t-channel (tHq) is generated at LO accuracy using MadGraph5_aMC@NLO with CT10 [67] PDFs. The tH samples are normalized to NLO QCD calculations [26, 68].

The parton-level events are input to Pythia8 [69] or Herwig++ [70] to model the Higgs boson decay, parton showering, hadronization, and multiple parton interaction (MPI) effects. The generators are interfaced to Pythia8 for all samples except tHW. For Pythia8 the AZNLO and A14 parameter sets [71] are used, and for Herwig++ its UEEE5 parameter set is used.

In the all-hadronic channel of the VBF, $H \rightarrow b\bar{b}$ analysis, the Powheg Box generator with the CT10 [67] set of PDFs is used to simulate the ggF [72] and VBF production processes, and interfaced with Pythia8 for parton shower. In the photon channel of the VBF, $H \rightarrow b\bar{b}$ analysis, VBF and ggF production in association with a photon is simulated using the MadGraph5_aMC@NLO generator with the PDF4LHC15 set of PDFs, and also using Pythia8 for parton shower. For both channels, contributions from VH and $t\bar{t}H$ production are generated using the Pythia8 generator with the NNPDF3.0 set of PDFs, and using the MadGraph5_aMC@NLO generator interfaced with Herwig++ and the NLO CT10 set of PDFs, respectively.

In the analyses targeting Higgs boson decays to invisible final states, the ggF, VBF and ZH signals are simulated in a similar way to the general procedure described above, but for VBF production process the NNPDF3.0 PDF set is used instead of PDF4LHC15, while for the ZH process the CT10 PDF set is used.

In the off-shell production analysis, the $gg \to H^* \to ZZ$ process is generated together with the corresponding irreducible continuum production, using the Sherpa 2.2.2 + OpenLoops [73–76] generator and the NNPDF3.0 PDF set. The generation is performed at leading order with up to one additional jet in the final state, and interfaced with the Sherpa parton shower [77]. The cross section calculations take into account K-factors following the methodology described in Ref. [18].

The particle-level Higgs boson events are passed through a Geant 4 [78, 79] simulation of the ATLAS detector [80] and reconstructed using the same analysis software as used for the data. Event pileup is included in the simulation by overlaying inelastic proton–proton collisions, such that the average number of interactions per bunch crossing reproduces that observed in the data. The inelastic proton–proton collisions are simulated with Pythia8 using the MSTW2008lo [81] set of PDFs with the A2 [82] set of tuned parameters.

3 Individual channel measurements

Brief descriptions of the input analyses to the combination are given below. More details can be found in the individual analysis references listed in each section. The categorization is summarized in Table 2. The overlap between the event selections of the analyses included in the combination is found to be negligible.

Table 2: Summary of the signal regions entering the combined measurements. Each 0-jet and 1-jet $H \rightarrow WW^*$ entry corresponds to two categories for a leading lepton flavor of either e or μ. For $H \rightarrow \tau\tau$, each entry corresponds to 3 categories for $\tau_{\mathrm{lep}}\tau_{\mathrm{lep}}$, $\tau_{\mathrm{lep}}\tau_{\mathrm{had}}$ and $\tau_{\mathrm{had}}\tau_{\mathrm{had}}$, unless otherwise specified. "Multilepton" refers to decays of the Higgs boson with one or more leptons, and encompasses $H \rightarrow WW^*$, $H \rightarrow \tau\tau$, and $H \rightarrow ZZ^*$ excluding $H \rightarrow ZZ^* \rightarrow 4\ell$. The selections targeting $H \rightarrow \mu\mu$, $H \rightarrow$ invisible and off-shell Higgs boson production are not included this table.

	$H \rightarrow \gamma\gamma$	$H \rightarrow ZZ^*$	$H \rightarrow WW^*$	$H \rightarrow \tau\tau$	$H \rightarrow b\bar{b}$
$t\bar{t}H$	$t\bar{t}H$ leptonic (3 categories) $t\bar{t}H$ hadronic (4 categories)	$t\bar{t}H$ multilepton 1 ℓ + 2 τ_{had} $t\bar{t}H$ multilepton 2 opposite-sign ℓ + 1 τ_{had} $t\bar{t}H$ multilepton 2 same-sign ℓ (categories for 0 or 1 τ_{had}) $t\bar{t}H$ multilepton 3 ℓ (categories for 0 or 1 τ_{had}) $t\bar{t}H$ multilepton 4 ℓ (except $H \rightarrow ZZ^* \rightarrow 4\ell$) $t\bar{t}H$ leptonic, $H \rightarrow ZZ^* \rightarrow 4\ell$ $t\bar{t}H$ hadronic, $H \rightarrow ZZ^* \rightarrow 4\ell$			$t\bar{t}H$ 1 ℓ, boosted $t\bar{t}H$ 1 ℓ, resolved (11 categories) $t\bar{t}H$ 2 ℓ (7 categories)
VH	VH 2 ℓ VH 1 ℓ, $p_{\mathrm{T}}^{\ell+E_{\mathrm{T}}^{\mathrm{miss}}} \geq 150$ GeV VH 1 ℓ, $p_{\mathrm{T}}^{\ell+E_{\mathrm{T}}^{\mathrm{miss}}} < 150$ GeV VH $E_{\mathrm{T}}^{\mathrm{miss}}$, $E_{\mathrm{T}}^{\mathrm{miss}} \geq 150$ GeV VH $E_{\mathrm{T}}^{\mathrm{miss}}$, $E_{\mathrm{T}}^{\mathrm{miss}} < 150$ GeV VH+VBF $p_{\mathrm{T}}^{j1} \geq 200$ GeV VH hadronic (2 categories)	VH leptonic 0-jet, $p_{\mathrm{T}}^{4\ell} \geq 100$ GeV 2-jet, $m_{jj} < 120$ GeV			2 ℓ, $75 \leq p_{\mathrm{T}}^{V} < 150$ GeV, $N_{\mathrm{jets}} = 2$ 2 ℓ, $75 \leq p_{\mathrm{T}}^{V} < 150$ GeV, $N_{\mathrm{jets}} \geq 3$ 2 ℓ, $p_{\mathrm{T}}^{V} \geq 150$ GeV, $N_{\mathrm{jets}} = 2$ 2 ℓ, $p_{\mathrm{T}}^{V} \geq 150$ GeV, $N_{\mathrm{jets}} \geq 3$ 1 ℓ $p_{\mathrm{T}}^{V} \geq 150$ GeV, $N_{\mathrm{jets}} = 2$ 1 ℓ $p_{\mathrm{T}}^{V} \geq 150$ GeV, $N_{\mathrm{jets}} = 3$ 0 ℓ, $p_{\mathrm{T}}^{V} \geq 150$ GeV, $N_{\mathrm{jets}} = 2$ 0 ℓ, $p_{\mathrm{T}}^{V} \geq 150$ GeV, $N_{\mathrm{jets}} = 3$
VBF	VBF, $p_{\mathrm{T}}^{\gamma\gamma jj} \geq 25$ GeV (2 categories) VBF, $p_{\mathrm{T}}^{\gamma\gamma jj} < 25$ GeV (2 categories)	2-jet VBF, $p_{\mathrm{T}}^{j1} \geq 200$ GeV 2-jet VBF, $p_{\mathrm{T}}^{j1} < 200$ GeV	2-jet VBF	VBF $p_{\mathrm{T}}^{\tau\tau} > 140$ GeV ($\tau_{\mathrm{had}}\tau_{\mathrm{had}}$ only) VBF high-m_{jj} VBF low-m_{jj}	VBF, two central jets VBF, four central jets VBF+γ
ggF	2-jet, $p_{\mathrm{T}}^{\gamma\gamma} \geq 200$ GeV 2-jet, 120 GeV$\leq p_{\mathrm{T}}^{\gamma\gamma} < 200$ GeV 2-jet, 60 GeV$\leq p_{\mathrm{T}}^{\gamma\gamma} < 120$ GeV 2-jet, $p_{\mathrm{T}}^{\gamma\gamma} < 60$ GeV 1-jet, $p_{\mathrm{T}}^{\gamma\gamma} \geq 200$ GeV 1-jet, 120 GeV$\leq p_{\mathrm{T}}^{\gamma\gamma} < 200$ GeV 1-jet, 60 GeV$\leq p_{\mathrm{T}}^{\gamma\gamma} < 120$ GeV 1-jet, $p_{\mathrm{T}}^{\gamma\gamma} < 60$ GeV 0-jet (2 categories)	1-jet, $p_{\mathrm{T}}^{4\ell} \geq 120$ GeV 1-jet, 60 GeV$\leq p_{\mathrm{T}}^{4\ell} < 120$ GeV 1-jet, $p_{\mathrm{T}}^{4\ell} < 60$ GeV 0-jet, $p_{\mathrm{T}}^{4\ell} < 100$ GeV	1-jet, $m_{\ell\ell} < 30$ GeV, $p_{\mathrm{T}}^{\ell_2} < 20$ GeV 1-jet, $m_{\ell\ell} < 30$ GeV, $p_{\mathrm{T}}^{\ell_2} \geq 20$ GeV 1-jet, $m_{\ell\ell} \geq 30$ GeV, $p_{\mathrm{T}}^{\ell_2} < 20$ GeV 1-jet, $m_{\ell\ell} \geq 30$ GeV, $p_{\mathrm{T}}^{\ell_2} \geq 20$ GeV 0-jet, $m_{\ell\ell} < 30$ GeV, $p_{\mathrm{T}}^{\ell_2} < 20$ GeV 0-jet, $m_{\ell\ell} < 30$ GeV, $p_{\mathrm{T}}^{\ell_2} \geq 20$ GeV 0-jet, $m_{\ell\ell} \geq 30$ GeV, $p_{\mathrm{T}}^{\ell_2} < 20$ GeV 0-jet, $m_{\ell\ell} \geq 30$ GeV, $p_{\mathrm{T}}^{\ell_2} \geq 20$ GeV	Boosted, $p_{\mathrm{T}}^{\tau\tau} > 140$ GeV Boosted, $p_{\mathrm{T}}^{\tau\tau} \leq 140$ GeV	

3.1 $H \to \gamma\gamma$

The $H \to \gamma\gamma$ analysis [4, 6] requires the presence of two isolated photons [83] within the pseudorapidity range $|\eta| < 2.37$, excluding the region $1.37 < |\eta| < 1.52$ corresponding to the transition between the barrel and endcap sections of the electromagnetic calorimeter. The transverse momenta of the leading and subleading photons are required to be greater than $0.35 m_{\gamma\gamma}$ and $0.25 m_{\gamma\gamma}$ respectively, where $m_{\gamma\gamma}$ is the invariant mass of the diphoton system. The distribution of $m_{\gamma\gamma}$ is used to separate the Higgs boson signal from continuum background processes. These mainly arise from prompt $\gamma\gamma$ production, single-photon production where an additional jet in the event is misidentified as a photon, and processes where two jets are misidentified as photons. The event reconstruction and selection procedures are largely unchanged with respect to the ones described in Ref. [4]. The only significant change concerns the reconstruction of the calorimeter clusters associated with the photons: a dynamical, topological cell clustering-based algorithm [84, 85] is now used instead of a sliding-window technique [83, 86].

Selected events are separated into 29 mutually exclusive categories based on the kinematics of the diphoton system and associated particles, chosen to approximately match those of the Stage 1 STXS regions described in Section 6.1. Seven categories are defined to select $t\bar{t}H$ production, targeting both leptonic and hadronic top decay processes through various selections on the multiplicities and kinematics of leptons [87, 88], jets [89], and jets tagged as containing b-hadrons [90]. These categories are described in detail in Ref. [6]. The remaining events are classified into categories targeting the VH, VBF and ggF production modes, described in detail in Ref. [4]. Five categories are defined to select WH and ZH production with leptonic decays of the W or Z, based on the presence of leptons and missing transverse momentum $E_{\mathrm{T}}^{\mathrm{miss}}$ [91]. Seven categories target the VBF and VH processes: one category requires the presence of two jets, with the leading jet transverse momentum $p_{\mathrm{T}j_1} > 200$ GeV; two categories select hadronic vector boson decays by requiring two jets with an invariant mass compatible with the W or Z boson mass; and four categories target VBF production by requiring forward jets in a VBF-like topology. The requirement of a second jet for the $p_{\mathrm{T}j_1} > 200$ GeV category is a change compared to [4] where only one jet was required, and helps to reduce contamination from ggF production. The remaining events are split into 10 categories, separating events with 0, 1, and $\geq$ 2-jets and classifying them further according to the pseudorapidity of the two photons (for 0-jet events) or the transverse momentum of the diphoton system $p_{\mathrm{T}}^{\gamma\gamma}$ (for 1 and $\geq$ 2-jet events).

3.2 $H \to ZZ^* \to 4\ell$

The $H \to ZZ^* \to 4\ell$ analysis requires the presence of at least two same-flavor and opposite-charge light-lepton pairs. The analysis follows the strategy described in the previous publication [5], but employs improved event reconstruction and electron reconstruction [92] techniques, and defines additional event categories to enhance sensitivity to the production of the SM Higgs boson associated with a vector boson (VH, $V \to \ell\nu/\nu\nu$) and with a top quark pair [6]. The largest background is the continuum $(Z^{(*)}/\gamma^*)(Z^{(*)}/\gamma^*)$ production, modeled using Monte Carlo simulation. Other background contributions arise from $Z+$jets and $t\bar{t}$ production with two prompt leptons and are estimated using data. The four-lepton invariant mass ($m_{4\ell}$) distribution is used to separate the Higgs boson signal from background processes. Boosted decision trees (BDTs) are employed to further separate the signal from the background processes and to enhance the sensitivity to the various Higgs boson production modes.

To distinguish the $t\bar{t}H$, VH, VBF, and ggF production modes and to enhance the purity of each kinematic selection, 11 mutually exclusive reconstructed event categories are defined based on the presence of jets and additional leptons in the final state. Candidate events with at least one b-tagged jet and three or more additional jets, or one additional lepton and at least two additional jets are classified into categories enriched in $t\bar{t}H$ production with respectively fully hadronic or leptonic top quark decays [6]. Events failing these requirements but containing at least one additional lepton are classified in a VH-enriched category with leptonic vector boson decays. The remaining events are classified according to their jet multiplicity (0-jet, 1-jet, and $\geq$ 2-jet). Events with at least two jets are divided into a VBF-enriched region, for which the dijet invariant mass m_{jj} is required to be above 120 GeV, and a region enriched in VH production mode with a hadronically decaying vector boson for $m_{jj} < 120$ GeV. The VBF-enriched region is further split into two categories, in which the transverse momentum of the leading jet $p_{\mathrm{T,jet}}$ is required to be either above or below 200 GeV. The selected 0-jet and 1-jet events are further separated according to the transverse momentum $p_{\mathrm{T}}^{4\ell}$ of the four-lepton system: the 0-jet events are split into 2 categories with a boundary at $p_{\mathrm{T}}^{4\ell} = 100$ GeV, with the higher $p_{\mathrm{T}}^{4\ell}$ selection being enriched in Higgs boson events produced in association with a weak vector boson. The 1-jet events are split into three categories with boundaries at $p_{\mathrm{T}}^{4\ell} = 60$ and 120 GeV to match the STXS selections described in Section 6.1.

3.3 $H \to WW^* \to e\nu\mu\nu$

The $H \to WW^* \to e\nu\mu\nu$ analysis [7] included in the combination targets the ggF and VBF production modes. Signal candidates are selected by requiring the presence of an isolated $e^{\pm}\mu^{\mp}$ pair, with transverse momentum thresholds at 22 and 15 GeV for the leading and subleading lepton. Events with jets tagged as containing b-quarks are rejected to suppress background contributions originating from top-quark production. Contributions from $W \to \tau\nu$ decays in which the tau leptons subsequently decay into electrons or muons are also included.

The primary background processes are WW, top-quark, W+jets, Drell–Yan, and other diboson (WZ, $W\gamma$, $W\gamma^*$, and ZZ) production. Most of these contributions are estimated using data in kinematic regions enriched in the given process.

Selected events are classified according to the number of associated jets (N_{jets}). Exclusive $N_{\mathrm{jets}} = 0$ and $N_{\mathrm{jets}} = 1$ selections are enriched in signal events produced via ggF. To isolate regions with higher sensitivity, they are each further split into eight categories apiece, based on the flavor of the leading lepton (e or μ), two bins of the invariant mass of the dilepton system $m_{\ell\ell}$ and two bins of the transverse momentum of the sub-leading lepton $p_{\mathrm{T}}^{\ell_2}$. The distribution of the transverse mass of the dilepton plus $E_{\mathrm{T}}^{\mathrm{miss}}$ system is used to separate the Higgs boson signal from background in each category. The $N_{\mathrm{jets}} \geq 2$ category is naturally sensitive to the VBF process. A central-jet veto is applied to suppress the QCD multijet background and the contribution from ggF production. The output of a boosted decision tree exploiting the kinematic properties of the two leading jets and the two leptons is used to separate the VBF Higgs boson production from background processes, including Higgs boson production via ggF.

3.4 $H \to \tau\tau$

The $H \to \tau\tau$ analysis [8] measures the Higgs boson production cross section in the VBF production process or in ggF production with large Higgs boson transverse momentum p_{T}^{H}. Final states with both leptonic (τ_{lep}) and hadronic (τ_{had}) decays of the tau lepton are considered. Selected lepton candidates are required to be of opposite charge, pass identification and isolation criteria and satisfy the p_{T} thresholds of the triggers used. Three mutually exclusive analysis channels, $\tau_{\mathrm{lep}}\tau_{\mathrm{lep}}$, $\tau_{\mathrm{lep}}\tau_{\mathrm{had}}$, and $\tau_{\mathrm{had}}\tau_{\mathrm{had}}$, are defined according to the number of selected electron, muon and hadronic tau candidates. All channels require the presence of at least one jet with high transverse momentum.

To exploit signal-sensitive event topologies, candidate events are divided into three categories targeting the VBF process and two categories targeting high-p_{T}^{H} Higgs production. The VBF categories collect events with two jets with a large pseudorapidity separation and a high invariant mass (m_{jj}). The Higgs boson decay products are required to be in the central rapidity region. One VBF category is defined by requiring the transverse momentum of the $\tau\tau$ system $p_{\mathrm{T}}^{\tau\tau}$ to be above 140 GeV, for $\tau_{\mathrm{had}}\tau_{\mathrm{had}}$ events only. The two remaining VBF categories are defined for lower and higher values of m_{jj}, with definitions that differ between the $\tau_{\mathrm{lep}}\tau_{\mathrm{lep}}$, $\tau_{\mathrm{lep}}\tau_{\mathrm{had}}$, and $\tau_{\mathrm{had}}\tau_{\mathrm{had}}$ channels. The high-p_{T}^{H} categories select events with large values of $p_{\mathrm{T}}^{\tau\tau}$, with contributions mainly from the ggF process. Events failing the VBF selection and with $p_{\mathrm{T}}^{\tau\tau} > 100$ GeV are selected. In order to improve the sensitivity of the analysis, two categories are defined respectively for $p_{\mathrm{T}}^{\tau\tau} > 140$ GeV and $p_{\mathrm{T}}^{\tau\tau} \leq 140$ GeV, with additional selections on the angular separation between the tau leptons. The distribution of the invariant mass of the di-tau system is used to separate the Higgs boson signal from background. In all three sub-channels, the most important backgrounds are irreducible $Z \rightarrow \tau\tau$ events, and events with one or two jets misidentified as tau lepton decay products, primarily from multijet and W+jets production.

3.5 $H \rightarrow b\bar{b}$

The $H \rightarrow b\bar{b}$ decay channel is used to measure the production cross section for the VH and VBF production modes.

The search for $H \rightarrow b\bar{b}$ in the VH production mode [9, 10] considers final states containing at least two jets, of which exactly two must be tagged as containing b-hadrons. Either zero, one or two charged leptons are also required, exploring the associated production of a Higgs boson with a W or Z boson decaying leptonically as $Z \rightarrow \nu\nu$, $W \rightarrow \ell\nu$, or $Z \rightarrow \ell\ell$. Contributions from $W \rightarrow \tau\nu$ and $Z \rightarrow \tau\tau$ decays in which the tau-leptons subsequently decay to electrons or muons are also included. The largest background contributions arise from V+heavy-flavor-jets and $t\bar{t}$ production, and their normalization is estimated using data. Other significant background sources are single-top-quark and diboson (WZ and ZZ) production. Their normalizations are obtained from theory predictions, while their shape is taken from simulation. Multijet events enter the selection due to jets mis-measured in the calorimeters and are estimated using data-driven control samples.

To enhance the signal sensitivity, selected candidate events are classified according to the charged lepton multiplicity, the vector boson transverse momentum p_{T}^{V}, and the jet multiplicity. For final states with zero or one lepton, $p_{\mathrm{T}}^{V} > 150$ GeV is required. In two-lepton final states two regions are considered, 75 GeV $< p_{\mathrm{T}}^{V} <$ 150 GeV and $p_{\mathrm{T}}^{V} > 150$ GeV. The p_{T}^{V} thresholds are chosen to select regions with strong experimental sensitivity, and match the STXS definitions described in Section 6.1. Each of these regions is finally separated into a category with exactly two reconstructed jets and another with three or more. In the zero- and one-lepton channel, events with four or more jets are rejected. Topological and kinematic selection criteria are applied within each of the resulting categories. Boosted decision trees incorporating the event kinematics and topology in addition to the dijet invariant mass are employed in each lepton channel and analysis region to separate the signal process from the sum of the expected background processes.

The $H \rightarrow b\bar{b}$ mode is also used to measure the VBF production process [11]. Three orthogonal selections are employed, targeting two all-hadronic channels and a photon-associated channel. Each selection requires the presence of at least two jets tagged as containing b-hadrons in the central pseudorapidity region $|\eta| < 2.5$ as well as at least two additional jets used to identify the VBF topology.

The first of the two all-hadronic selections requires the b-tagged jets to have transverse momenta larger than 95 GeV and 70 GeV, while one of the additional jets is required to be in the forward region $3.2 < |\eta| < 4.4$ and have a transverse momentum larger than 60 GeV and another must satisfy $p_{\mathrm{T}} > 20$ GeV and $|\eta| < 4.4$. The transverse momentum p_{T}^{bb} of the system composed of the two b-tagged jets must be larger than 160 GeV.

The second all-hadronic selection with four central jets is defined by the presence of two jets with $|\eta| < 2.8$ in addition to the b-tagged jets with $|\eta| < 2.5$. All selected jets are required to pass a common threshold of 55 GeV on their transverse momenta. The p_{T} of the bb-system required to be larger than 150 GeV. Events containing at least one forward jet satisfying the selection criteria of the first all-hadronic channel, are removed.

A VBF+γ selection is defined by the presence of a photon with transverse momentum $E_T > 30$ GeV and $|\eta| < 2.37$, excluding the region $1.37 < |\eta| < 1.52$, which suppresses the dominant background from non-resonant $b\bar{b}jj$ production. Events must have at least four jets, all satisfying $p_{\mathrm{T}} > 40$ GeV and $|\eta| < 4.4$, with at least two jets in $|\eta| < 2.5$ passing the b-tag requirements. The invariant mass of the VBF jets is required to be higher than 800 GeV, and $p_{\mathrm{T}}^{bb} > 80$ GeV. In all three selections a BDT built from variables describing jet and photon kinematics is used to enhance the sensitivity. The signal is extracted from a fit to the distribution of the invariant mass m_{bb} of the two b-tagged jets.

The main background contributions originate from non-resonant production of b-tagged jet pairs, with smaller contributions from $Z \to b\bar{b}$ production. Non-resonant background yields in the photon-associated channel are about two orders of magnitude lower than in the other two VBF selections. The VBF, $H \to b\bar{b}$ channels are included in all the measurements except for those presented in Section 6.

3.6 $H \to \mu\mu$

The $H \to \mu\mu$ search uses a similar technique as $H \to \gamma\gamma$, requiring a pair of opposite-charge muons and using the distribution of the invariant mass $m_{\mu\mu}$ to separate signal from background. Events are classified into eight categories. The output of a BDT exploiting the kinematic properties of the two leading jets and the two muons is used to define two categories targeting the VBF process. In order to enhance the sensitivity of the analysis, the remaining events are classified into three ranges of the transverse momentum $p_{\mathrm{T}}^{\mu\mu}$ of the dimuon system ($p_{\mathrm{T}}^{\mu\mu} < 15$ GeV, 15 GeV $\leq p_{\mathrm{T}}^{\mu\mu} < 50$ GeV and $p_{\mathrm{T}}^{\mu\mu} \geq 50$ GeV) and two ranges of the muon pseudorapidities η^{μ} (both muons within $|\eta^{\mu}| \leq 1$, or at least one muon outside this range), for a total of six categories. The analysis follows closely the $H \to \mu\mu$ search described in Ref. [14], which used a smaller dataset collected in 2015 and 2016 only. The analysis does not provide a sensitivity at the level of the Higgs boson signal expected in the SM, and is only included in the results presented in Section 7.4.

3.7 $t\bar{t}H, H \to b\bar{b}$ and $t\bar{t}H$ multilepton analyses

Searches for the associated production of the Higgs boson with a $t\bar{t}$ pair have been performed using Higgs boson decays to $b\bar{b}$ [13] and in multilepton final states, targeting Higgs boson decays to WW^*, ZZ^* and $\tau\tau$ [6, 12]. These analyses complement the selections sensitive to $t\bar{t}H$ production defined in the analyses of the $H \to \gamma\gamma$ and $H \to ZZ^* \to 4\ell$ decay channels, described in Sections 3.1 and 3.2.

The search for $t\bar{t}H$ production with $H \rightarrow b\bar{b}$ employs two selections, optimized for single-lepton and dilepton final states of $t\bar{t}$ decays. In the single lepton channel, events are required to have one isolated electron or muon and at least five jets, of which at least two must be identified as containing b-hadrons. In the dilepton channel, events are required to have two opposite-charge leptons and at least three jets, of which at least two must be identified as containing b-hadrons. Candidate events are classified into eleven (seven) orthogonal categories in the single lepton (dilepton) channel, according to the jet multiplicity and the values of the b-tagging discriminant for the jets. In the single-lepton channel, an additional category, referred to as *boosted*, is designed to select events with large transverse momenta for the Higgs candidate ($p_{\mathrm{T}}^{H} > 200$ GeV) and one of the top quark candidates ($p_{\mathrm{T}}^{t} > 250$ GeV). In each signal-enriched region, a BDT exploiting kinematic information of the events is employed to separate $t\bar{t}H$ production from background processes. Some of the selected regions are enriched in the main background processes, $t\bar{t}$ + light flavor, $t\bar{t}+ \geq 1b$, $t\bar{t}+ \geq 1c$, $t\bar{t} + V$ and non-$t\bar{t}$ production, and are used to estimate their yields.

The $t\bar{t}H$ search with Higgs boson decays to WW^*, ZZ^* and $\tau\tau$ exploits several multilepton signatures resulting from leptonic decays of vector bosons and/or the presence of hadronically-decaying τ lepton candidates. Seven final states, categorized by the number and flavor of reconstructed charged lepton candidates, are examined. They are: one lepton with two hadronic τ candidates, two same-charge leptons with zero or one hadronic τ candidates, two opposite-charge leptons with one hadronic τ candidate, three leptons with zero or one hadronic τ candidates, and four leptons, excluding events from $H\rightarrow ZZ^*\rightarrow 4\ell$ decays. Events in all channels are required to have at least two jets, at least one of which must be b-tagged. Additional requirements are employed for each final state. The largest backgrounds arise from leptons produced in heavy-flavor decays, photon conversions or misidentified hadronic jets, from electron charge misreconstruction in events where opposite-sign leptons are produced and from the production of $t\bar{t} + W/Z$. Multivariate analysis techniques exploiting the kinematic properties and topologies of the selected events have been applied in most channels to improve the discrimination between the signal and the background. The number of expected background events and the associated kinematic distributions are estimated using data-driven methods and simulation.

3.8 Searches for invisible Higgs boson decays

Searches targeting decays of the Higgs boson to invisible final states select events with large missing transverse momentum; backgrounds are suppressed by requiring in addition either jets with a VBF topology [15], an associated Z boson decaying to charged leptons [16] or an associated W or Z boson decaying to hadronic final states [17].

Production in the VBF topology is identified by requiring two jets with a pseudorapidity difference $|\Delta\eta_{jj}| > 4.8$ and invariant mass $m_{jj} > 1\,\mathrm{TeV}$. The missing transverse momentum is required to be larger than 180 GeV. Events with isolated lepton candidates or additional jets are rejected. Three signal regions are defined for $1 < m_{jj} < 1.5\,\mathrm{TeV}$, $1.5 < m_{jj} < 2\,\mathrm{TeV}$ and $m_{jj} > 2\,\mathrm{TeV}$. The leading background processes, $(Z\rightarrow \ell\ell)$+jets production and $(W\rightarrow \ell\nu)$+jets production with an undetected charged lepton, are estimated in data using control regions and extrapolated to the signal region using MC simulations.

Production in association with a leptonically decaying Z boson is identified by requiring the presence of a pair of isolated electrons or muons with an invariant mass close to m_Z. The magnitude of the missing transverse momentum is required to be larger than 90 GeV. It must also be larger than 60% of the scalar sum of the transverse momenta of the identified leptons and jets, and must be oriented back-to-back with the dilepton system in the transverse plane. The leading background processes, $(Z\rightarrow \ell\ell)(Z\rightarrow \nu\nu)$

production and $(Z\to\ell\ell)(W\to\ell\nu)$ production with an additional undetected charged lepton, are estimated from simulation.

Two event topologies are considered to identify production in association with a hadronically decaying W and Z boson. The *resolved* topology is defined by the presence of two jets compatible with originating from the hadronic decay of a W or Z, reconstructed using the anti-k_t algorithm [93] with a radius parameter of 0.4. The *merged* topology, targeted towards W or Z bosons with large transverse momentum, is identified through the presence of a single jet, reconstructed using the anti-k_t algorithm with a radius parameter of 1. The missing transverse momentum is required to be larger than 150 GeV and 250 GeV for the resolved and boosted topology respectively. In both cases, events are categorized according to the multiplicity of jets tagged as containing b-quarks. A separate category is also defined for events in which the mass of the jet system, defined as the dijet mass in the resolved topology and the mass of the large-radius jet in the merged topology, is compatible with a hadronic W or Z decay. The main backgrounds, from W+jets, Z+jets and $t\bar{t}$ production, are estimated from control regions in data.

These analyses are only included in the coupling measurements presented in Sections 7.3 and 7.5.

3.9 Off-shell Higgs boson production

Measurements of the $H^* \to ZZ$ final state in the mass range above the $2m_Z$ threshold (off-shell region) provide the opportunity to measure the off-shell coupling strength of the observed Higgs boson, as discussed in Refs. [94–97]. The $ZZ \to 4\ell$ and $ZZ \to 2\ell 2\nu$ decay channels, detailed in Ref. [18], are used in these measurements.

Assuming that the on-shell and off-shell coupling modifiers are the same and the ratio of the Higgs boson couplings to the SM predictions is independent of the momentum transfer of the Higgs production mechanism considered in the analysis, the total width of the Higgs boson can be constrained from a combination with the on-shell measurements. It is also assumed that any new physics which modifies the off-shell signal strength and the off-shell couplings does not modify the relative phase of the interfering signal and background processes. Further, it is assumed that there are neither sizeable kinematic modifications to the off-shell signal nor new sizeable signals in the search region of this analysis unrelated to an enhanced off-shell signal strength [98, 99].

The analysis in the $ZZ \to 4\ell$ final state follows closely the Higgs boson measurements in the same final state, described in Section 3.2, with the same event reconstruction, trigger and event selections and background estimation methods. The off-peak region is defined to include the range $220\,\text{GeV} < m_{4\ell} < 2000\,\text{GeV}$. Like the $H \to ZZ^* \to 4\ell$ analysis, the background is dominated by $q\bar{q}/gg \to ZZ$ production. A matrix-element-based discriminant is constructed to enhance the $gg \to H^* \to ZZ$ signal and is used in a binned maximum-likelihood fit for the final result.

The analysis in the $ZZ \to 2\ell 2\nu$ channel is similar to the one performed to search for heavy ZZ resonances [100] with the same object definitions. The analysis is performed inclusively in the number of final state jets and thus kinematic selections are optimized accordingly. SM ZZ and WZ production are the major backgrounds. The transverse mass (m_{T}^{ZZ}) [18], reconstructed from the momentum of the dilepton system and the missing transverse momentum, is chosen as the discriminating variable. Events in the range of $250\,\text{GeV} < m_{\mathrm{T}}^{ZZ} < 2000\,\text{GeV}$ are used in a binned maximum likelihood fit for the final result.

These off-shell analyses are only included in the coupling measurements presented in Section 7.5.

4 Statistical model

The statistical methods used in this note follow those of Ref. [3]. The results of the combination are obtained from a likelihood function defined as the product of the likelihoods of each input analysis. These are themselves products of likelihoods computed in mutually exclusive regions selected in the analysis, referred to as analysis categories.

The number of signal events in each analysis category k is expressed as

$$n_k^{\text{signal}} = \mathcal{L}_k \sum_i \sum_f (\sigma \times \mathrm{B})_{if} (A \times \epsilon)_{if,k} \tag{1}$$

where the sum runs over production modes i (i = ggF, VBF, $WH, ZH, t\bar{t}H, \ldots$) and decay final states f ($f = \gamma\gamma, ZZ^*, WW^*, \tau\tau, b\bar{b}, \mu\mu$), $\mathcal{L}_k$ is the integrated luminosity of the dataset used in category k, and $(A \times \epsilon)_{if,k}$ is the acceptance times efficiency factor in category k for production mode i and final state f. The cross section times branching ratio $(\sigma \times \mathrm{B})_{if}$ for each relevant pair (i, f) are the parameters of interest of the model. The measurements presented in this note are obtained from fits in which these expressions are free parameters (Section 5.3), or in which they are re-expressed in terms of smaller sets of parameters: of a single signal strength parameter μ (Section 5.1), of the cross sections σ_i in each of the main production modes (Section 5.2), of ratios of cross sections and branching ratios (Sections 5.4 and Section 6.2) or of coupling modifiers (Section 7). Additional parameters, denoted as nuisance parameters, are used to describe systematic uncertainties and background quantities that are constrained by sidebands or control regions in data.

Systematic uncertainties that affect multiple analyses are modeled with common nuisance parameters to propagate the effect of these uncertainties coherently to all measurements. The assessment of the associated uncertainties varies between data samples, reconstruction algorithms and software releases, leading to differences in particular between analyses performed using the 2017 data set and those using 2015 and 2016 data only. Some components of the systematic uncertainties in the luminosity, the jet energy scale, the electron/photon resolution and energy scale, and in the electron reconstruction and identification efficiencies are correlated between the analyses. Uncertainties due to the limited number of simulated events used to estimate expected signal and background yields are included using the simplified version of the Beeston–Barlow technique [101] implemented in the HistFactory tool [102]. They are counted among the systematic uncertainties.

Theory uncertainties affecting the inclusive signal yields of each production and decay process, such as missing higher-order QCD corrections and PDF-induced uncertainties are described by a common set of nuisance parameters in most channels. Components of theory uncertainties that affect the acceptances in the various categories are also modeled using common nuisance parameters, except in cases where their effect in different regions is expected to originate from uncorrelated sources. In the latter case, the uncertainty is modeled using separate sets of nuisance parameters in each region. The effects of correlations between Higgs boson branching fractions are modeled using the correlation model specified in Ref. [26]. Uncertainties due to dependencies on SM parameter values and missing-high-order effects are applied to the partial decay widths and propagated to the branching ratios. The uncertainties due to modeling of background processes are typically treated as uncorrelated between analyses.

The measurement of the parameters of interest is carried out using a statistical test based on the profile likelihood ratio [103],

$$\Lambda(\boldsymbol{\alpha}) = \frac{L(\boldsymbol{\alpha}, \hat{\hat{\boldsymbol{\theta}}}(\boldsymbol{\alpha}))}{L(\hat{\boldsymbol{\alpha}}, \hat{\boldsymbol{\theta}})}, \tag{2}$$

where $\boldsymbol{\alpha}$ and $\boldsymbol{\theta}$ are respectively the parameters of interest and the nuisance parameters. In the numerator, the nuisance parameters are set to their profiled values $\hat{\hat{\boldsymbol{\theta}}}(\boldsymbol{\alpha})$, which maximize the likelihood function for fixed values of the parameters of interest $\boldsymbol{\alpha}$. In the denominator, both the parameters of interest and the nuisance parameters are set to the values $\hat{\boldsymbol{\alpha}}$ and $\hat{\boldsymbol{\theta}}$ respectively which jointly maximize the likelihood.

In the asymptotic regime, in which the likelihood is approximately Gaussian, the value of $-2\ln\Lambda(\boldsymbol{\alpha})$ follows a χ^2 distribution with a number of degrees of freedom n equal to the dimensionality of the vector $\boldsymbol{\alpha}$ [103]. This property is assumed to hold for all the results presented in the following sections. Confidence intervals for a confidence level (CL) $1-p$ are then defined as the regions with values of $-2\ln\Lambda(\boldsymbol{\alpha})$ below a threshold $F^{-1}_{\chi^2_n}(1-p)$, where $F^{-1}_{\chi^2_n}$ is the quantile of the χ^2 distribution with n degrees of freedom.

The CL$_s$ prescription [104] is applied when setting upper limits on parameters directly related to measured event rates such as production cross sections.

For relevant parameters of interest a physical boundary on the parameter values is included in the statistical interpretation. For example, branching ratio parameters cannot conceptually be smaller than zero. The 95% confidence interval quoted for such parameters is then based on the profile likelihood ratio restricted to the allowed region of parameter space, using the $\tilde{t}_\mu$ test statistic of Ref. [103]. The confidence interval is defined by the standard χ^2 cutoff, which leads to some over-coverage near the boundaries.

Uncertainties on the measurement parameters are in some cases broken down into separate components for theory uncertainties affecting the background processes, theory uncertainties affecting the Higgs boson signal production, experimental uncertainties and statistical uncertainties. Each component is derived by fixing the associated nuisance parameters to their best-fit values $\hat{\theta}$ in both the numerator and denominator of Λ, and computing again the uncertainty on the measurement parameters. This is done for each component in turn, following the order in which they are listed above. The uncertainty obtained at at each step is then subtracted in quadrature from the uncertainty obtained in the previous step (in the first step, from the total uncertainty) to obtain the corresponding uncertainty component. The statistical uncertainty component is obtained in the last step, with all nuisance parameters fixed except for the ones that are only constrained by data, such as parameters used to describe data-driven background estimations.

For the systematic uncertainties reported in the detailed breakdowns of Tables 3 and 5, a simpler procedure is used: in each case the corresponding nuisance parameters are fixed to their best fit values, while other nuisance parameters are left free, and the resulting uncertainty is subtracted in quadrature from the total uncertainty.

The compatibility with the Standard Model is quantified using the test statistic $\lambda_{\mathrm{SM}} = -2\ln\Lambda(\boldsymbol{\alpha} = \boldsymbol{\alpha}_{\mathrm{SM}})$, where $\boldsymbol{\alpha}_{\mathrm{SM}}$ are the Standard Model values of the parameters of interest. A p-value[3] p_{SM} for the compatibility is computed in the asymptotic approximation as $p_{\mathrm{SM}} = 1 - F_{\chi^2_n}(\lambda_{\mathrm{SM}})$, with n equal to the number of free parameters of interest. For the cross section and branching ratio measurements reported in this note, this definition does not account for the uncertainties on the SM values used as reference and may therefore lead to an underestimation of the compatibility with the SM.

Results on expected significances and limits are obtained using the Asimov dataset technique [103].

---

[3] The p-value is defined as the probability to obtain a value of the test statistic that is at least as high as the observed value under the hypothesis that is being tested.

The correlation coefficients presented in this note are constructed as symmetric around the observed best fit values of the parameters of interest using the second derivatives of the negative log-likelihood ratio. Hence, the shown correlation matrices are not fully representative of the asymmetric uncertainties observed in the measurements. While the reported information is sufficient to reinterpret the measurements in terms of other parameterizations of the parameters of interest, this provides only an approximation to the information contained in the full likelihood function. For this reason, results for a number of commonly-used parameterizations are also provided in Sections 5 to 7.

5 Combined measurements of signal strength, production cross sections and branching ratios

5.1 Global signal strength

The global signal strength μ is determined following the procedures used for the measurements performed at $\sqrt{s}$ = 7 and 8 TeV [3]. For a specific production mode i and decay final state f, the signal yield is expressed in terms of a single modifier μ_{if}, as the production cross section σ_i and the branching fraction B_f cannot be separately measured without further assumptions. The modifiers are defined as the ratios of the measured Higgs boson yields and their SM expectations, denoted by the superscript *SM*,

$$\mu_{if} = \frac{\sigma_i}{\sigma_i^{\mathrm{SM}}} \times \frac{\mathrm{B}_f}{\mathrm{B}_f^{\mathrm{SM}}}. \tag{3}$$

The SM expectation by definition corresponds to $\mu_{if} = 1$. The uncertainties on the SM predictions are included as nuisance parameters in the measurement of the signal strength modifiers, following the methodology introduced in Section 4.

In the model used in this section, all the μ_{if} are set to a global signal strength μ, describing a common scaling of the expected Higgs boson yield in all categories. Its combined measurement is

$$\mu = 1.11^{+0.09}_{-0.08} = 1.11 \pm 0.05\,(\mathrm{stat.})\,^{+0.05}_{-0.04}\,(\mathrm{exp.})\,^{+0.05}_{-0.04}\,(\mathrm{sig.\ th.})\,\pm 0.03\,(\mathrm{bkg.\ th.})$$

where the total uncertainty is decomposed into components for statistical uncertainties, experimental systematic uncertainties, and theory uncertainties on signal and background modeling, following the procedure outlined in Section 4. The signal theory component includes uncertainties due to missing higher-order perturbative QCD and electroweak corrections in the MC simulation, uncertainties on PDF and α_s values, the treatment of the underlying event, the matching between the hard-scattering process and the parton shower, choice of hadronization models, and branching ratio uncertainties. The measurement is consistent with the SM prediction with a p-value of $p_{\mathrm{SM}} = 18\%$, computed using the procedure outlined in Section 4 with one degree of freedom. The value of $-2\ln\Lambda(\mu)$ as a function of μ is shown in Figure 1, for the full likelihood and the versions with sets of nuisance parameters fixed to their best-fit values to obtain the components of the uncertainty as described in Section 4.

Table 3 shows a summary of the leading uncertainties in the combined measurement of the global signal strength, with uncertainties computed as described in Section 4. The dominant uncertainties arise from the theory modeling of the signal and background processes in simulation. Further important uncertainties relate to the luminosity measurement; the selection efficiencies, energy scale and energy resolution of electrons and photons; the estimation of lepton yields from heavy-flavor decays, photon conversions or misidentified hadronic jets (classified as *background modelling* in the table); the jet energy scale and resolution, and the identification of heavy-flavor jets.

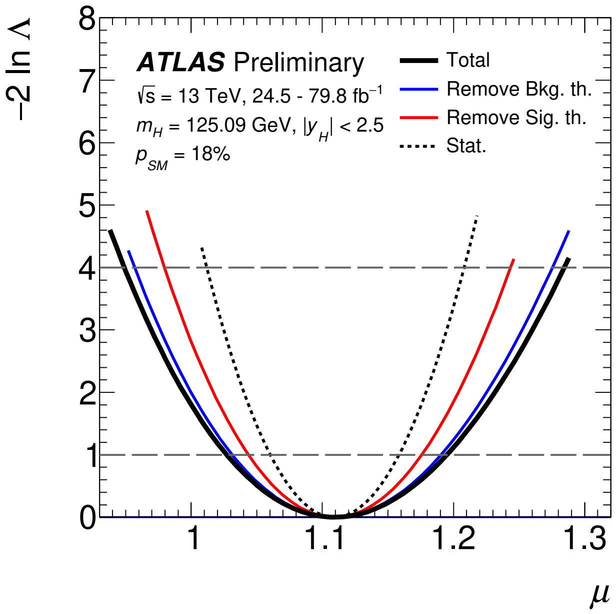

Figure 1: Variations of $-2\ln\Lambda(\mu)$ as a function of μ with all systematic uncertainties included (solid black line), with parameters describing theory uncertainties on background processes fixed to their best-fit values (solid blue line), with the same procedure also applied to theory uncertainties on the signal process (solid red line) and all systematic uncertainties (dotted black line). The dashed horizontal lines show the levels $-2\ln\Lambda(\mu) = 1$ and $-2\ln\Lambda(\mu) = 4$ which are used to define, respectively, the 1σ and 2σ confidence intervals on μ, as described in Section 4.

5.2 Production cross sections

Higgs boson production is studied in each of its main production modes. The production mechanisms considered are ggF, VBF, WH, ZH (including $gg \to ZH$), and the combination of $t\bar{t}H$ and tH ($t\bar{t}H$+tH). In cases where several processes are combined, the combination assumes the relative fractions of each component to be as in the SM, with theory uncertainties assigned. The small contribution from $b\bar{b}H$ is grouped with ggF. Cross sections are reported in the region $|y_H| < 2.5$ of the Higgs boson rapidity y_H. Results are obtained in a simultaneous fit to the data, with the cross section of each production mechanism as parameters of interest. Higgs boson decay branching fractions are set to their SM values, within the uncertainties specified in Ref. [26].

The results are shown in Figure 2 and Table 4. The leading sources of uncertainty on the production cross section measurements are summarized in Table 5, with uncertainties computed as described in Section 4. The measured $t\bar{t}H$+tH production cross section differs from the $t\bar{t}H$ cross section reported in Ref. [6], after accounting for the difference between the $|y_H| < 2.5$ region used in this note and the inclusive phase space considered in Ref. [6]. This is due in part to the inclusion of tH, which in Ref. [6] is fixed to the SM and not included in the reported $t\bar{t}H$ cross section, as well as to a better control of systematic effects, in particular related to photon energy scale and resolution, due to the $H \to \gamma\gamma$ categories targeting other processes which

Table 3: Summary of the relative uncertainties $\Delta\mu/\mu$ affecting the measurement of the combined global signal strength μ. "MC stat." refers to uncertainties due to limited numbers of simulated events. "Other" refers to the combined effect of the sources of experimental systematic uncertainty not explicitly listed in the table.

Uncertainty source	$\Delta\mu/\mu$ [%]
Statistical uncertainty	4.4
Systematic uncertainties	6.2
Theory uncertainties	4.8
Signal	4.2
Background	2.6
Experimental uncertainties (excl. MC stat.)	4.1
Luminosity	2.0
Background modeling	1.6
Jets, $E_{\mathrm{T}}^{\mathrm{miss}}$	1.4
Flavour tagging	1.1
Electrons, photons	2.2
Muons	0.2
τ-lepton	0.4
Other	1.6
MC statistical uncertainty	1.7
Total uncertainty	7.6

Table 4: Best-fit values and uncertainties of the production cross sections of the Higgs boson, assuming SM values for its decay branching fractions. The total uncertainties are decomposed into components for data statistics (Stat.), experimental systematic uncertainties (Exp.), and theory uncertainties in the modeling of the signal (Sig. th.) and background (Bkg. th.) processes. SM predictions [26] are shown for the cross section of each production process. The observed (obs.) and expected (exp.) significances of the observed signals relative to the no-signal hypothesis are also shown for all processes except ggF, which was observed in Run 1. For the WH and ZH modes, a combined VH significance is reported assuming the SM value of the ratio of WH to ZH production.

Process	Value	Uncertainty [pb]					SM pred.	Significance	
($\lvert y_H \rvert < 2.5$)	[pb]	Total	Stat.	Exp.	Sig. th.	Bkg. th.	[pb]	obs. (exp.)	
ggF	46.5	±4.0	±3.1	±2.2	±0.9	±1.3	44.7 ± 2.2	-	
VBF	4.25	$^{+0.84}_{-0.77}$	$^{+0.63}_{-0.60}$	$^{+0.35}_{-0.32}$	$^{+0.42}_{-0.32}$	$^{+0.14}_{-0.11}$	3.515 ± 0.075	6.5 (5.3)	
WH	1.57	$^{+0.48}_{-0.46}$	$^{+0.34}_{-0.33}$	$^{+0.25}_{-0.24}$	$^{+0.11}_{-0.07}$	±0.20	1.204 ± 0.024	3.5 (2.7)	5.3 (4.7)
ZH	0.84	$^{+0.25}_{-0.23}$	±0.19	±0.09	$^{+0.07}_{-0.04}$	±0.10	$0.797^{+0.033}_{-0.026}$	3.6 (3.6)	
$t\bar{t}H$+tH	0.71	$^{+0.15}_{-0.14}$	±0.10	±0.07	$^{+0.05}_{-0.04}$	$^{+0.08}_{-0.07}$	$0.586^{+0.034}_{-0.049}$	5.8 (5.4)	

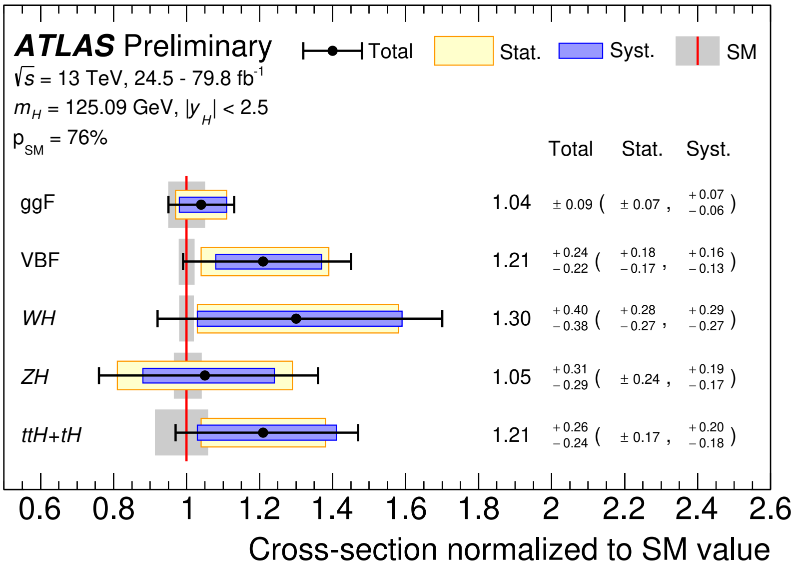

Figure 2: Cross sections for ggF, VBF, WH, ZH and $t\bar{t}H{+}tH$ normalized to their SM predictions, measured with the assumption of SM branching fractions. The black error bars, blue boxes and yellow boxes show the total, systematic, and statistical uncertainties in the measurements, respectively. The gray bands indicate the theory uncertainties in the cross section predictions.

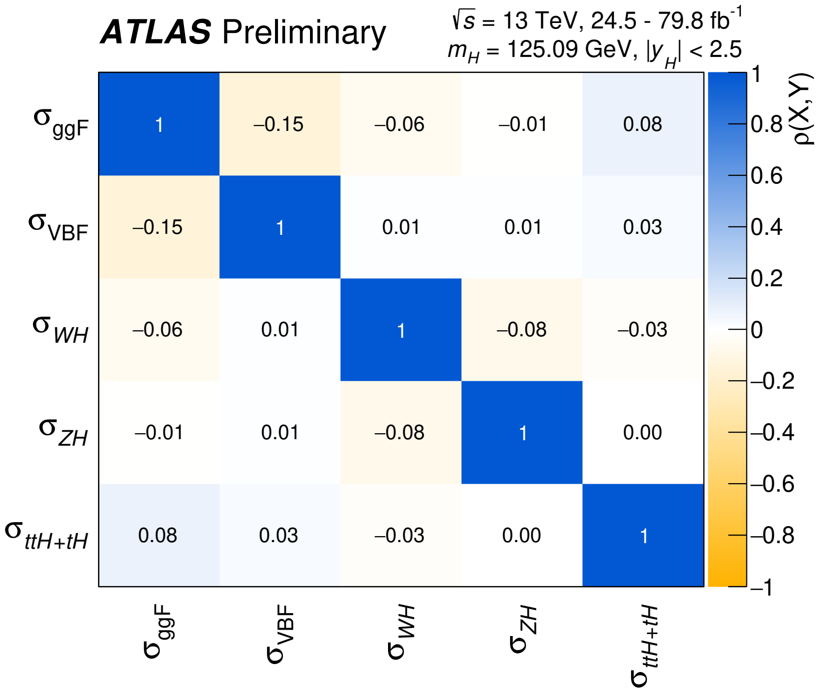

	σ_ggF	σ_VBF	σ_WH	σ_ZH	σ_ttH+tH
σ_ggF	1	−0.15	−0.06	−0.01	0.08
σ_VBF	−0.15	1	0.01	0.01	0.03
σ_WH	−0.06	0.01	1	−0.08	−0.03
σ_ZH	−0.01	0.01	−0.08	1	0.00
σ_ttH+tH	0.08	0.03	−0.03	0.00	1

Figure 3: Correlation matrix for the measurement of production cross sections of the Higgs boson, assuming SM values for its decay branching fractions.

Table 5: Summary of the uncertainties affecting the production cross section measurements. "MC stat." refers to uncertainties due to limited numbers of simulated events. "Other" refers to the combined effect of the sources of experimental systematic uncertainty not explicitly listed in the table.

Uncertainty source	$\frac{\Delta\sigma_{\text{ggF}}}{\sigma_{\text{ggF}}}$ [%]	$\frac{\Delta\sigma_{\text{VBF}}}{\sigma_{\text{VBF}}}$ [%]	$\frac{\Delta\sigma_{WH}}{\sigma_{WH}}$ [%]	$\frac{\Delta\sigma_{ZH}}{\sigma_{ZH}}$ [%]	$\frac{\Delta\sigma_{t\bar{t}H+tH}}{\sigma_{t\bar{t}H+tH}}$ [%]
Statistical uncertainties	6.4	15	21	23	14
Systematic uncertainties	6.2	12	22	17	15
Theory uncertainties	3.4	9.2	14	14	12
Signal	2.0	8.7	5.8	6.7	6.3
Background	2.7	3.0	13	12	10
Experimental uncertainties (excl. MC stat.)	5.0	6.5	9.9	9.6	9.2
Luminosity	2.1	1.8	1.8	1.8	3.1
Background modeling	2.5	2.2	4.7	2.9	5.7
Jets, $E_{\text{T}}^{\text{miss}}$	0.9	5.4	3.0	3.3	4.0
Flavour tagging	0.9	1.3	7.9	8.0	1.8
Electrons, photons	2.5	1.7	1.8	1.5	3.8
Muons	0.4	0.3	0.1	0.2	0.5
τ-lepton	0.2	1.3	0.3	0.1	2.4
Other	2.5	1.2	0.3	1.1	0.8
MC statistical uncertainties	1.6	4.8	8.8	7.9	4.4
Total uncertainties	8.9	19	30	29	21

are included in this combination, as described in Section 3.1. The correlations between the measured cross sections, shown in Figure 3, are significantly reduced with respect to previous analyses [3, 105].

A modest correlation of -15% between the ggF and VBF processes remains however, because of contributions from ggF production in the VBF-enriched selections. The compatibility between the measurement and the SM prediction corresponds to a p-value of $p_{\text{SM}} = 76\%$, computed using the procedure outlined in Section 4 with 5 degrees of freedom.

Figure 4 shows the observed likelihood contours in the plane of σ_{ggF} versus σ_{VBF} from individual channels and the combined fit, together with the SM prediction. The cross sections for the other production modes are profiled.

Significances above 5σ are observed for the combined measurements of the ggF, VBF, VH and $t\bar{t}H$+tH production processes. For the VBF process, the observed (expected) significance is 6.5σ (5.3σ). For the WH and ZH modes, these are respectively 3.5σ (2.7σ) and 3.6σ (3.6σ). Combining WH and ZH production into a single VH process, with the ratio of WH to ZH production set to its SM value leads to an observed (expected) significance for this process of 5.3σ (4.7σ). For the combination of $t\bar{t}H$ and tH production, the observed (expected) significance is 5.8σ (5.4σ).

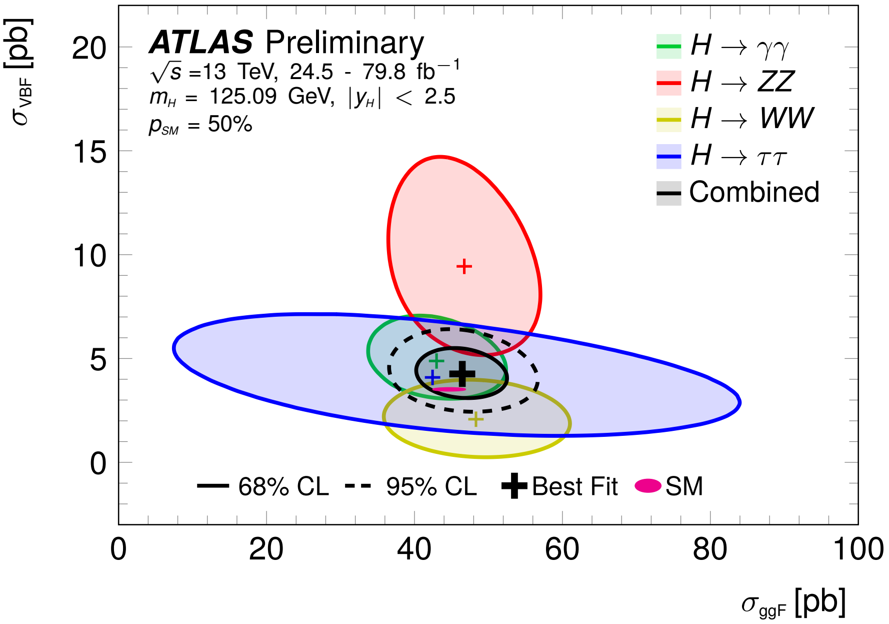

Figure 4: Observed likelihood contours in the plane of σ_{VBF} versus σ_{ggF} from individual channels and the combined fit. Contours for 68% (95%) CL, defined in the asymptotic approximation by $-2 \ln \Lambda = 2.28$ (5.99), are shown in solid (dashed) lines. The crosses indicate the best-fit values, and the solid ellipse the SM prediction. Higgs boson branching fractions are fixed to their SM values within theory uncertainties. The compatibility between the combined measurement and the SM prediction, estimated using the procedure outlined in the text with 2 degrees of freedom, is indicated.

5.3 Products of production cross sections and branching ratios

A description of both the production and decay mechanisms of the Higgs boson is obtained by considering the products $(\sigma \times \mathrm{B})_{if}$ of the cross section in production process i and branching fraction to final state f. The production processes are defined as in Section 5.2 except for the fact that the WH and ZH processes, which cannot be reliably determined in all decay channels except $H \to b\bar{b}$, are considered together as a single VH process, with the ratio of WH to ZH cross sections fixed to its SM value within uncertainties. The decay modes considered are $H \to \gamma\gamma$, $H \to ZZ^*$, $H \to WW^*$, $H \to \tau\tau$ and $H \to b\bar{b}$. There are in total 20 such independent products, but the analyses included in the combination provide little sensitivity to ggF production in the $H \to b\bar{b}$ decay mode, and to VH production in the $H \to WW^*$ and $H \to \tau\tau$ decay modes. The corresponding products are therefore fixed to their SM values within uncertainties. For the same reason, in $t\bar{t}H$ production the $H \to ZZ^*$ decay mode is considered together with $H \to WW^*$ as a single $H \to VV^*$ process, with the ratio of $H \to ZZ^*$ to $H \to WW^*$ fixed to its SM value. The results are obtained from a simultaneous fit of all input analyses, with the 15 independent $(\sigma \times \mathrm{B})$ products defined above as parameters of interest. They are shown in Figure 5 and Table 6. The correlation matrix of the measurements in shown in Figure 6. The largest terms in absolute value are between the $t\bar{t}H$, $H \to VV^*$ and $t\bar{t}H$, $H \to \tau\tau$ processes, and between the ggF, $H \to \tau\tau$ and VBF, $H \to \tau\tau$ processes. In both cases, this is due to cross-contamination between these processes in the analyses providing the most sensitive measurements. The compatibility between the measurement and the SM prediction corresponds to a p-value of $p_{\mathrm{SM}} = 71\%$, computed using the procedure outlined in Section 4 with 15 degrees of freedom.

Table 6: Best-fit values and uncertainties of the production cross sections times branching ratios of the Higgs boson, for the combinations in which sufficient sensitivity is provided by the input analyses. Combinations not shown in the table are fixed to their SM values within uncertainties. For $t\bar{t}H$+tH production, $H \rightarrow VV^*$ refers to the combination of $H \rightarrow WW^*$ and $H \rightarrow ZZ^*$, with a relative weight fixed by their respective SM branching fractions. The total uncertainties are decomposed into components for data statistics (Stat.), experimental systematic uncertainties (Exp.), and theory uncertainties in the modeling of the signal (Sig. th.) and background (Bkg. th.) processes. SM predictions [26] are shown for each process.

Process	Value	Uncertainty [fb]					SM pred.
($\lvert y_H \rvert < 2.5$)	[fb]	Total	Stat.	Exp.	Sig. th.	Bkg. th.	[fb]
ggF, $H \rightarrow \gamma\gamma$	97	± 14	± 11	± 8	± 2	$^{+2}_{-1}$	101.5 ± 5.3
ggF, $H \rightarrow ZZ^*$	1230	$^{+190}_{-180}$	± 170	± 60	± 20	± 20	1181 ± 61
ggF, $H \rightarrow WW^*$	10400	± 1800	± 1100	± 1100	± 380	$^{+960}_{-870}$	9600 ± 500
ggF, $H \rightarrow \tau\tau$	2700	$^{+1700}_{-1500}$	± 1000	± 920	$^{+810}_{-310}$	$^{+390}_{-420}$	2800 ± 140
VBF, $H \rightarrow \gamma\gamma$	11.1	$^{+3.2}_{-2.8}$	$^{+2.5}_{-2.4}$	$^{+1.4}_{-1.0}$	$^{+1.5}_{-1.1}$	$^{+0.3}_{-0.2}$	7.98 ± 0.21
VBF, $H \rightarrow ZZ^*$	249	$^{+91}_{-77}$	$^{+87}_{-75}$	$^{+16}_{-11}$	$^{+17}_{-12}$	$^{+9}_{-7}$	92.8 ± 2.3
VBF, $H \rightarrow WW^*$	450	$^{+270}_{-260}$	$^{+220}_{-200}$	$^{+120}_{-130}$	$^{+80}_{-70}$	$^{+70}_{-80}$	756 ± 19
VBF, $H \rightarrow \tau\tau$	260	$^{+130}_{-120}$	± 90	$^{+80}_{-70}$	$^{+30}_{-10}$	$^{+30}_{-20}$	220 ± 6
VBF, $H \rightarrow b\bar{b}$	6100	$^{+3400}_{-3300}$	$^{+3300}_{-3200}$	$^{+700}_{-600}$	± 300	± 300	2040 ± 50
VH, $H \rightarrow \gamma\gamma$	5.0	$^{+2.6}_{-2.5}$	$^{+2.4}_{-2.2}$	$^{+1.0}_{-0.9}$	± 0.5	± 0.1	$4.54^{+0.13}_{-0.12}$
VH, $H \rightarrow ZZ^*$	36	$^{+63}_{-41}$	$^{+62}_{-41}$	$^{+5}_{-4}$	$^{+6}_{-4}$	$^{+4}_{-2}$	52.8 ± 1.4
VH, $H \rightarrow b\bar{b}$	1380	$^{+310}_{-290}$	$^{+210}_{-200}$	± 150	$^{+120}_{-80}$	± 140	1162^{+31}_{-29}
$t\bar{t}H$+tH, $H \rightarrow \gamma\gamma$	1.46	$^{+0.55}_{-0.47}$	$^{+0.48}_{-0.44}$	$^{+0.19}_{-0.15}$	$^{+0.17}_{-0.11}$	± 0.03	$1.33^{+0.08}_{-0.11}$
$t\bar{t}H$+tH, $H \rightarrow VV^*$	212	$^{+84}_{-81}$	$^{+61}_{-59}$	$^{+47}_{-44}$	$^{+17}_{-10}$	$^{+31}_{-30}$	142^{+8}_{-12}
$t\bar{t}H$+tH, $H \rightarrow \tau\tau$	51	$^{+41}_{-35}$	$^{+31}_{-28}$	$^{+26}_{-21}$	$^{+6}_{-4}$	$^{+8}_{-6}$	$36.7^{+2.2}_{-3.1}$
$t\bar{t}H$+tH, $H \rightarrow b\bar{b}$	270	± 200	± 100	± 80	$^{+40}_{-10}$	$^{+150}_{-160}$	341^{+20}_{-29}

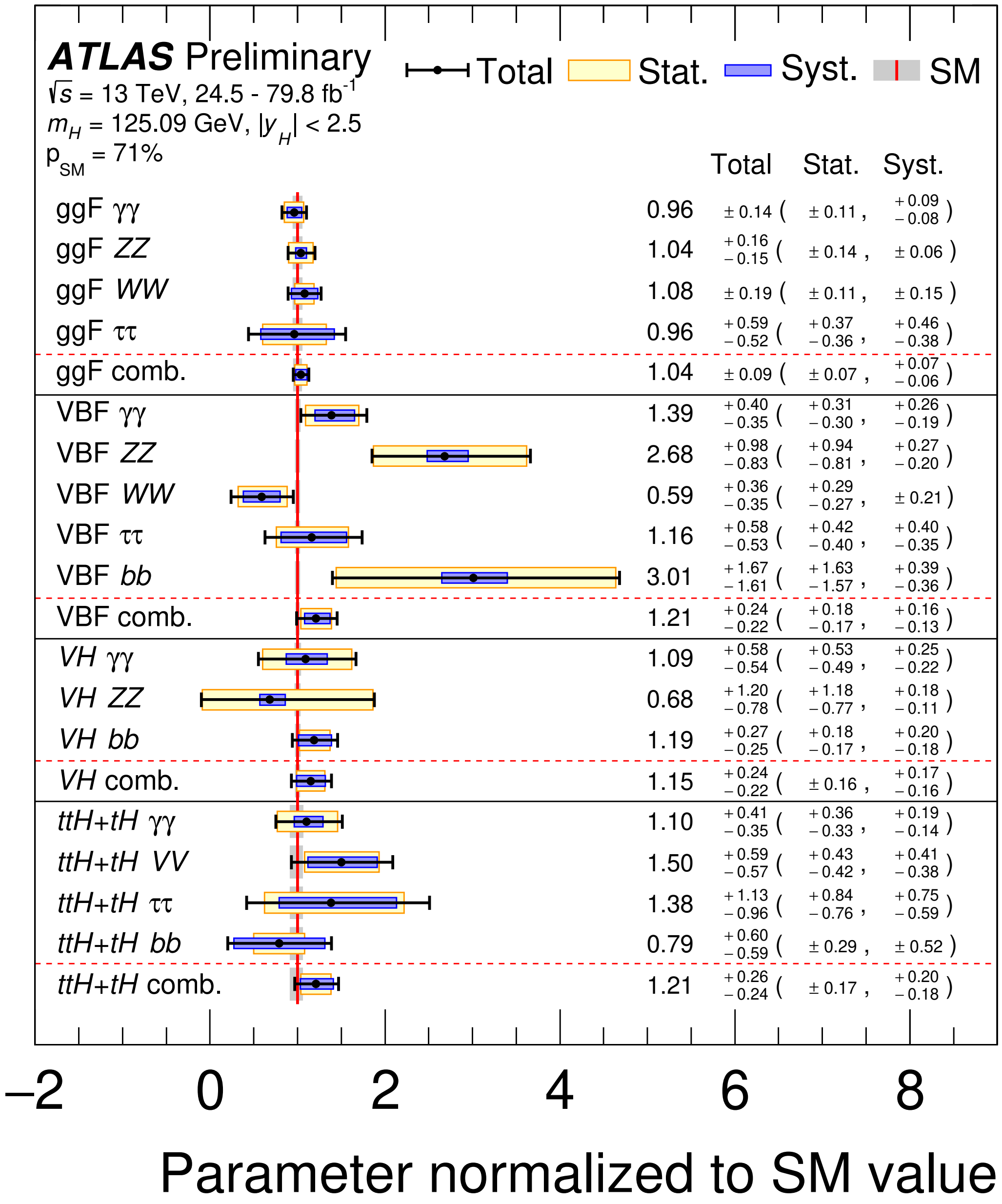

Figure 5: Cross sections times branching fraction for ggF, VBF, VH and $t\bar{t}H$+tH production in each relevant decay mode, normalized to their SM predictions. The values are obtained from a simultaneous fit to all channels. The cross sections of the ggF, $H \to b\bar{b}$, VH, $H \to WW^*$ and VH, $H \to \tau\tau$ processes are fixed to their SM predictions. Combined results for each production mode are also shown, assuming SM values for the branching ratios into each decay mode. The black error bars, blue boxes and yellow boxes show the total, systematic, and statistical uncertainties in the measurements, respectively. The gray bands show the theory uncertainties in the predictions.

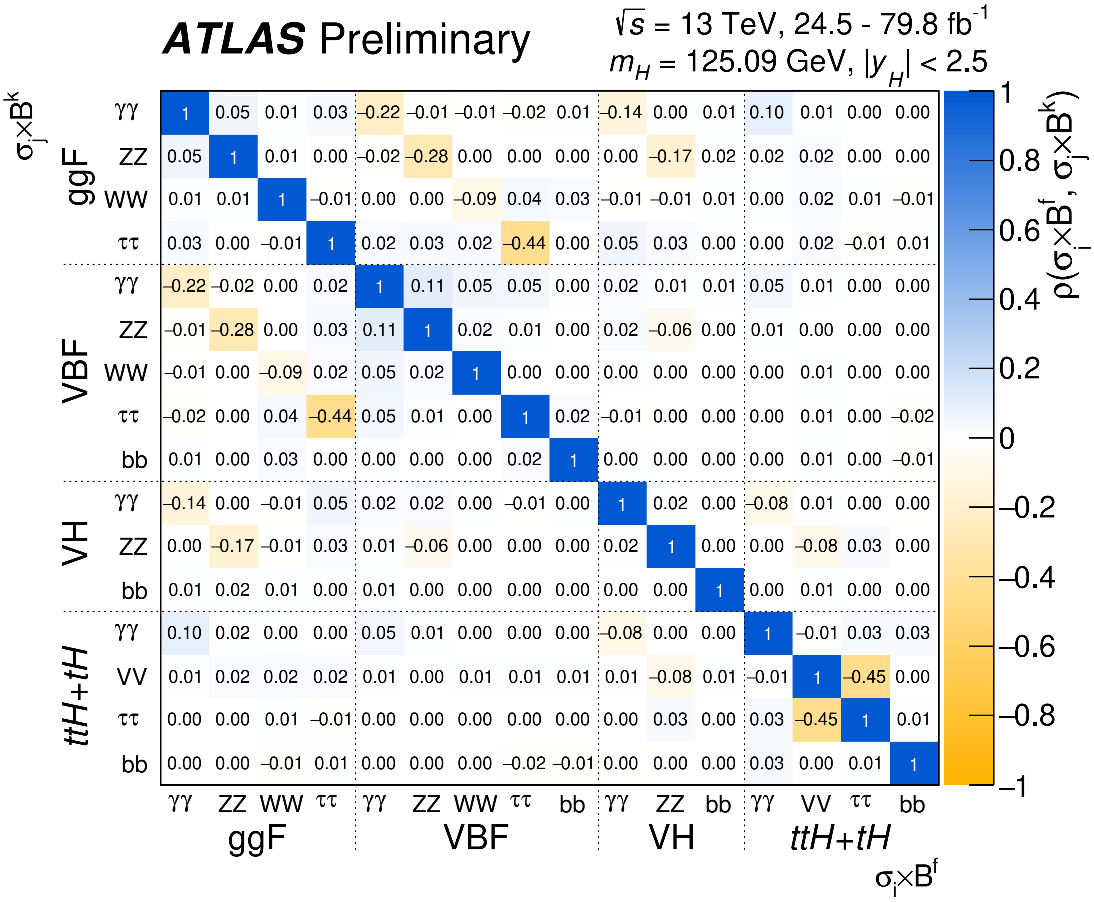

		ggF				VBF					VH			*ttH*+*tH*			
		γγ	ZZ	WW	ττ	γγ	ZZ	WW	ττ	bb	γγ	ZZ	bb	γγ	VV	ττ	bb
ggF	γγ	1	0.05	0.01	0.03	−0.22	−0.01	−0.01	−0.02	0.01	−0.14	0.00	0.01	0.10	0.01	0.00	0.00
	ZZ	0.05	1	0.01	0.00	−0.02	−0.28	0.00	0.00	0.00	0.00	−0.17	0.02	0.02	0.02	0.00	0.00
	WW	0.01	0.01	1	−0.01	0.00	0.00	−0.09	0.04	0.03	−0.01	−0.01	0.01	0.00	0.02	0.01	−0.01
	ττ	0.03	0.00	−0.01	1	0.02	0.03	0.02	−0.44	0.00	0.05	0.03	0.00	0.00	0.02	−0.01	0.01
VBF	γγ	−0.22	−0.02	0.00	0.02	1	0.11	0.05	0.05	0.00	0.02	0.01	0.01	0.05	0.01	0.00	0.00
	ZZ	−0.01	−0.28	0.00	0.03	0.11	1	0.02	0.01	0.00	0.02	−0.06	0.00	0.01	0.00	0.00	0.00
	WW	−0.01	0.00	−0.09	0.02	0.05	0.02	1	0.00	0.00	0.00	0.00	0.00	0.00	0.01	0.00	0.00
	ττ	−0.02	0.00	0.04	−0.44	0.05	0.01	0.00	1	0.02	−0.01	0.00	0.00	0.00	0.01	0.00	−0.02
	bb	0.01	0.00	0.03	0.00	0.00	0.00	0.00	0.02	1	0.00	0.00	0.00	0.00	0.01	0.00	−0.01
VH	γγ	−0.14	0.00	−0.01	0.05	0.02	0.02	0.00	−0.01	0.00	1	0.02	0.00	−0.08	0.01	0.00	0.00
	ZZ	0.00	−0.17	−0.01	0.03	0.01	−0.06	0.00	0.00	0.00	0.02	1	0.00	0.00	−0.08	0.03	0.00
	bb	0.01	0.02	0.01	0.00	0.01	0.00	0.00	0.00	0.00	0.00	0.00	1	0.00	0.01	0.00	0.00
ttH+*tH*	γγ	0.10	0.02	0.00	0.00	0.05	0.01	0.00	0.00	0.00	−0.08	0.00	0.00	1	−0.01	0.03	0.03
	VV	0.01	0.02	0.02	0.02	0.01	0.00	0.01	0.01	0.01	0.01	−0.08	0.01	−0.01	1	−0.45	0.00
	ττ	0.00	0.00	0.01	−0.01	0.00	0.00	0.00	0.00	0.00	0.00	0.03	0.00	0.03	−0.45	1	0.01
	bb	0.00	0.00	−0.01	0.01	0.00	0.00	0.00	−0.02	−0.01	0.00	0.00	0.00	0.03	0.00	0.01	1

Figure 6: Correlation matrix for the measured values of the production cross sections times branching ratios of the Higgs boson, for the combinations in which sufficient sensitivity is provided by the input analyses.

5.4 Ratios of cross sections and branching fractions

The products $(\sigma \times \mathrm{B})_{if}$ described in Section 5.3 can be expressed as

$$(\sigma \times \mathrm{B})_{if} = \sigma_{\mathrm{ggF}}^{ZZ} \cdot \left(\frac{\sigma_i}{\sigma_{\mathrm{ggF}}}\right) \cdot \left(\frac{\mathrm{B}_f}{\mathrm{B}_{ZZ}}\right), \tag{4}$$

in terms of the cross section times branching ratio $\sigma_{\mathrm{ggF}}^{ZZ}$ for the reference process $gg \to H \to ZZ^*$, which is precisely measured and exhibits small systematic uncertainties, ratios of production cross sections to that of ggF, $\sigma_i/\sigma_{\mathrm{ggF}}$, and ratios of branching fractions to that of $H \to ZZ^*$, $\mathrm{B}_f/\mathrm{B}_{ZZ}$.

Results are shown in Figure 7 and Table 7.

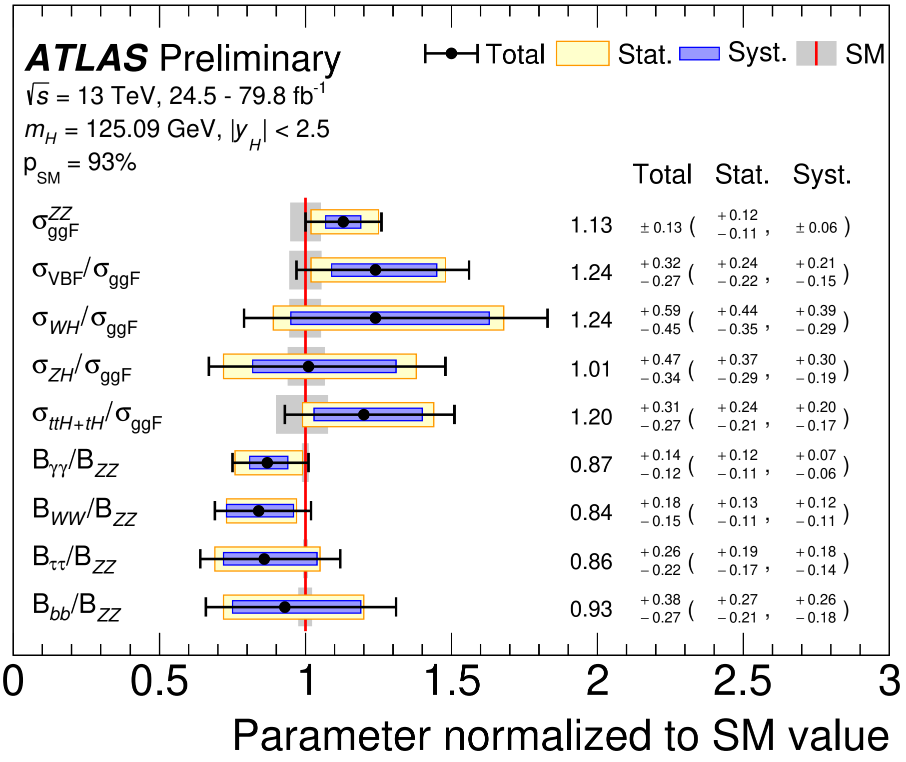

Figure 7: Results of a simultaneous fit for $\sigma_{\mathrm{ggF}}^{ZZ}$, $\sigma_{\mathrm{VBF}}/\sigma_{\mathrm{ggF}}$, $\sigma_{WH}/\sigma_{\mathrm{ggF}}$, $\sigma_{ZH}/\sigma_{\mathrm{ggF}}$, $\sigma_{t\bar{t}H+tH}/\sigma_{\mathrm{ggF}}$, $\mathrm{B}_{\gamma\gamma}/\mathrm{B}_{ZZ}$, $\mathrm{B}_{WW}/\mathrm{B}_{ZZ}$, $\mathrm{B}_{\tau\tau}/\mathrm{B}_{ZZ}$, and $\mathrm{B}_{bb}/\mathrm{B}_{ZZ}$. The fit results are normalized to the SM predictions. The black error bars, blue boxes and yellow boxes show the total, systematic, and statistical uncertainties in the measurements, respectively. The gray bands show the theory uncertainties in the predictions.

The compatibility between the measurements and the SM predictions corresponds to a p-value of $p_{\mathrm{SM}} = 93\%$, computed using the procedure outlined in Section 4 with 9 degrees of freedom.

Table 7: Best-fit values and uncertainties of σ_{ggF}^{ZZ}, together with ratios of production cross sections normalized to σ_{ggF}, and ratios of branching fractions normalized to B_{ZZ}. Uncertainties in the SM predictions are computed following the same method as for Ref. [3].

Quantity	Value	Uncertainty					SM prediction
		Total	Stat.	Exp.	SigTheo.	BkgTheo.	
σ_{ggF}^{ZZ} [pb]	1.33	± 0.15	$^{+0.14}_{-0.13}$	± 0.06	± 0.02	± 0.04	1.181 ± 0.061
$\sigma_{\text{VBF}}/\sigma_{\text{ggF}}$	0.097	$^{+0.025}_{-0.021}$	$^{+0.019}_{-0.017}$	$^{+0.010}_{-0.008}$	$^{+0.011}_{-0.008}$	$^{+0.006}_{-0.005}$	0.0786 ± 0.0043
$\sigma_{WH}/\sigma_{\text{ggF}}$	0.034	$^{+0.016}_{-0.012}$	$^{+0.012}_{-0.009}$	$^{+0.008}_{-0.006}$	$^{+0.003}_{-0.002}$	$^{+0.007}_{-0.005}$	$0.0269^{+0.0014}_{-0.0015}$
$\sigma_{ZH}/\sigma_{\text{ggF}}$	0.0180	$^{+0.0084}_{-0.0062}$	$^{+0.0066}_{-0.0052}$	$^{+0.0034}_{-0.0021}$	$^{+0.0016}_{-0.0009}$	$^{+0.0037}_{-0.0025}$	$0.0178^{+0.0011}_{-0.0010}$
$\sigma_{t\bar{t}H+tH}/\sigma_{\text{ggF}}$	0.0157	$^{+0.0041}_{-0.0035}$	$^{+0.0031}_{-0.0029}$	$^{+0.0020}_{-0.0017}$	$^{+0.0012}_{-0.0008}$	$^{+0.0013}_{-0.0012}$	$0.0131^{+0.0010}_{-0.0013}$
$\text{B}_{\gamma\gamma}/\text{B}_{ZZ}$	0.075	$^{+0.012}_{-0.010}$	$^{+0.010}_{-0.009}$	$^{+0.006}_{-0.005}$	$^{+0.002}_{-0.001}$	± 0.002	0.0860 ± 0.0010
$\text{B}_{WW}/\text{B}_{ZZ}$	6.8	$^{+1.5}_{-1.2}$	$^{+1.1}_{-0.9}$	$^{+0.8}_{-0.7}$	± 0.2	$^{+0.6}_{-0.5}$	$8.15 \pm < 0.01$
$\text{B}_{\tau\tau}/\text{B}_{ZZ}$	2.04	$^{+0.62}_{-0.52}$	$^{+0.45}_{-0.40}$	$^{+0.36}_{-0.31}$	$^{+0.17}_{-0.09}$	$^{+0.12}_{-0.09}$	2.369 ± 0.017
$\text{B}_{bb}/\text{B}_{ZZ}$	20.5	$^{+8.4}_{-6.2}$	$^{+6.2}_{-4.6}$	$^{+3.7}_{-2.4}$	$^{+1.3}_{-0.9}$	$^{+4.2}_{-2.9}$	22.00 ± 0.51

6 Combined measurements of simplified template cross sections

6.1 Simplified template cross section framework

Simplified template cross sections [26, 27] are defined through a partition of the phase space of the SM Higgs production process into a set of non-overlapping regions. These regions are defined in terms of the kinematics of the Higgs boson and, when they are present, of associated jets and W and Z bosons, independently of the Higgs boson decay process. They are chosen according to three criteria: sensitivity to deviations from the SM expectation, avoidance of large theory uncertainties in the corresponding SM predictions, and to approximately match experimental selections so as to minimize model-dependent extrapolations. Analysis selections do not however necessarily correspond exactly to the STXS regions.

All regions are defined for a Higgs boson rapidity y_H satisfying $|y_H| < 2.5$, corresponding approximately to the region of experimental sensitivity. Jets are reconstructed from all stable particles with a lifetime greater than 10 ps, excluding the Higgs decay products, using the anti-k_t algorithm with a jet radius parameter $R = 0.4$, and must have a transverse momentum $p_{\text{T,jet}} > 30$ GeV.

The measurements presented in this note are based on the Stage 1 splitting of the STXS framework [26]. Higgs boson production is first classified according to the nature of the initial state and of associated particles, the latter including the decay products of W and Z bosons if they are present. These categories are, by order of decreasing selection priority: $t\bar{t}H$ and tH processes; $qq \to Hqq$ processes, with contributions from both VBF production and quark-initiated VH production with a hadronic decay of the gauge boson; $gg \to ZH$ with $Z \to q\bar{q}$; VH production with a leptonic decay of the vector boson (V(lep)H), including $gg \to ZH$ production; and finally the gluon fusion process. The latter is considered together with

$gg \to ZH$, $Z \to q\bar{q}$ production, as a single $gg \to H$ process. The $b\bar{b}H$ production mode is modeled as a 1% [26] increase of the $gg \to H$ yield in each STXS bin, since the acceptances for both processes are similar for all input analyses [26]. The $t\bar{t}H$ and tH processes are also combined in a single $t\bar{t}H$+tH category, assuming the relative fraction of each component to be as in the SM, within uncertainties.

The analyses included in this note provide only limited sensitivity to the cross-section in some bins of the Stage 1 scheme, in particular due to limited data statistics in some regions. In other cases, they only provide sensitivity to a combination of bins, leading to strongly correlated measurements. To mitigate these effects, the results are presented in terms of a reduced splitting, with the measurement bins defined as merged groups of Stage 1 bins (and in the case V(lep)H with an additional splitting not present in the original Stage 1 scheme, as described below). These measurement bins are defined as follows for each process:

- $\boldsymbol{gg \to H}$ is separated into regions defined by the jet multiplicity and the Higgs boson transverse momentum p_{T}^{H}. A region is defined for events with one or more jets and $p_{\mathrm{T}}^{H} \geq 200$ GeV, providing sensitivity to deviations from the SM at high momentum transfer. The remaining events are separated into classes with 0, 1 and ≥ 2 jets in the final state. The one-jet category is further split in bins of p_{T}^{H}, probing perturbative QCD predictions and providing sensitivity to deviations from the SM. Three bins are defined with $p_{\mathrm{T}}^{H} < 60$ GeV, $60\ \mathrm{GeV} \leq p_{\mathrm{T}}^{H} < 120$ GeV and $120\ \mathrm{GeV} \leq p_{\mathrm{T}}^{H} < 200$ GeV.
- $\boldsymbol{qq \to Hqq}$ is separated into three regions. The first selects events in which the transverse momentum of the leading jet p_{T}^{j} is ≥ 200 GeV. A second region, denoted as *VH topo*, is defined by $p_{\mathrm{T}}^{j} < 200$ GeV and the presence of two jets with an invariant mass m_{jj} in the range $60 \leq m_{jj} < 120$ GeV, selecting in particular events originating from VH production. The remaining events are grouped into a third bin, denoted as *VBF topo + Rest*, which includes in particular the VBF-topology region defined by the presence of two jets with $m_{jj} \geq 400$ GeV and a pseudorapidity difference $|\Delta\eta_{jj}| \geq 2.8$, as well as events that fall in none of the above selections. The measurement sensitivity of the corresponding cross-section is dominated by the VBF-topology region which is measured precisely by the analyses targeting VBF production.
- $\boldsymbol{V}$**(lep)**$\boldsymbol{H}$ is split into the two processes $qq \to WH$ and $pp \to ZH$, the latter including both quark-initiated and gluon-initiated production. These regions are further split according to p_{T}^{V}, the transverse momentum of the W or Z. For the $qq \to WH$ process two bins are defined for $p_{\mathrm{T}}^{V} \leq 250$ GeV and $p_{\mathrm{T}}^{V} > 250$ GeV, while for $pp \to ZH$ three bins are defined for $p_{\mathrm{T}}^{V} < 150$ GeV, $150\ \mathrm{GeV} \leq p_{\mathrm{T}}^{V} < 250$ GeV and $p_{\mathrm{T}}^{V} \geq 250$ GeV. This definition deviates from the one given in Ref. [26], where the $qq \to ZH$ and $gg \to ZH$ processes are measured separately and no splitting is performed at $p_{\mathrm{T}}^{V} = 250$ GeV for $gg \to ZH$, given the limited sensitivity of the current measurements to separating the $qq \to ZH$ and $gg \to ZH$ processes.

The above merging scheme of Stage 1 bins is summarized in Figure 8.

Sensitivity to the 0-jet and 1-jet, $p_{\mathrm{T}}^{H} < 60$ GeV regions of the $gg \to H$ process is provided mainly by the $H \to ZZ^* \to 4\ell$, $H \to \gamma\gamma$ and $H \to WW^* \to e\nu\mu\nu$ analyses, with the leading contribution in each region coming from $H \to WW^* \to e\nu\mu\nu$ and $H \to \gamma\gamma$ respectively. For the 1-jet, $60 \leq p_{\mathrm{T}}^{H} < 120$ GeV region, the main contributions to sensitivity are from $H \to ZZ^* \to 4\ell$ and $H \to \gamma\gamma$, dominated by the latter. The $H \to \gamma\gamma$ analysis also provides the largest sensitivity in the rest of the $gg \to H$ regions as well as in the $qq \to Hqq$ sector, apart from the $p_{\mathrm{T}}^{j} > 200$ GeV region for which $H \to \tau\tau$ dominates the sensitivity. The VH, $H \to b\bar{b}$ analysis provides the most sensitive measurements in the V(lep)H regions. Finally, the $H \to \gamma\gamma$ and $t\bar{t}H$ multilepton analyses provide the leading contributions to the measurement of the $t\bar{t}H$+tH region.

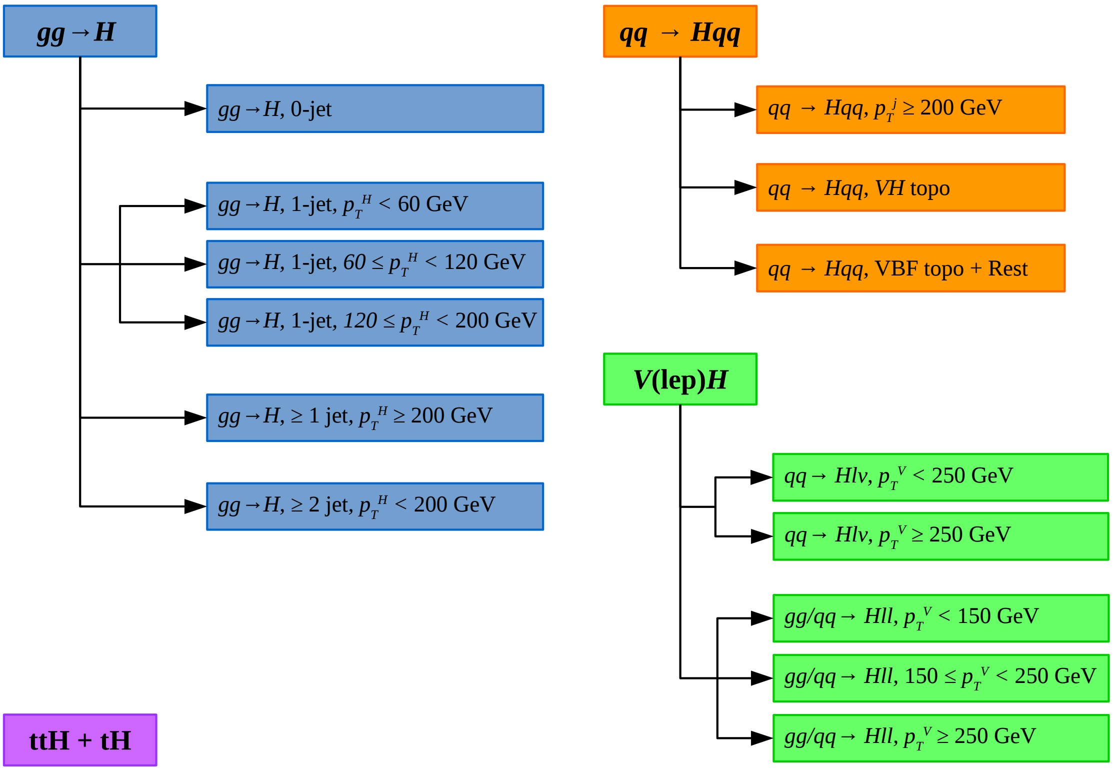

Figure 8: Definition of the STXS measurement regions used in this note. For each Higgs boson production process, the regions are defined starting from the top of the corresponding schematic, with regions nearer the top taking precedence in case of overlapping selections. The $b\bar{b}H$ production mode is considered as part of $gg \to H$.

The measurement is performed as described by Eq. 1, with parameters of interest of the form $(\sigma \times \mathrm{B})_{if}$ denoting the cross section times branching ratio in STXS region i and decay channel f. The acceptance factors $(\epsilon \times A)^{k}_{if}$ for each analysis category k are determined from SM Higgs boson production processes, modeled using the samples described in Section 2, and act as templates in the fits of the STXS cross sections to the data. The dependence on the theory assumptions is reduced compared to the measurement of the total cross sections in each production mode, since the $(\epsilon \times A)^{k}_{if}$ are computed over smaller regions. Assumptions on the kinematics within a given STXS region lead to some model-dependence, which can be reduced further using a finer splitting the phase space as justified by the experimental precision.

Theory uncertainties for the $gg \to H$ and $qq \to Hqq$ processes are defined as in Ref. [4], while those of the $V(\mathrm{lep})H$ process follow the scheme described in [106]. For the measurement bins defined by merging several bins of the STXS Stage-1 framework, the $(\epsilon \times A)$ factors are determined assuming that the relative fractions of each Stage-1 bin in the total are as in the SM, and SM uncertainties on these fractions are included in the measurement.

6.2 Results

The parameters used for the combined STXS measurements are the cross sections for Higgs boson production in STXS region i times the branching fraction for the $H \to ZZ^*$ decay, $(\sigma \times \mathrm{B})_{i,ZZ}$, and the ratios of branching fractions $\mathrm{B}_f/\mathrm{B}_{ZZ}$ for the other final states f. As for the ratio model of Section 5.4, the cross sections times branching ratios for final states other than ZZ are parametrized as

$$(\sigma \times \mathrm{B})_{if} = (\sigma \times \mathrm{B})_{i,ZZ} \cdot \left(\frac{\mathrm{B}_f}{\mathrm{B}_{ZZ}}\right). \tag{5}$$

The results are shown in Figures 9 and 10 and in Table 8. The observed upper limits at 95% CL on the cross sections in the $qq \to Hqq$, $(V \to q\bar{q})H$ and $qq \to Hqq$, $p_T^j \geq 200$ GeV bins are set at 1.45 pb and 0.59 pb, respectively, taking into account the physical boundary on the parameter values as discussed in Section 4. The corresponding expected upper limits are set at 1.53 pb and 0.80 pb, respectively.

The correlations between the measured parameters are shown in Figure 11. The largest anti-correlations are between $\mathrm{B}_{b\bar{b}}/\mathrm{B}_{ZZ}$ and the cross-section measurements in the $V(\mathrm{lep})H$ region, since the VH, $H \to b\bar{b}$ analysis is sensitive to products of these quantities; between the cross-section measurement in the $gg \to H$ 0-jet region and both $\mathrm{B}_{\gamma\gamma}/\mathrm{B}_{ZZ}$ and $\mathrm{B}_{WW}/\mathrm{B}_{ZZ}$, since the $H \to \gamma\gamma$, $H \to ZZ^* \to 4\ell$ and $H \to WW^* \to e\nu\mu\nu$ decay channels provide the most precise measurements in this region; between $\mathrm{B}_{\gamma\gamma}/\mathrm{B}_{ZZ}$ and the cross-section measurement in the $qq \to Hqq$, $p_T^j < 200$ GeV region, since there is a tension between the $H \to \gamma\gamma$ and $H \to ZZ^* \to 4\ell$ measurements in this region; between $\mathrm{B}_{\tau\tau}/\mathrm{B}_{ZZ}$ and the cross-section measurement in the $p_{\mathrm{T}}^H > 200\,\mathrm{GeV}$ region, since the high-p_{T}^H channels of the $H \to \tau\tau$ analysis are sensitive to their product; and between the cross-section measurements in the $qq \to Hqq$, $p_T^j \geq 200$ GeV and $gg \to H$, $\geq$ 1-jet, $p_{\mathrm{T}}^H \geq 200$ GeV regions on the one hand, and the $qq \to Hqq$, $p_T^j \geq 200$ GeV and $gg \to H$, 1-jet, $120 \leq p_{\mathrm{T}}^H < 200$ GeV regions on the other hand, since in both cases there is cross-contamination between these processes in the experimental selections.

The largest positive correlations are between the $(W \to \ell\nu)H$ and $(Z \to \ell\ell)H$ measurement regions, related to their strong anti-correlation with $\mathrm{B}_{b\bar{b}}/\mathrm{B}_{ZZ}$; and between $\mathrm{B}_{\gamma\gamma}/\mathrm{B}_{ZZ}$ and $\mathrm{B}_{WW}/\mathrm{B}_{ZZ}$, due to their strong anti-correlation with the cross-section measurement in the 0-jet region.

The results show good overall agreement with the SM predictions in a range of kinematic regions of Higgs boson production processes. The compatibility between the measurement and the SM prediction corresponds to a p-value of $p_{\mathrm{SM}} = 88\%$, computed using the procedure outlined in Section 4 with 19 degrees of freedom.

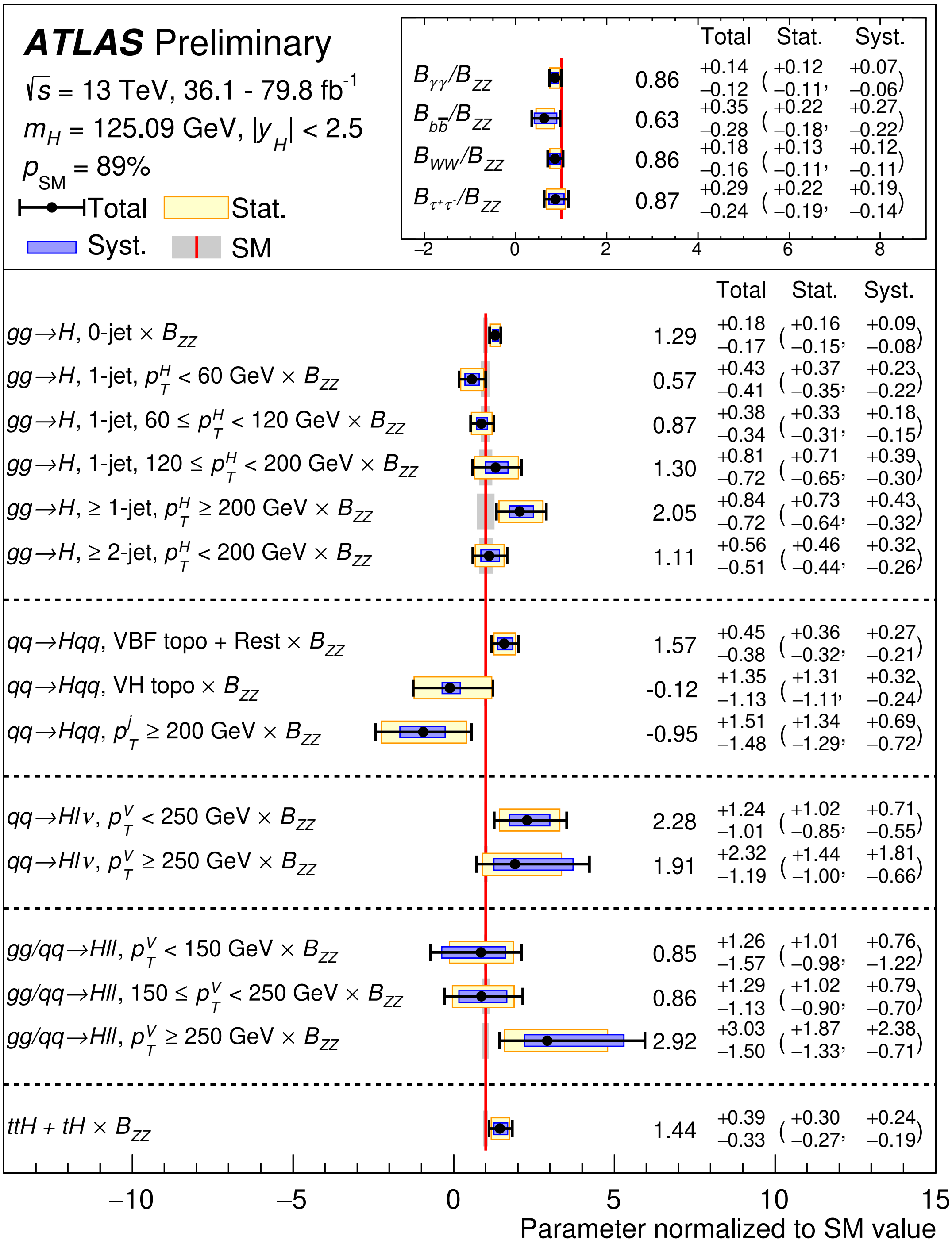

Figure 9: Best-fit values and uncertainties of the cross sections in each measurement region and of the ratios of branching fractions $\mathrm{B}_f/\mathrm{B}_{4\ell}$, normalized to the SM predictions for the various parameters. The parameters directly extracted from the fit are the products $(\sigma_i \times \mathrm{B}_{ZZ})$ and the ratios $\mathrm{B}_f/\mathrm{B}_{ZZ}$. The black error bar shows the total uncertainty on each measurement.

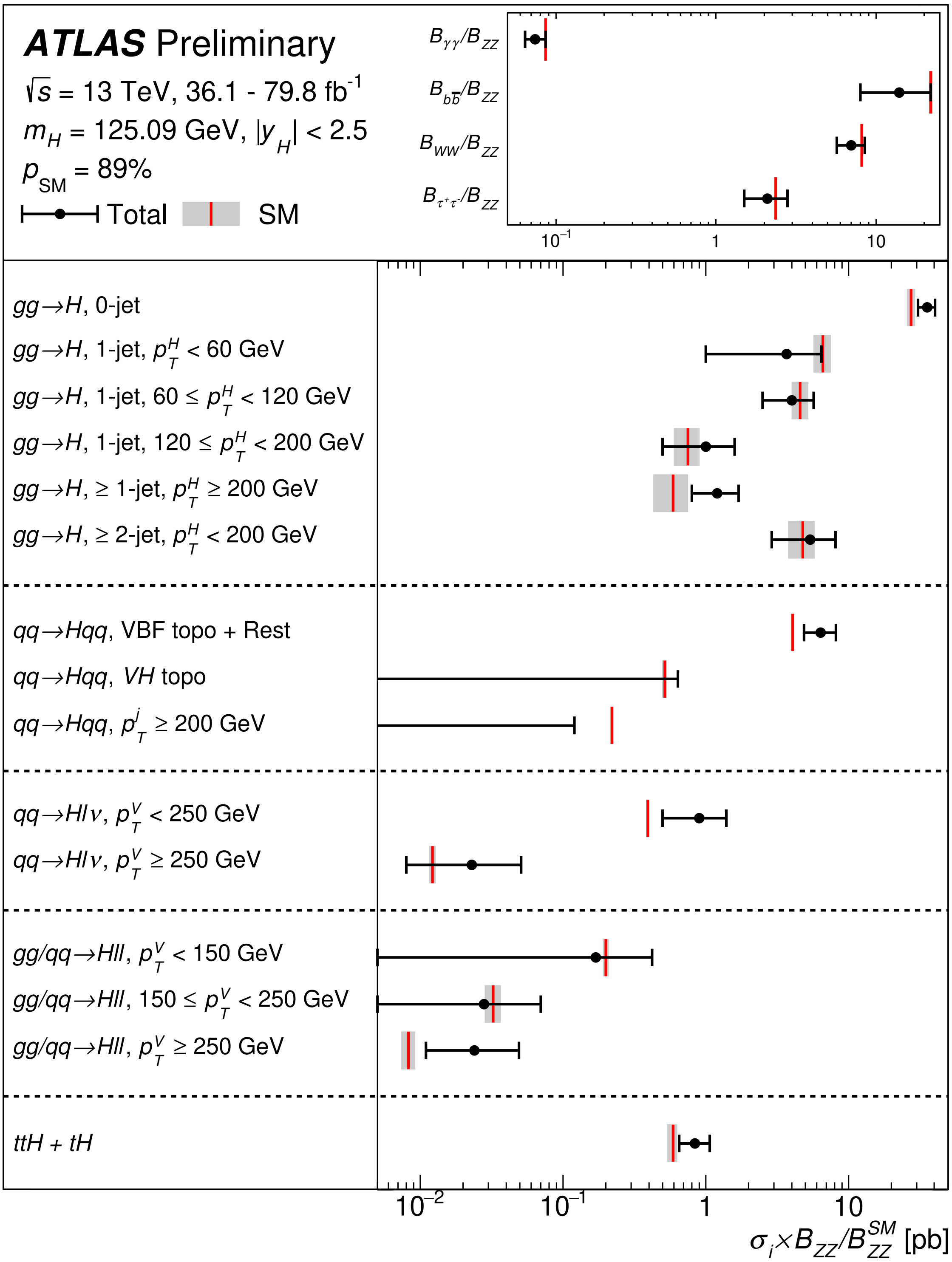

Figure 10: Best-fit values and uncertainties of the cross sections in each measurement region and of the ratios of branching fractions $B_f/B_{4\ell}$. The parameters directly extracted from the fit are the products $(\sigma_i \times B_{ZZ})$ and the ratios B_f/B_{ZZ}; the former are shown divided by the SM value of B_{ZZ} for presentation purposes. The black error bar shows the total uncertainty on each measurement.

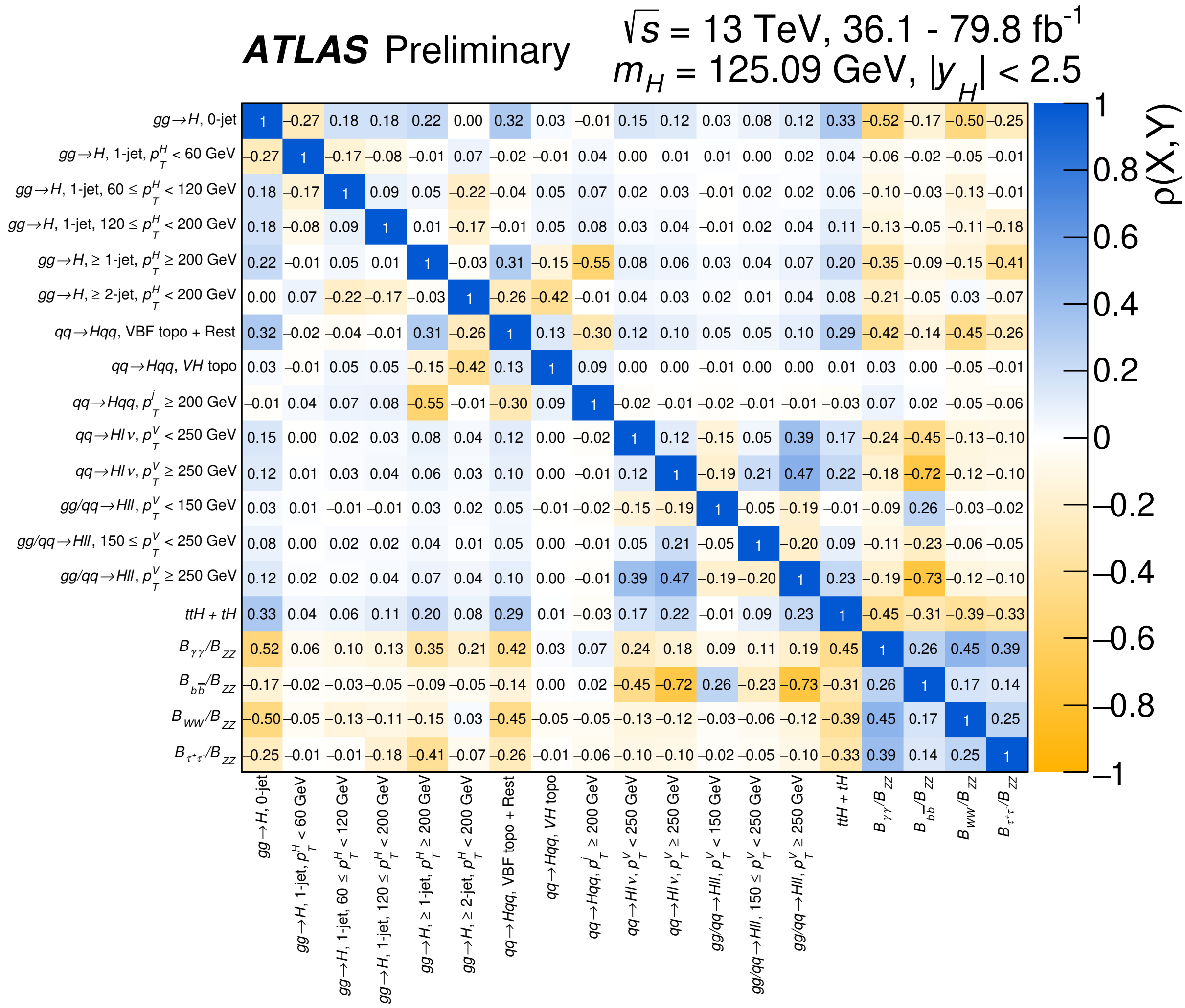

	$gg\to H$, 0-jet	$gg\to H$, 1-jet, $p_T^H < 60$ GeV	$gg\to H$, 1-jet, $60 \le p_T^H < 120$ GeV	$gg\to H$, 1-jet, $120 \le p_T^H < 200$ GeV	$gg\to H$, $\ge$ 1-jet, $p_T^H \ge 200$ GeV	$gg\to H$, $\ge$ 2-jet, $p_T^H < 200$ GeV	$qq\to Hqq$, VBF topo + Rest	$qq\to Hqq$, VH topo	$qq\to Hqq$, $p_T^j \ge 200$ GeV	$qq\to Hl\nu$, $p_T^V < 250$ GeV	$qq\to Hl\nu$, $p_T^V \ge 250$ GeV	$gg/qq\to Hll$, $p_T^V < 150$ GeV	$gg/qq\to Hll$, $150 \le p_T^V < 250$ GeV	$gg/qq\to Hll$, $p_T^V \ge 250$ GeV	$ttH + tH$	$B_{\gamma\gamma}/B_{ZZ}$	$B_{b\bar{b}}/B_{ZZ}$	B_{WW}/B_{ZZ}	$B_{\tau^+\tau^-}/B_{ZZ}$
$gg\to H$, 0-jet	1	−0.27	0.18	0.18	0.22	0.00	0.32	0.03	−0.01	0.15	0.12	0.03	0.08	0.12	0.33	−0.52	−0.17	−0.50	−0.25
$gg\to H$, 1-jet, $p_T^H < 60$ GeV	−0.27	1	−0.17	−0.08	−0.01	0.07	−0.02	−0.01	0.04	0.00	0.01	0.01	0.00	0.02	0.04	−0.06	−0.02	−0.05	−0.01
$gg\to H$, 1-jet, $60 \le p_T^H < 120$ GeV	0.18	−0.17	1	0.09	0.05	−0.22	−0.04	0.05	0.07	0.02	0.03	−0.01	0.02	0.02	0.06	−0.10	−0.03	−0.13	−0.01
$gg\to H$, 1-jet, $120 \le p_T^H < 200$ GeV	0.18	−0.08	0.09	1	0.01	−0.17	−0.01	0.05	0.08	0.03	0.04	−0.01	0.02	0.04	0.11	−0.13	−0.05	−0.11	−0.18
$gg\to H$, $\ge$ 1-jet, $p_T^H \ge 200$ GeV	0.22	−0.01	0.05	0.01	1	−0.03	0.31	−0.15	−0.55	0.08	0.06	0.03	0.04	0.07	0.20	−0.35	−0.09	−0.15	−0.41
$gg\to H$, $\ge$ 2-jet, $p_T^H < 200$ GeV	0.00	0.07	−0.22	−0.17	−0.03	1	−0.26	−0.42	−0.01	0.04	0.03	0.02	0.01	0.04	0.08	−0.21	−0.05	0.03	−0.07
$qq\to Hqq$, VBF topo + Rest	0.32	−0.02	−0.04	−0.01	0.31	−0.26	1	0.13	−0.30	0.12	0.10	0.05	0.05	0.10	0.29	−0.42	−0.14	−0.45	−0.26
$qq\to Hqq$, VH topo	0.03	−0.01	0.05	0.05	−0.15	−0.42	0.13	1	0.09	0.00	0.00	−0.01	0.00	0.00	0.01	0.03	0.00	−0.05	−0.01
$qq\to Hqq$, $p_T^j \ge 200$ GeV	−0.01	0.04	0.07	0.08	−0.55	−0.01	−0.30	0.09	1	−0.02	−0.01	−0.02	−0.01	−0.01	−0.03	0.07	0.02	−0.05	−0.06
$qq\to Hl\nu$, $p_T^V < 250$ GeV	0.15	0.00	0.02	0.03	0.08	0.04	0.12	0.00	−0.02	1	0.12	−0.15	0.05	0.39	0.17	−0.24	−0.45	−0.13	−0.10
$qq\to Hl\nu$, $p_T^V \ge 250$ GeV	0.12	0.01	0.03	0.04	0.06	0.03	0.10	0.00	−0.01	0.12	1	−0.19	0.21	0.47	0.22	−0.18	−0.72	−0.12	−0.10
$gg/qq\to Hll$, $p_T^V < 150$ GeV	0.03	0.01	−0.01	−0.01	0.03	0.02	0.05	−0.01	−0.02	−0.15	−0.19	1	−0.05	−0.19	−0.01	−0.09	0.26	−0.03	−0.02
$gg/qq\to Hll$, $150 \le p_T^V < 250$ GeV	0.08	0.00	0.02	0.02	0.04	0.01	0.05	0.00	−0.01	0.05	0.21	−0.05	1	−0.20	0.09	−0.11	−0.23	−0.06	−0.05
$gg/qq\to Hll$, $p_T^V \ge 250$ GeV	0.12	0.02	0.02	0.04	0.07	0.04	0.10	0.00	−0.01	0.39	0.47	−0.19	−0.20	1	0.23	−0.19	−0.73	−0.12	−0.10
$ttH + tH$	0.33	0.04	0.06	0.11	0.20	0.08	0.29	0.01	−0.03	0.17	0.22	−0.01	0.09	0.23	1	−0.45	−0.31	−0.39	−0.33
$B_{\gamma\gamma}/B_{ZZ}$	−0.52	−0.06	−0.10	−0.13	−0.35	−0.21	−0.42	0.03	0.07	−0.24	−0.18	−0.09	−0.11	−0.19	−0.45	1	0.26	0.45	0.39
$B_{b\bar{b}}/B_{ZZ}$	−0.17	−0.02	−0.03	−0.05	−0.09	−0.05	−0.14	0.00	0.02	−0.45	−0.72	0.26	−0.23	−0.73	−0.31	0.26	1	0.17	0.14
B_{WW}/B_{ZZ}	−0.50	−0.05	−0.13	−0.11	−0.15	0.03	−0.45	−0.05	−0.05	−0.13	−0.12	−0.03	−0.06	−0.12	−0.39	0.45	0.17	1	0.25
$B_{\tau^+\tau^-}/B_{ZZ}$	−0.25	−0.01	−0.01	−0.18	−0.41	−0.07	−0.26	−0.01	−0.06	−0.10	−0.10	−0.02	−0.05	−0.10	−0.33	0.39	0.14	0.25	1

Figure 11: Correlation matrix for the measured values of the simplified template cross sections and ratios of branching fractions. The fit parameters are the products $(\sigma_i \times \mathrm{B}_{ZZ})$ and the ratios $\mathrm{B}_f/\mathrm{B}_{ZZ}$. For the former, the label " $\times\,\mathrm{B}_{ZZ}$" is omitted for presentation purposes.

Table 8: Best-fit values and uncertainties of the cross sections in each measurement region, and of the ratios of branching fractions $\mathrm{B}_f/\mathrm{B}_{ZZ}$. The SM predictions [26] are shown for each quantity. The parameters directly extracted from the fit are the products $(\sigma_i \times \mathrm{B}_{ZZ})$ and the ratios $\mathrm{B}_f/\mathrm{B}_{ZZ}$; the former are shown divided by the SM value of B_{ZZ} for presentation purposes.

Measurement region $\left((\sigma_i \times \mathrm{B}_{ZZ})/\mathrm{B}^{\mathrm{SM}}_{ZZ}\right)$	Result [pb]	Uncertainty [pb]			SM prediction [pb]
		Total	Stat.	Syst.	
$gg \to H$, 0-jet	35.5	$^{+5.0}_{-4.7}$	$^{+4.4}_{-4.1}$	$^{+2.5}_{-2.2}$	27.5 ± 1.8
$gg \to H$, 1-jet, $p_{\mathrm{T}}^{H} < 60$ GeV	3.7	$^{+2.8}_{-2.7}$	$^{+2.4}_{-2.3}$	$^{+1.5}_{-1.4}$	6.6 ± 0.9
$gg \to H$, 1-jet, $60 \leq p_{\mathrm{T}}^{H} < 120$ GeV	4.0	$^{+1.7}_{-1.5}$	$^{+1.5}_{-1.4}$	$^{+0.8}_{-0.7}$	4.6 ± 0.6
$gg \to H$, 1-jet, $120 \leq p_{\mathrm{T}}^{H} < 200$ GeV	1.0	$^{+0.6}_{-0.5}$	± 0.5	$^{+0.3}_{-0.2}$	0.75 ± 0.15
$gg \to H$, $\geq$ 1-jet, $p_{\mathrm{T}}^{H} \geq 200$ GeV	1.2	$^{+0.5}_{-0.4}$	± 0.4	$^{+0.3}_{-0.2}$	0.59 ± 0.16
$gg \to H$, $\geq$ 2-jet, $p_{\mathrm{T}}^{H} < 200$ GeV	5.4	$^{+2.7}_{-2.5}$	$^{+2.2}_{-2.1}$	$^{+1.5}_{-1.3}$	4.8 ± 1.0
$qq \to Hqq$, VBF topo + Rest	6.4	$^{+1.8}_{-1.5}$	$^{+1.5}_{-1.3}$	$^{+1.1}_{-0.9}$	4.07 ± 0.09
$qq \to Hqq$, VH topo	−0.06	$^{+0.70}_{-0.58}$	$^{+0.68}_{-0.57}$	$^{+0.16}_{-0.12}$	0.515 ± 0.019
$qq \to Hqq$, $p_T^{j} \geq 200$ GeV	−0.21	± 0.33	$^{+0.29}_{-0.28}$	$^{+0.15}_{-0.16}$	0.220 ± 0.005
$qq \to H\ell\nu$, $p_T^{V} < 250$ GeV	0.90	$^{+0.49}_{-0.40}$	$^{+0.40}_{-0.33}$	$^{+0.28}_{-0.22}$	0.393 ± 0.009
$qq \to H\ell\nu$, $p_T^{V} \geq 250$ GeV	0.023	$^{+0.028}_{-0.015}$	$^{+0.018}_{-0.012}$	$^{+0.022}_{-0.008}$	0.0122 ± 0.0006
$gg/qq \to H\ell\ell$, $p_T^{V} < 150$ GeV	0.17	$^{+0.25}_{-0.31}$	± 0.20	$^{+0.15}_{-0.24}$	0.200 ± 0.008
$gg/qq \to H\ell\ell$, $150 \leq p_T^{V} < 250$ GeV	0.028	$^{+0.042}_{-0.037}$	$^{+0.033}_{-0.029}$	$^{+0.026}_{-0.023}$	0.0324 ± 0.0041
$gg/qq \to H\ell\ell$, $p_T^{V} \geq 250$ GeV	0.024	$^{+0.025}_{-0.013}$	$^{+0.016}_{-0.011}$	$^{+0.020}_{-0.006}$	0.0083 ± 0.0009
$t\bar{t}H$+tH	0.84	$^{+0.23}_{-0.19}$	$^{+0.18}_{-0.16}$	$^{+0.14}_{-0.11}$	$0.59^{+0.04}_{-0.05}$
Branching fraction ratio	Result	Uncertainty			SM prediction
		Total	Stat.	Syst.	
$\mathrm{B}_{\gamma\gamma}/\mathrm{B}_{ZZ}$	0.074	$^{+0.012}_{-0.010}$	$^{+0.010}_{-0.009}$	$^{+0.006}_{-0.005}$	0.0860 ± 0.0010
$\mathrm{B}_{b\bar{b}}/\mathrm{B}_{ZZ}$	14	$^{+8}_{-6}$	$^{+5}_{-4}$	$^{+6}_{-5}$	22.0 ± 0.5
$\mathrm{B}_{WW}/\mathrm{B}_{ZZ}$	7.0	$^{+1.5}_{-1.3}$	$^{+1.1}_{-0.9}$	$^{+1.0}_{-0.9}$	$8.15 \pm < 0.01$
$\mathrm{B}_{\tau\tau}/\mathrm{B}_{ZZ}$	2.1	$^{+0.7}_{-0.6}$	± 0.5	$^{+0.5}_{-0.3}$	2.37 ± 0.02

7 Interpretation of results in the κ framework

For testing the Higgs boson coupling strengths, production cross sections σ_i, decay branching fractions B_f and the signal-strength parameters μ_{if} defined in Eq. 3 cannot be treated independently, as each observed process involves at least two Higgs boson coupling strengths. Scenarios with a consistent treatment of coupling strengths in Higgs boson production and decay modes are presented in this section.

7.1 Framework for coupling-strength measurements

Coupling strength modifiers $\boldsymbol{\kappa}$ are introduced to study modifications of the Higgs boson couplings related to BSM physics, within a framework [28] (κ-framework) based on the leading-order contributions to each production and decay process. Within the assumptions made in this framework, the Higgs boson production and decay can be factorized, such that the cross section times branching fraction of an individual channel $\sigma(i \to H \to f)$ contributing to a measured signal yield is parametrised as

$$\sigma_i \times \mathrm{B}_f = \frac{\sigma_i(\boldsymbol{\kappa}) \times \Gamma_f(\boldsymbol{\kappa})}{\Gamma_H}, \tag{6}$$

where Γ_H is the total width of the Higgs boson and Γ_f is the partial width for Higgs boson decay to the final state f. For a given production process or decay mode j, the corresponding coupling strength modifier κ_j is defined as

$$\kappa_j^2 = \frac{\sigma_j}{\sigma_j^{\mathrm{SM}}} \quad \text{or} \quad \kappa_j^2 = \frac{\Gamma_j}{\Gamma_j^{\mathrm{SM}}}. \tag{7}$$

The SM expectation, denoted by the label *SM*, by definition corresponds to $\kappa_j = 1$. Modifications of the coupling scale factors also change the Higgs boson total width Γ_H by a factor κ_H, defined as $\kappa_H^2 = \sum_j \mathrm{B}_f^{\mathrm{SM}} \kappa_j^2$.

The total width of the Higgs boson increases beyond modifications of κ_j due to contributions from two additional classes of Higgs boson decays: invisible decays, which are identified through an $E_{\mathrm{T}}^{\mathrm{miss}}$ signature in the analyses described in Section 3.8; and undetected decays, to which none of the analyses included in this combination are sensitive (the latter includes for instance Higgs boson decays to light quarks, or to BSM particles to which none of the input analyses provide appreciable sensitivity). In the SM, the branching ratio for decays to invisible final states is $\sim 0.1\%$, from the $H \to ZZ^* \to 4\nu$ process. BSM contributions to this branching fraction and to the branching fraction to undetected final states are denoted by $\mathrm{B}_{\mathrm{inv}}$ and $\mathrm{B}_{\mathrm{undet}}$ respectively, with the SM corresponding to $\mathrm{B}_{\mathrm{inv}} = \mathrm{B}_{\mathrm{undet}} = 0$. The Higgs boson total width is then expressed as

$$\Gamma_H(\boldsymbol{\kappa}, \mathrm{B}_{\mathrm{inv}}, \mathrm{B}_{\mathrm{undet}}) = \frac{\kappa_H^2(\boldsymbol{\kappa})}{(1 - \mathrm{B}_{\mathrm{inv}} - \mathrm{B}_{\mathrm{undet}})} \Gamma_H^{\mathrm{SM}}. \tag{8}$$

Constraints of $\mathrm{B}_{\mathrm{inv}}$ are provided by the analyses described in Section 3.8, but no direct constraints are included for $\mathrm{B}_{\mathrm{undet}}$. Since its value scales all observed cross sections of on-shell Higgs boson production $\sigma(i \to H \to f)$ through Eqs. 6 and 8, further assumptions about undetected decays must be included in order to interpret these measurements in terms of absolute coupling-strength scale factors κ_j. The simplest assumption is that there are no undetected Higgs boson decays and the invisible branching fraction is as predicted by SM. An alternative, weaker assumption, is to require $\kappa_W \leq 1$ and $\kappa_Z \leq 1$ [28]. A second alternative uses the assumption that the signal strength of off-shell Higgs boson production only depends on the coupling-strength scale factors and not on the total width [94, 95], $\sigma^{\mathrm{off}}(i \to H^* \to f) \sim \kappa_{i,\mathrm{off}}^2 \times \kappa_{f,\mathrm{off}}^2$. If the coupling strengths in off-shell Higgs boson production are furthermore assumed to be identical to those for on-shell Higgs boson production, $\kappa_{j,\mathrm{off}} = \kappa_{j,\mathrm{on}}$, and both the off-shell signal strength and coupling-strength scale factors are independent of the energy scale of Higgs boson production, the Higgs boson total width can be determined from the ratio of off-shell to on-shell signal strengths [18, 107]. These assumptions can also be extended to apply to $\mathrm{B}_{\mathrm{inv}}$ as well as $\mathrm{B}_{\mathrm{undet}}$, as an alternative to the measurements of Section 3.8.

An alternative approach is to rely on measurements of ratios of coupling strength scale factors, which can be measured without assumptions on the Higgs boson total width, since the dependence on Γ_H of each coupling strength cancels in their ratios.

The current LHC data are insensitive to the coupling strength modifiers κ_c and κ_s. Thus, in the following it is assumed that κ_c varies as κ_t and κ_s varies as κ_b. Other coupling modifiers (κ_u, κ_d, and κ_e) are irrelevant for the combination provided they are of order unity. The $gg \rightarrow H$, $H \rightarrow gg$, $gg \rightarrow ZH$, $H \rightarrow \gamma\gamma$ and $H \rightarrow Z\gamma$ processes are loop induced in the SM. The ggH vertex and the $H \rightarrow \gamma\gamma$ process are treated either using effective scale factors κ_g and κ_γ, respectively, or expressed in terms of the more fundamental coupling strength scale factors corresponding to the particles that contribute to the loop, including all interference effects. The $gg \rightarrow ZH$ process is never described using an effective scale factor and always resolved in terms of modifications of the SM Higgs boson couplings to the top quark and the Z boson. This assumption impacts the description of BSM effects in $gg \rightarrow ZH$, since these lead to modified production kinematics [108]. However the effect of introducing an explicit dependence on the transverse momentum of the Z boson in the parameterization was found to have a negligible impact on the results at the current level of experimental precision. Similarly, the $H \rightarrow Z\gamma$ decay is always expressed in terms of the Higgs boson couplings to the W boson and the t quark as no analysis targeting this decay mode is included in the combination. These relations are summarized in Table 9. All uncertainties on the best-fit values shown in the following take into account both the experimental and theoretical systematic uncertainties, following the procedures outlined in Section 4.

Table 9: Parametrizations of Higgs boson production cross sections σ_i, partial decay widths Γ^f, and the total width Γ_H, normalized to their SM values, as functions of the coupling strength modifiers κ. The effect of invisible and undetected decays is not considered in the expression for Γ_H. For effective κ parameters associated with loop processes, the resolved scaling in terms of the modifications of the Higgs boson couplings to the fundamental SM particles is given. The coefficients are derived following the methodology in Ref. [28].

Production	Loops	Interference	Effective modifier	Resolved modifier
$\sigma(\text{ggF})$	✓	$t-b$	κ_g^2	$1.04\,\kappa_t^2 + 0.002\,\kappa_b^2 - 0.04\,\kappa_t\kappa_b$
$\sigma(\text{VBF})$	-	-	-	$0.73\,\kappa_W^2 + 0.27\,\kappa_Z^2$
$\sigma(qq/qg \to ZH)$	-	-	-	κ_Z^2
$\sigma(gg \to ZH)$	✓	$t-Z$	$\kappa_{(ggZH)}$	$2.46\,\kappa_Z^2 + 0.46\,\kappa_t^2 - 1.90\,\kappa_Z\kappa_t$
$\sigma(WH)$	-	-	-	κ_W^2
$\sigma(t\bar{t}H)$	-	-	-	κ_t^2
$\sigma(tHW)$	-	$t-W$	-	$2.91\,\kappa_t^2 + 2.31\,\kappa_W^2 - 4.22\,\kappa_t\kappa_W$
$\sigma(tHq)$	-	$t-W$	-	$2.63\,\kappa_t^2 + 3.58\,\kappa_W^2 - 5.21\,\kappa_t\kappa_W$
$\sigma(b\bar{b}H)$	-	-	-	κ_b^2
Partial decay width				
Γ^{bb}	-	-	-	κ_b^2
Γ^{WW}	-	-	-	κ_W^2
Γ^{gg}	✓	$t-b$	κ_g^2	$1.11\,\kappa_t^2 + 0.01\,\kappa_b^2 - 0.12\,\kappa_t\kappa_b$
$\Gamma^{\tau\tau}$	-	-	-	κ_τ^2
Γ^{ZZ}	-	-	-	κ_Z^2
Γ^{cc}	-	-	-	$\kappa_c^2\ (= \kappa_t^2)$
$\Gamma^{\gamma\gamma}$	✓	$t-W$	κ_γ^2	$1.59\,\kappa_W^2 + 0.07\,\kappa_t^2 - 0.67\,\kappa_W\kappa_t$
$\Gamma^{Z\gamma}$	✓	$t-W$	$\kappa_{(Z\gamma)}^2$	$1.12\,\kappa_W^2 - 0.12\,\kappa_W\kappa_t$
Γ^{ss}	-	-	-	$\kappa_s^2\ (= \kappa_b^2)$
$\Gamma^{\mu\mu}$	-	-	-	κ_μ^2
Total width ($\text{B}_{\text{inv}} = \text{B}_{\text{undet}} = 0$)				
Γ_H	✓	-	κ_H^2	$0.58\,\kappa_b^2 + 0.22\,\kappa_W^2$ $+0.08\,\kappa_g^2 + 0.06\,\kappa_\tau^2$ $+0.03\,\kappa_Z^2 + 0.03\,\kappa_c^2$ $+0.0023\,\kappa_\gamma^2 + 0.0015\,\kappa_{(Z\gamma)}^2$ $+0.0004\,\kappa_s^2 + 0.00022\,\kappa_\mu^2$

7.2 Fermion and gauge boson couplings

The model studied in this section probes the universal coupling strength scale factors $\kappa_V = \kappa_W = \kappa_Z$ for all vector bosons and $\kappa_F = \kappa_t = \kappa_b = \kappa_\tau = \kappa_\mu$ for all fermions. The effective couplings corresponding to the ggH and $H \longrightarrow \gamma\gamma$ vertex loops are resolved in terms of the fundamental SM couplings. It is assumed that there are no invisible or undetected Higgs boson decays, i.e. $\mathrm{B}_{\mathrm{inv}} = \mathrm{B}_{\mathrm{undet}} = 0$. Only the relative sign between κ_V and κ_F is physical. As a negative relative sign has been excluded [3], $\kappa_V \geq 0$ and $\kappa_F \geq 0$ are assumed. These definitions can be applied either globally, yielding two parameters, or separately for each of the five major decay channels, yielding ten parameters, κ_V^f and κ_F^f with the superscript f indicating the decay mode. The best-fit values and uncertainties from a combined fit are

$$\kappa_V = 1.05 \pm 0.04$$
$$\kappa_F = 1.05 \pm 0.09.$$

Figure 12 shows the results of the combined fit in the (κ_V, κ_F) plane as well as the contributions of the individual decay modes in this benchmark model. Both κ_V and κ_F are measured to be compatible with the SM expectation. The compatibility of the SM hypothesis with the best fit point corresponds to a p-value of $p_{\mathrm{SM}} = 41\%$, computed using the procedure outlined in Section 4 with two degrees of freedom. In the combined measurement a linear correlation of 44% between κ_V and κ_F is observed.

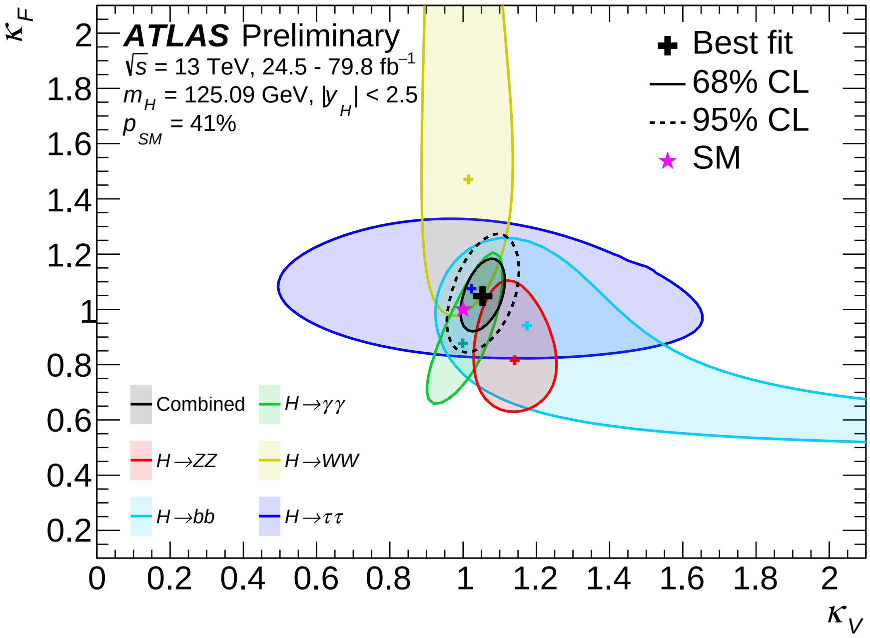

Figure 12: Negative log-likelihood contours at 68% and 95% CL in the (κ_V^f, κ_F^f) plane for the individual decay modes and their combination (κ_F versus κ_V shown in black) assuming the coupling strengths to fermions and vector bosons to be positive. No contributions from invisible or undetected Higgs boson decays are assumed. The best fit value for each measurement is indicated by a cross while the SM hypothesis is indicated by a star.

7.3 Probing BSM contributions in loops and decays

To probe contributions of new particles either though loops or new final states, the effective coupling strengths to photons and gluons κ_γ and κ_g are measured. These parameters are defined to be positive as there is by construction no sensitivity to the sign of these coupling strengths. The modifiers corresponding to other loop-induced processes are resolved. The potential new particles contributing to these vertex loops may or may not contribute to the total width of the Higgs boson through direct invisible or undetected decays. In the former case, the total width is parametrized in terms of the branching fractions $\mathrm{B}_{\mathrm{inv}}$ and $\mathrm{B}_{\mathrm{undet}}$ defined in Section 7.1. Furthermore, the benchmark models studied in this section assume that all coupling strength modifiers of known SM particles are unity, i.e. they follow the SM predictions.

Assuming $\mathrm{B}_{\mathrm{inv}} = \mathrm{B}_{\mathrm{undet}} = 0$, the best-fit values and uncertainties from a combined fit are

$$\begin{aligned}\kappa_\gamma &= 1.00 \pm 0.06 \\ \kappa_g &= 1.03^{+0.07}_{-0.06}.\end{aligned}$$

Figure 13 shows negative log-likelihood contours obtained from the combined fit in the $(\kappa_\gamma, \kappa_g)$ plane. Both κ_γ and κ_g are measured to be compatible with the SM expectation. The compatibility of the SM hypothesis with the best fit point corresponds to a p-value of $p_{\mathrm{SM}} = 88\%$, computed using the procedure outlined in Section 4 with two degrees of freedom. In the combined measurement a linear correlation of -44% between κ_γ and κ_g is observed, in part due to constraining their product by the rate of $H \to \gamma\gamma$ decays in the ggF channel.

To also consider additional contributions to the total width of the Higgs boson, the assumption of no invisible or undetected decays is dropped and $\mathrm{B}_{\mathrm{inv}}$ and $\mathrm{B}_{\mathrm{undet}}$ are included as independent parameters in the model. The measurement sensitive to Higgs boson decays to invisible final states described in Section 3.8 are included in the combination and used to constrain $\mathrm{B}_{\mathrm{inv}}$. The $\mathrm{B}_{\mathrm{undet}}$ parameter is constrained by decay modes that do not involve a loop process. The results from this model are

$$\begin{aligned}\kappa_\gamma &= 0.97 \pm 0.06 \\ \kappa_g &= 0.95 \pm 0.08 \\ \mathrm{B}_{\mathrm{inv}} &< 0.46 \text{ at } 95\% \text{ CL.} \\ \mathrm{B}_{\mathrm{undet}} &< 0.12 \text{ at } 95\% \text{ CL..}\end{aligned}$$

Limits on $\mathrm{B}_{\mathrm{inv}}$ and $\mathrm{B}_{\mathrm{undet}}$ are set using the $\tilde{t}_\mu$ prescription presented in Section 4. The expected upper limits at 95% CL on $\mathrm{B}_{\mathrm{inv}}$ and $\mathrm{B}_{\mathrm{undet}}$ are respectively 0.23 and 0.32. The compatibility of the SM hypothesis with the best fit point corresponds to a p-value of $p_{\mathrm{SM}} = 25\%$, computed using the procedure outlined in Section 4 with four degrees of freedom.

The results for both models are summarized in Fig. 14

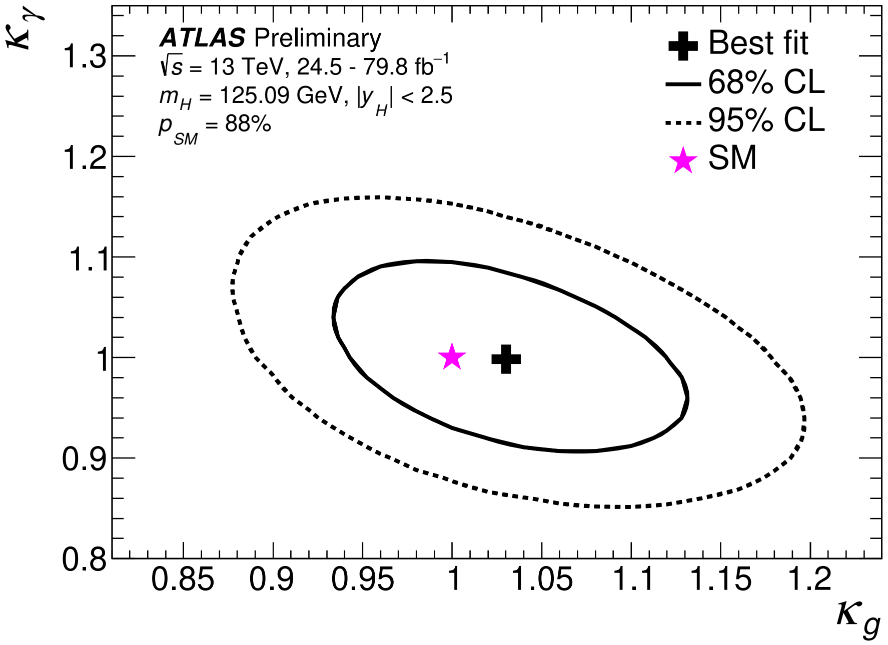

Figure 13: Negative log-likelihood contours at 68% and 95% CL in the $(\kappa_\gamma, \kappa_g)$ plane obtained from a combined fit, constraining all other coupling strength modifiers to their SM values and assuming no contributions from invisible or undetected Higgs boson decays. The best fit value for each measurement is indicated by a cross while the SM hypothesis is indicated by a star.

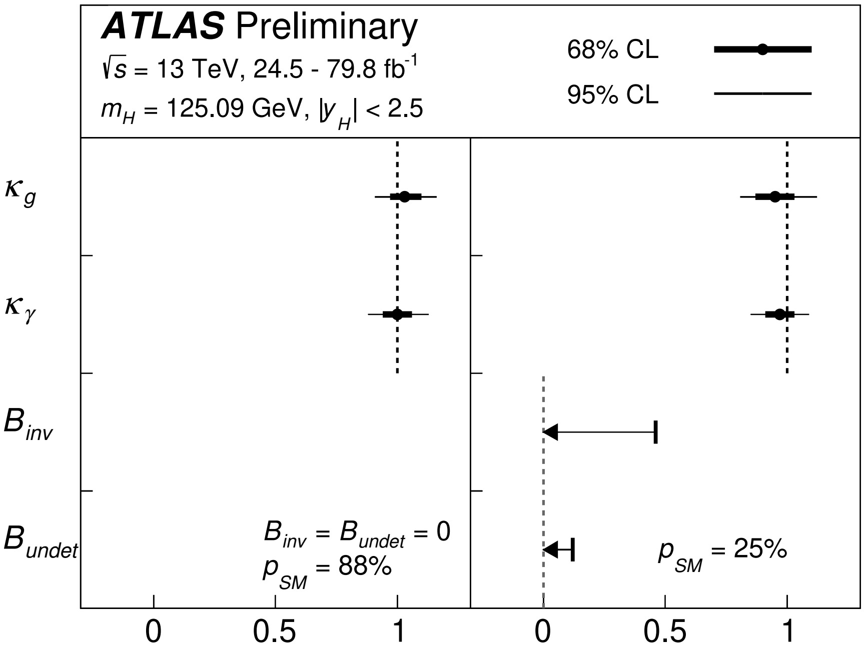

Figure 14: Best-fit values and uncertainties of effective modifiers to the photon and gluon couplings of the Higgs boson, with either $\mathrm{B_{inv}} = \mathrm{B_{undet}} = 0$ (left), or $\mathrm{B_{inv}}$ and $\mathrm{B_{undet}}$ included as free parameters (right). In the latter case, the measurements of the Higgs boson decay rate to invisible final states described in Section 3.8 are included in the combination. The SM corresponds to $\kappa_\gamma = \kappa_g = 1$ and $\mathrm{B_{inv}} = \mathrm{B_{undet}} = 0$. All coupling strength modifiers of known SM particles are assumed to be unity, i.e. they follow the SM predictions.

7.4 Generic parametrization assuming no new particles in loops and decays

In this model the coupling scale factors for the coupling strengths to W, Z, t, b, τ and μ are treated independently. The Higgs boson couplings to second generation quarks are assumed to scale as the couplings to the third generation quarks. SM values are assumed for the couplings to first generation fermions. Furthermore, it is assumed that only SM particles contribute to Higgs boson vertices involving loops, and modifications of the coupling strength scale factors for fermions and vector bosons are propagated through the loop calculations. No invisible or undetected Higgs boson decays are assumed to exist. All coupling strength scale factors are assumed to be positive. The results of the $H \to \mu\mu$ analysis are included for this specific benchmark model. The results are shown in Table 10. The expected 95% upper limit on κ_μ is 1.79. All measured coupling-strength scale factors in this generic model are found to be compatible with their SM expectation. The compatibility of the SM hypothesis with the best fit point corresponds to a p-value of $p_{\mathrm{SM}} = 76\%$, computed using the procedure outlined in Section 4 with six degrees of freedom. Figure 15 shows the results of this benchmark model in terms of reduced coupling strength scale factors

$$y_{V,i} = \sqrt{\kappa_{V,i}\frac{g_{V,i}}{2v}} = \sqrt{\kappa_{V,i}}\frac{m_{V,i}}{v} \tag{9}$$

for weak bosons with a mass m_V, where $g_{V,i}$ is the absolute Higgs boson coupling strength, $v = 246\,\mathrm{GeV}$ is the vacuum expectation value of the Higgs field and

$$y_{F,i} = \kappa_{F,i}\frac{g_{F,i}}{\sqrt{2}} = \kappa_{F,i}\frac{m_{F,i}}{v} \tag{10}$$

for fermions as a function of the particle mass m_F, assuming a SM Higgs boson with a mass of 125.09 GeV. For the b-quark mass the $\overline{MS}$ running mass evaluated at a scale of 125.09 GeV is assumed.

Table 10: Fit results for κ_Z, κ_W, κ_b, κ_t, κ_τ and κ_μ, all assumed to be positive. In this benchmark model no BSM contributions to Higgs boson decays are assumed to exist and Higgs boson vertices involving loops are resolved in terms of their SM content. The upper limit on κ_μ is set using the CL$_s$ prescription.

Parameter	Result
κ_Z	1.10 ± 0.08
κ_W	1.05 ± 0.08
κ_b	$1.06^{+0.19}_{-0.18}$
κ_t	$1.02^{+0.11}_{-0.10}$
κ_τ	1.07 ± 0.15
κ_μ	< 1.51 at 95% CL.

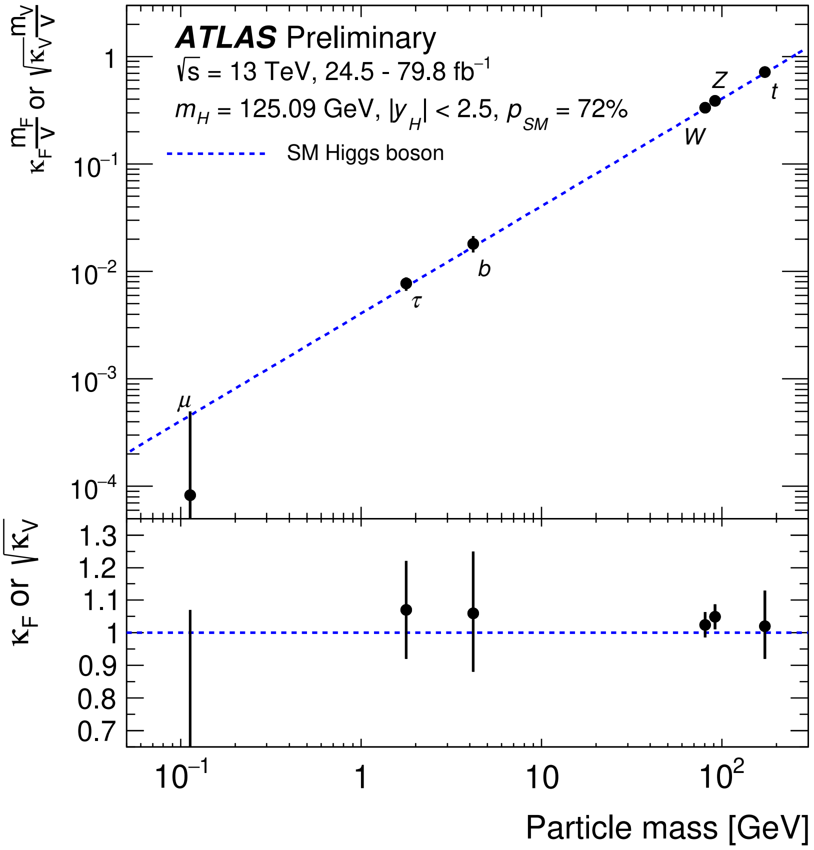

Figure 15: Reduced coupling strength modifiers $\kappa_F \frac{m_F}{v}$ for fermions ($F = t, b, \tau, \mu$) and $\sqrt{\kappa_V}\frac{m_V}{v}$ for weak gauge bosons ($V = W, Z$) as a function of their masses m_F and m_V, respectively, and the vacuum expectation value of the Higgs field $v = 246$ GeV. The SM prediction for both cases is also shown (dotted line). The couplings modifiers κ_F and κ_V are measured assuming no BSM contributions to the Higgs boson decays, and the SM structure of loop processes such as ggF, $H \to \gamma\gamma$ and $H \to gg$. The lower inset shows the ratios of the values to their SM predictions.

7.5 Generic parameterization including effective photon and gluon couplings with and without BSM contributions in decays

The models considered in this section are based on the same parameterization as the one in Section 7.4 but the ggF, $H \to gg$ and $H \to \gamma\gamma$ loop processes are parameterized using the effective coupling strength modifiers κ_g and κ_γ, similar to the benchmark model probed in Section 7.3.

The measured parameters include κ_Z, κ_W, κ_b, κ_t, κ_τ, κ_γ and κ_g. The sign of κ_t can be either positive or negative, while κ_Z is assumed to be positive without loss of generality. All other model parameters are also assumed to be positive. Three alternative scenarios are considered for the total width of the Higgs boson:

(a) No BSM contributions to the total width ($B_{\text{inv}} = B_{\text{undet}} = 0$).

(b) Both B_{inv} and B_{undet} are added as free parameters to the model. The measurements of Higgs boson decays to invisible final states described in Section 3.8 are included in the combination, for these results only, and used to provide a constraint on B_{inv}. The conditions $\kappa_W \leq 1$ and $\kappa_Z \leq 1$ are used to provide a constraint on B_{undet} as discussed in Section 7.1.

(c) A single free parameter $B_{\text{BSM}} = B_{\text{inv}} = B_{\text{undet}}$ is added to the model. The measurements of off-shell production described in Section 3.9 is included in the combination, for these results only, and used to provide a constraint on B_{BSM} under the assumptions listed in Section 7.1.

The numerical results of the various scenarios are summarized in Table 11 and illustrated in Figure 16. Limits on B_{inv}, B_{undet} and B_{BSM} are set using the $\tilde{t}_\mu$ prescription presented in Section 4. All probed fundamental coupling-strength scale factors, as well as the probed loop-induced coupling scale factors are measured to be compatible with their SM expectation under all explored assumptions. Upper limits are set on the fraction of Higgs boson decays to invisible or undetected decays. In scenario (b) the observed (expected) 95% CL upper limits on the branching ratios are $B_{\text{inv}} < 0.30$ (0.18) and $B_{\text{undet}} < 0.22$ (0.38), and the lower limits on the couplings to vector bosons are $\kappa_Z > 0.87$ (0.76) and $\kappa_W > 0.86$ (0.77). In scenario (c), the observed (expected) upper limit on B_{BSM} is 0.47 (0.57). The compatibility of the SM hypothesis with the best-fit point in scenario (a) is $p_{\text{SM}} = 88\%$, computed using the procedure outlined in Section 4 with seven degrees of freedom and B_{BSM} fixed to zero.

Table 11: Fit results for Higgs boson coupling modifiers per particle type with effective photon and gluon couplings and either (a) $B_{\text{inv}} = B_{\text{undet}} = 0$, (b) B_{inv} and B_{undet} included as free parameters, the conditions $\kappa_{W,Z} \leq 1$ applied and the measurement of the Higgs boson decay rate to invisible final states described in Section 3.8 included in the combination, or (c) $B_{\text{BSM}} = B_{\text{inv}} + B_{\text{undet}}$ included as a free parameter, the measurement of off-shell Higgs boson production described in Section 3.9 included in the combination, and the assumptions described in the text applied on the off-shell coupling-strength scale factors. The SM corresponds to $B_{\text{inv}} = B_{\text{undet}} = B_{\text{BSM}} = 0$ and all κ parameters set to unity. All parameters except κ_t are assumed to be positive.

Parameter	(a) $B_{\text{inv}} = B_{\text{undet}} = 0$	(b) B_{inv} free, $B_{\text{undet}} \geq 0$, $\kappa_{W,Z} \leq 1$	(c) $B_{\text{BSM}} \geq 0$, $\kappa_{\text{off}} = \kappa_{\text{on}}$
κ_Z	1.11 ± 0.08	> 0.87 at 95% CL	$1.16^{+0.18}_{-0.13}$
κ_W	1.05 ± 0.09	> 0.85 at 95% CL	$1.12^{+0.18}_{-0.15}$
κ_b	$1.03^{+0.19}_{-0.17}$	0.88 ± 0.13	$1.08^{+0.25}_{-0.20}$
κ_t	$1.09^{+0.15}_{-0.14}$	$[-1.03, -0.79] \cup [0.93, 1.24]$ at 68% CL	$1.14^{+0.19}_{-0.18}$
κ_τ	$1.05^{+0.16}_{-0.15}$	0.97 ± 0.13	$1.12^{+0.23}_{-0.21}$
κ_γ	1.05 ± 0.09	0.98 ± 0.07	$1.10^{+0.19}_{-0.13}$
κ_g	$0.99^{+0.11}_{-0.10}$	$1.01^{+0.13}_{-0.11}$	$1.02^{+0.22}_{-0.13}$
B_{inv}	-	< 0.30 at 95% CL	-
B_{undet}	-	< 0.22 at 95% CL	-
B_{BSM}	-	-	< 0.47 at 95% CL

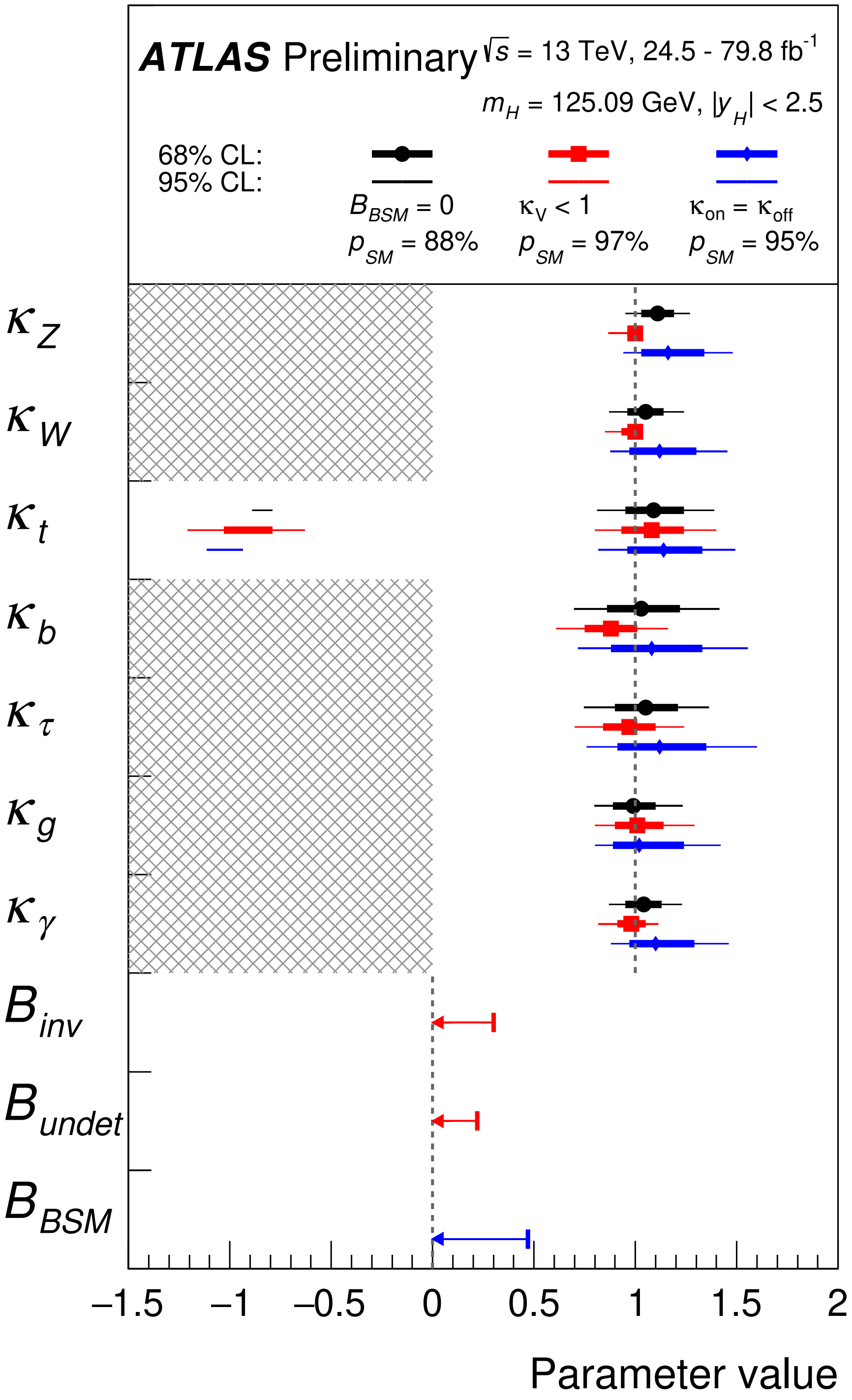

Figure 16: Best-fit values and uncertainties of Higgs boson coupling modifiers per particle type with effective photon and gluon couplings and either $\mathrm{B}_{\mathrm{inv}} = \mathrm{B}_{\mathrm{undet}} = 0$ (black); $\mathrm{B}_{\mathrm{inv}}$ and $\mathrm{B}_{\mathrm{undet}}$ included as free parameters, the conditions $\kappa_{W,Z} \leq 1$ applied and the measurement of the Higgs boson decay rate to invisible final states described in Section 3.8 included in the combination (red); or $\mathrm{B}_{\mathrm{BSM}} = \mathrm{B}_{\mathrm{inv}} + \mathrm{B}_{\mathrm{undet}}$ included as a free parameter, the measurement of off-shell Higgs boson production described in Section 3.9 included in the combination, and the assumptions described in the text applied on the off-shell coupling-strength scale factors (blue). The SM corresponds to $\mathrm{B}_{\mathrm{inv}} = \mathrm{B}_{\mathrm{undet}} = \mathrm{B}_{\mathrm{BSM}} = 0$ and all κ parameters set to unity. All parameters except κ_t are assumed to be positive.

7.6 Generic parameterization using ratios of coupling modifiers

The five absolute coupling strength scale factors and two effective loop coupling scale factors measured in the previous benchmark model are expressed as ratios of scale factors that can be measured independent of any assumptions on the Higgs boson total width. The model parameters are defined in Table 12. All parameters are assumed to be positive. This parametrization represents the most model-independent determination of coupling-strength scale factors that is currently possible in the κ-framework. The numerical results from the fit to this benchmark model are summarized in Table 12 and visualized in Figure 17. All model parameters are measured to be compatible with their SM expectation. The compatibility of the SM hypothesis with the best fit point corresponds to a p-value of $p_{\mathrm{SM}} = 85\%$, computed using the procedure outlined in Section 4 with seven degrees of freedom.

The parameter λ_{WZ} in this model is of particular interest: identical coupling-strength scale factors for the W and Z bosons are required within tight bounds by the SU(2) custodial symmetry and the ρ parameter measurements at LEP and at the Tevatron [109]. The ratio $\lambda_{\gamma Z}$ is sensitive to new charged particles contributing to the $H \rightarrow \gamma\gamma$ loop in comparison to $H \rightarrow ZZ^*$ decays. Similarly, the ratio λ_{tg} is sensitive to new colored particles contributing through the ggF loop as compared to ttH. The observed values are in agreement with the SM expectation.

Table 12: Best-fit values and uncertainties of ratios of coupling modifiers. The second column provides the expression of the measured parameters in terms of the coupling modifiers defined in previous sections. All parameters are defined to be unity in the SM.

Parameter	Definition in terms of κ modifiers	Result
κ_{gZ}	$\kappa_g \kappa_Z / \kappa_H$	1.06 ± 0.07
λ_{tg}	κ_t / κ_g	$1.10^{+0.15}_{-0.14}$
λ_{Zg}	κ_Z / κ_g	$1.12^{+0.15}_{-0.13}$
λ_{WZ}	κ_W / κ_Z	0.95 ± 0.08
$\lambda_{\gamma Z}$	κ_γ / κ_Z	0.94 ± 0.07
$\lambda_{\tau Z}$	κ_τ / κ_Z	0.95 ± 0.13
λ_{bZ}	κ_b / κ_Z	$0.93^{+0.15}_{-0.13}$

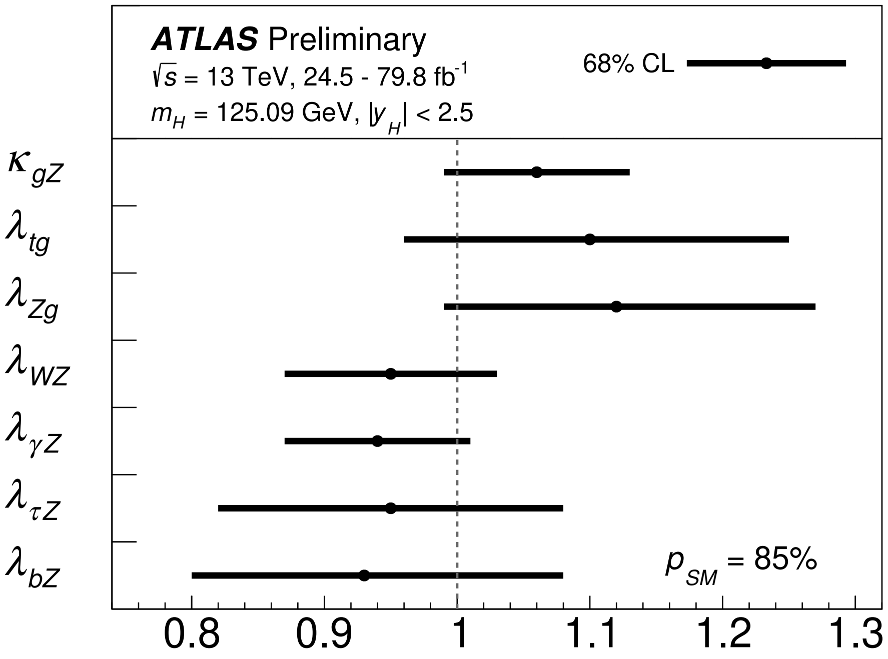

Figure 17: Measured ratios of coupling modifiers. The dashed line indicates the SM value of unity for each parameter.

8 Constraints on New Phenomena

Two Higgs doublet models (2HDMs) [28, 110–112] and supersymmetry [113–118] are promising extensions of the SM. The measurements are interpreted in these benchmark models, providing indirect limits on their parameters that are complementary to those obtained by direct searches for new particles. The interpretations presented in this section follow the procedure discussed in Ref. [29].

8.1 Two Higgs doublet model

In 2HDMs, the SM Higgs sector is extended by introducing an additional complex isodoublet scalar field with weak hypercharge one. Four types of 2HDMs satisfy the Paschos-Glashow-Weinberg condition [119, 120], which prevents the appearance of tree-level flavor-changing neutral currents:

- Type I: One Higgs doublet couples to vector bosons, while the other one couples to fermions. The first doublet is *fermiophobic* in the limit where the two Higgs doublets do not mix.
- Type II: One Higgs doublet couples to up-type quarks and the other one to down-type quarks and charged leptons.
- Lepton-specific: The Higgs bosons have the same couplings to quarks as in the Type I model and to charged leptons as in Type II.
- Flipped: The Higgs bosons have the same couplings to quarks as in the Type II model and to charged leptons as in Type I.

The observed Higgs boson is identified with the light CP-even neutral scalar h predicted by 2HDMs, and its accessible production and decay modes are assumed to be the same as those of the SM Higgs boson. Its couplings to vector bosons, up-type quarks, down-type quarks and leptons relative to the corresponding SM predictions are expressed as functions of the mixing angle of h with the heavy CP-even neutral scalar, α, and the ratio of the vacuum expectation values of the Higgs doublets, $\tan\beta$.

Figure 18 shows the regions of the $(\cos(\beta-\alpha), \tan\beta)$ plane that are excluded at a confidence level of 95 % or higher, for each of the four types of 2HDMs. The expected exclusion limits in the SM hypothesis are also overlaid. The data are consistent with the alignment limit [112] at $\cos(\beta-\alpha) = 0$, in which the couplings of h match those of the SM Higgs boson, within one standard deviation or better in each of the tested models. The allowed regions also include narrow, curved *petal* regions at positive $\cos(\beta-\alpha)$ and moderate $\tan\beta$ in the Type II, Lepton-specific, and Flipped models. These correspond to regions with $\cos(\beta+\alpha) \approx 0$, for which some fermion couplings have the same magnitude as in the SM, but the opposite sign.

8.2 Simplified Minimal Supersymmetric Standard Model

The scalar sector of the Minimal Supersymmetric Standard Model (MSSM) [121–123] is a realization of a Type II 2HDM. As a benchmark, a simplified MSSM model in which the Higgs boson is identified with the light CP-even scalar h, termed hMSSM [124–126], is studied. The assumptions made by this model are discussed in Ref. [29]. Notably, the hMSSM is a good approximation of the MSSM only for moderate values of $\tan\beta$. For $\tan\beta \gtrsim 10$ the scenario is approximate due to missing supersymmetry corrections in the Higgs boson coupling to b-quarks, and for $\tan\beta$ of $O(1)$ the precision of the approximation depends on m_A [26]. The production and decay modes accessible to h are assumed to be the same as those of the SM Higgs boson.

The Higgs boson couplings to vector bosons, up-type fermions and down-type fermions relative to the corresponding SM predictions are expressed as functions of the ratio of the vacuum expectation values of the Higgs doublets, $\tan\beta$, and the masses of the CP-odd scalar (m_A), the Z boson, and of h.

Figure 19 shows the regions of the hMSSM parameter space that are indirectly excluded by the measurement of the Higgs boson production and decay rates. The data are consistent with the SM decoupling limit at large m_A, where the h couplings tend to those of the SM Higgs boson. The observed (expected) lower limit at 95 % CL on the CP-odd Higgs boson mass is at least $m_A > 480$ GeV ($m_A > 400$ GeV) for $1 \leq \tan\beta \leq 25$, increasing to $m_A > 530$ GeV ($m_A > 450$ GeV) at $\tan\beta = 1$. The observed limit is stronger than the expected because the hMSSM model exhibits a physical boundary $\kappa_V \leq 1$, but the Higgs boson coupling to vector bosons is measured to be larger than the SM value, as presented in Section 7.

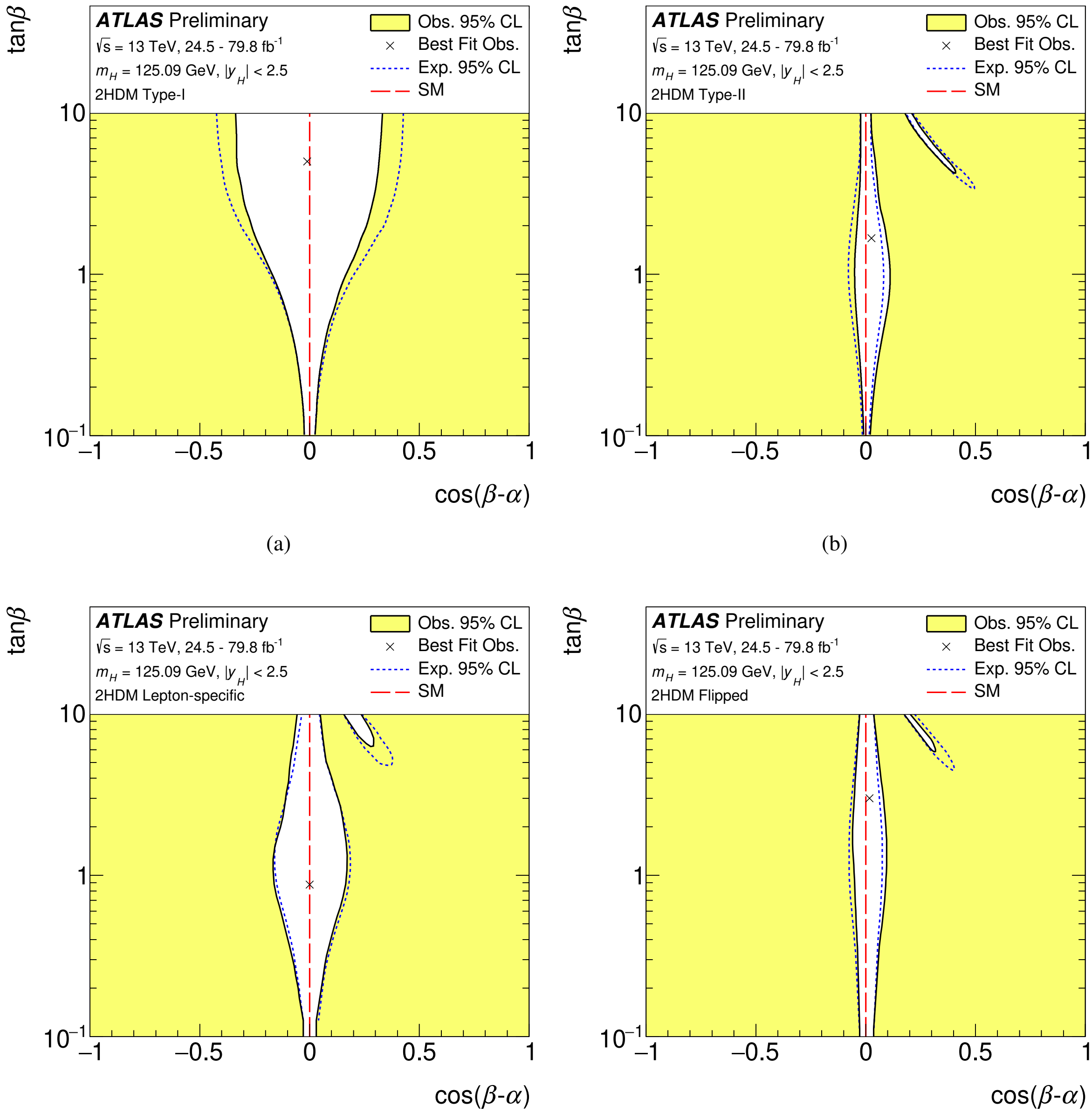

(a) (b)

(c) (d)

Figure 18: Regions of the $(\cos(\beta - \alpha), \tan\beta)$ plane of four types of 2HDMs excluded by fits to the measured rates of Higgs boson production and decays. Contours at 95% CL, defined in the asymptotic approximation by $-2\ln\Lambda = 5.99$, are drawn for both the data and the expectation for the SM Higgs sector. The cross in each plot marks the observed best-fit value. The angles α and β are taken to satisfy $0 \le \beta \le \pi/2$ and $0 \le \beta - \alpha \le \pi$ without loss of generality. The alignment limit at $\cos(\beta - \alpha) = 0$, in which all Higgs boson couplings take their SM values, is indicated by the dashed red line.

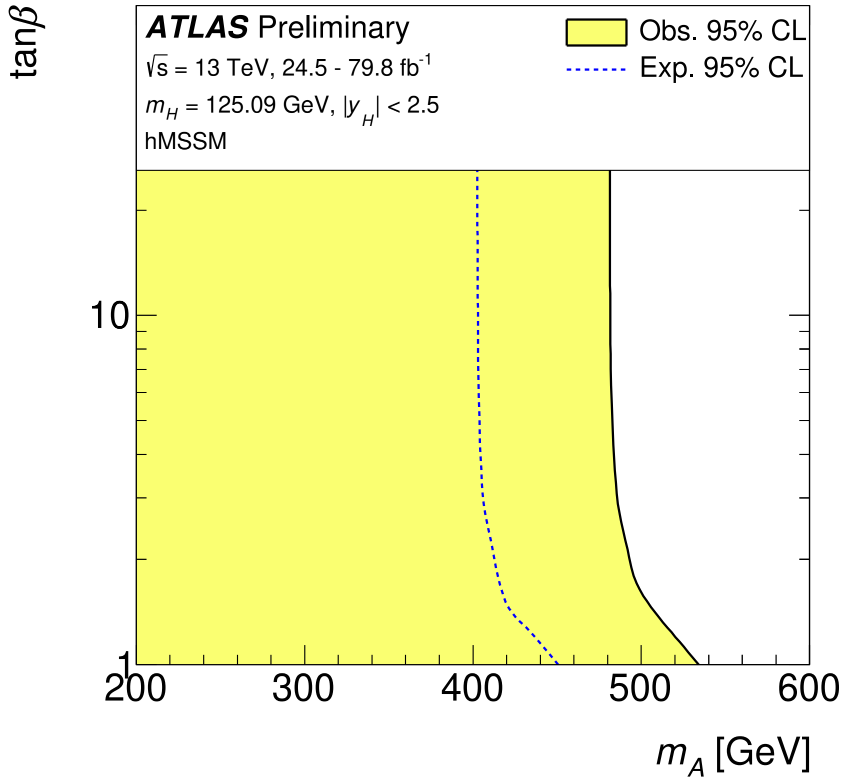

Figure 19: Regions of the $(m_A, \tan\beta)$ plane in the hMSSM excluded by fits to the measured rates of Higgs boson production and decays. Likelihood contours at 95% CL, defined in the asymptotic approximation by $-2\ln\Lambda = 5.99$, are drawn for both the data and the expectation of the SM Higgs sector. The regions to the left of the solid contour are excluded. The decoupling limit, in which all Higgs boson couplings tend to their SM value, corresponds to $m_A \to \infty$.

9 Conclusions

Measurements of Higgs boson production cross sections and branching ratios have been performed using up to 79.8 fb^{-1} of proton-proton collision data produced by the LHC at $\sqrt{s} = 13$ TeV and recorded by the ATLAS detector. The results presented in this note are based on the combination of analyses of the $H \to \gamma\gamma$, $H \to ZZ^*$, $H \to WW^*$, $H \to \tau\tau$, $H \to b\bar{b}$ and $H \to \mu\mu$ decay modes, searches for decays into invisible final states, as well as on measurements of off-shell Higgs boson production.

The global signal strength is determined to be $\mu = 1.11^{+0.09}_{-0.08}$.

The Higgs boson production cross sections within the region $|y_H| < 2.5$ are measured in a combined fit for the gluon fusion process, vector-boson fusion, the associated production with a W or Z boson and the associated production with top quarks, assuming the SM Higgs boson branching fractions. The combined measurement leads to an observed (expected) significance for the vector-boson fusion production process of 6.5σ (5.3σ). For the VH production mode the observed (expected) significance is 5.3σ (4.7σ). The $t\bar{t}H + tH$ processes are measured with an observed (expected) significance of 5.8σ (5.3σ).

Removing the SM assumption on branching fractions, a combined fit is performed for the production cross section times branching fraction for each pair of production and decay processes the combined analyses are sensitive to. Results are also presented for a model in which these quantities are expressed using the cross section of the $gg \to H \to ZZ^*$ process, ratios of production cross sections relative to that of ggF production, and ratios of branching fraction relative to that of $H \to ZZ^*$.

Cross sections are measured in 17 regions of Higgs boson production kinematics defined within the simplified template cross section framework, which characterize in particular the transverse momentum of the Higgs boson, the topology of associated jets and the transverse momentum of associated vector bosons. The measurements in all regions are found to be compatible with SM predictions.

The observed Higgs boson yields are used to obtain confidence intervals for κ modifiers to the couplings of the SM Higgs boson to fermions, weak vector bosons, gluons, and photons and to the branching ratio of the Higgs boson to invisible and undetected decay modes. A variety of physics-motivated constraints on the Higgs boson total width are explored: Using searches for $H \to$ invisible and constraints on couplings to vector bosons, the branching fraction of invisible Higgs boson decays into BSM particles is constrained to be less than 30% at 95% CL, while the branching fraction of decays into undetected particles is less than 22% at 95% CL. The overall branching fraction of the Higgs boson into BSM decays is determined to be less than 47% at 95% CL using measurements of off-shell Higgs boson production in combination with measurements of SM Higgs boson production and rates. No significant deviation from the Standard Model predictions is observed in any of the benchmark models studied.

Finally, the results are interpreted in the context of two-Higgs doublet models and the hMSSM. Constraints are set in the $(m_A, \tan\beta)$ plane of the hMSSM and the $(\cos(\beta - \alpha), \tan\beta)$ plane in 2HDM Type-I, Type-II, Lepton-specific and Flipped models.

References

[1] ATLAS Collaboration, *Observation of a new particle in the search for the Standard Model Higgs boson with the ATLAS detector at the LHC*, Phys. Lett. B **716** (2012) 1, arXiv: `1207.7214 [hep-ex]` (cit. on p. 2).

[2] CMS Collaboration, *Observation of a new boson at a mass of 125 GeV with the CMS experiment at the LHC*, Phys. Lett. B **716** (2012) 30, arXiv: `1207.7235 [hep-ex]` (cit. on p. 2).

[3] ATLAS and CMS Collaborations, *Measurements of the Higgs boson production and decay rates and constraints on its couplings from a combined ATLAS and CMS analysis of the LHC pp collision data at* $\sqrt{s} = 7$ *and* 8 *TeV*, JHEP **08** (2016) 045, arXiv: `1606.02266 [hep-ex]` (cit. on pp. 2, 13, 15, 19, 25, 36, 61).

[4] ATLAS Collaboration, *Measurements of Higgs boson properties in the diphoton decay channel with* $36 fb^{-1}$ *of pp collision data at* $\sqrt{s} = 13$ *TeV with the ATLAS detector*, Phys. Rev. D **98** (2018) 052005, arXiv: `1802.04146 [hep-ex]` (cit. on pp. 2, 7, 27).

[5] ATLAS Collaboration, *Measurement of the Higgs boson coupling properties in the* $H \to ZZ^* \to 4\ell$ *decay channel at* $\sqrt{s} = 13$ *TeV with the ATLAS detector*, JHEP **03** (2018) 095, arXiv: `1712.02304 [hep-ex]` (cit. on pp. 2, 7).

[6] ATLAS Collaboration, *Observation of Higgs boson production in association with a top quark pair at the LHC with the ATLAS detector*, Phys. Lett. B **784** (2018) 173, arXiv: `1806.00425 [hep-ex]` (cit. on pp. 2, 7, 8, 10, 16).

[7] ATLAS Collaboration, *Measurements of gluon-gluon fusion and vector-boson fusion Higgs boson production cross-sections in the* $H \to WW^* \to e\nu\mu\nu$ *decay channel in pp collisions at* $\sqrt{s} = 13$ *TeV with the ATLAS detector*, Phys. Lett. B **789** (2019) 508, arXiv: `1808.09054 [hep-ex]` (cit. on pp. 2, 8).

[8] ATLAS Collaboration, *Cross-section measurements of the Higgs boson decaying into a pair of* τ*-leptons in proton–proton collisions at* $\sqrt{s} = 13$ *TeV with the ATLAS detector*, Phys. Rev. (2018), arXiv: `1811.08856 [hep-ex]` (cit. on pp. 2, 8).

[9] ATLAS Collaboration, *Observation of* $H \to b\bar{b}$ *decays and* VH *production with the ATLAS detector*, Phys. Lett. B **786** (2018) 59, arXiv: `1808.08238 [hep-ex]` (cit. on pp. 2, 9).

[10] ATLAS Collaboration, *Measurements of* VH, $H \to b\bar{b}$ *production as a function of the vector boson transverse momentum in* 13 *TeV pp collisions with the ATLAS detector*, (2019), arXiv: `1903.04618 [hep-ex]` (cit. on pp. 2, 9).

[11] ATLAS Collaboration, *Search for Higgs bosons produced via vector-boson fusion and decaying into bottom quark pairs in* $\sqrt{s} = 13$ *TeV pp collisions with the ATLAS detector*, Phys. Rev. D **98** (2018) 052003, arXiv: `1807.08639 [hep-ex]` (cit. on pp. 2, 9).

[12] ATLAS Collaboration, *Evidence for the associated production of the Higgs boson and a top quark pair with the ATLAS detector*, Phys. Rev. D **97** (2018) 072003, arXiv: `1712.08891 [hep-ex]` (cit. on pp. 2, 10).

[13] ATLAS Collaboration, *Search for the standard model Higgs boson produced in association with top quarks and decaying into a* $b\bar{b}$ *pair in pp collisions at* $\sqrt{s} = 13$ *TeV with the ATLAS detector*, Phys. Rev. D **97** (2018) 072016, arXiv: `1712.08895 [hep-ex]` (cit. on pp. 2, 10).

[14] ATLAS Collaboration, *Search for the Dimuon Decay of the Higgs Boson in pp Collisions at* $\sqrt{s} = 13$ *TeV with the ATLAS Detector*, Phys. Rev. Lett. **119** (2017) 051802, arXiv: `1705.04582 [hep-ex]` (cit. on pp. 2, 10).

[15] ATLAS Collaboration, *Search for invisible Higgs boson decays in vector boson fusion at* $\sqrt{s} =$ 13 *TeV with the ATLAS detector*, Phys. Lett. (2018), arXiv: `1809.06682 [hep-ex]` (cit. on pp. 2, 11).

[16] ATLAS Collaboration, *Search for an invisibly decaying Higgs boson or dark matter candidates produced in association with a Z boson in pp collisions at* $\sqrt{s} = 13$ *TeV with the ATLAS detector*, Phys. Lett. B **776** (2018) 318, arXiv: `1708.09624 [hep-ex]` (cit. on pp. 2, 11).

[17] ATLAS Collaboration, *Search for dark matter in events with a hadronically decaying vector boson and missing transverse momentum in pp collisions at* $\sqrt{s} = 13$ *TeV with the ATLAS detector*, JHEP **10** (2018) 180, arXiv: `1807.11471 [hep-ex]` (cit. on pp. 2, 11).

[18] ATLAS Collaboration, *Constraints on off-shell Higgs boson production and the Higgs boson total width in* $ZZ \to 4\ell$ *and* $ZZ \to 2\ell 2\nu$ *final states with the ATLAS detector*, Phys. Lett. B **786** (2018) 223, arXiv: `1808.01191 [hep-ex]` (cit. on pp. 2, 5, 12, 33).

[19] ATLAS and CMS Collaborations, *Combined Measurement of the Higgs Boson Mass in pp Collisions at* $\sqrt{s} = 7$ *and* 8 *TeV with the ATLAS and CMS Experiments*, Phys. Rev. Lett. **114** (2015) 191803, arXiv: `1503.07589 [hep-ex]` (cit. on p. 2).

[20] CMS Collaboration, *Measurements of Higgs boson properties in the diphoton decay channel in proton–proton collisions at* $\sqrt{s} = 13$ *TeV*, JHEP **11** (2018) 185, arXiv: `1804.02716 [hep-ex]` (cit. on p. 2).

[21] CMS Collaboration, *Measurements of properties of the Higgs boson decaying to a W boson pair in pp collisions at* $\sqrt{s} = 13$ *TeV*, Phys. Lett. (2018), arXiv: `1806.05246 [hep-ex]` (cit. on p. 2).

[22] CMS Collaboration, *Observation of the Higgs boson decay to a pair of* τ *leptons*, Phys. Lett. B **779** (2018) 283, arXiv: `1708.00373 [hep-ex]` (cit. on p. 2).

[23] CMS Collaboration, *Evidence for the Higgs boson decay to a bottom quark–antiquark pair*, Phys. Lett. B **780** (2018) 501, arXiv: `1709.07497 [hep-ex]` (cit. on p. 2).

[24] CMS Collaboration, *Observation of* $t\bar{t}H$ *Production*, Phys. Rev. Lett. **120** (2018) 231801, arXiv: `1804.02610 [hep-ex]` (cit. on p. 2).

[25] CMS Collaboration, *Combined measurements of Higgs boson couplings in proton–proton collisions at* $\sqrt{s} = 13$ *TeV*, Eur. Phys. J. (2018), arXiv: `1809.10733 [hep-ex]` (cit. on p. 2).

[26] LHC Higgs Cross Section Working Group, D. de Florian et al., *Handbook of LHC Higgs Cross Sections: 4. Deciphering the Nature of the Higgs Sector*, (2016), arXiv: `1610.07922 [hep-ph]` (cit. on pp. 2–4, 13, 16, 17, 21, 25, 26, 32, 45, 58, 64, 67).

[27] J. R. Andersen et al., *Les Houches 2015: Physics at TeV Colliders Standard Model Working Group Report*, (2016), arXiv: `1605.04692 [hep-ph]` (cit. on pp. 2, 25, 67).

[28] LHC Higgs Cross Section Working Group, S. Heinemeyer et al., *Handbook of LHC Higgs Cross Sections: 3. Higgs Properties*, CERN-2013-004 (2013), arXiv: `1307.1347 [hep-ph]` (cit. on pp. 3, 32, 33, 35, 44).

[29] ATLAS Collaboration, *Constraints on new phenomena via Higgs boson couplings and invisible decays with the ATLAS detector*, JHEP **11** (2015) 206, arXiv: `1509.00672 [hep-ex]` (cit. on pp. 3, 44, 45).

[30] ATLAS Collaboration, *The ATLAS Experiment at the CERN Large Hadron Collider*, JINST **3** (2008) S08003 (cit. on p. 3).

[31] ATLAS Collaboration, *ATLAS Insertable B-layer Technical Design Report*, CERN-LHCC-2010-013, ATLAS-TDR-19 (2010), URL: `http://cds.cern.ch/record/1291633` (cit. on p. 3).

[32] P. Nason, *A new method for combining NLO QCD with shower Monte Carlo algorithms*, JHEP **0411** (2004) 040, arXiv: `hep-ph/0409146` (cit. on p. 4).

[33] S. Frixione, P. Nason, and C. Oleari, *Matching NLO QCD computations with Parton Shower simulations: the POWHEG method*, JHEP **0711** (2007) 070, arXiv: `0709.2092 [hep-ph]` (cit. on p. 4).

[34] S. Alioli, P. Nason, C. Oleari, and E. Re, *A general framework for implementing NLO calculations in shower Monte Carlo programs: the POWHEG BOX*, JHEP **1006** (2010) 043, arXiv: `1002.2581 [hep-ph]` (cit. on p. 4).

[35] S. Alioli, P. Nason, C. Oleari, and E. Re, *NLO Higgs boson production via gluon fusion matched with shower in POWHEG*, JHEP **0904** (2009) 002, arXiv: `0812.0578 [hep-ph]` (cit. on p. 4).

[36] K. Hamilton, P. Nason, E. Re, and G. Zanderighi, *NNLOPS simulation of Higgs boson production*, JHEP **1310** (2013) 222, arXiv: `1309.0017 [hep-ph]` (cit. on p. 4).

[37] K. Hamilton, P. Nason, and G. Zanderighi, *Finite quark-mass effects in the NNLOPS POWHEG+MiNLO Higgs generator*, JHEP **1505** (2015) 140, arXiv: `1501.04637 [hep-ph]` (cit. on p. 4).

[38] S. Catani and M. Grazzini, *An NNLO subtraction formalism in hadron collisions and its application to Higgs boson production at the LHC*, Phys. Rev. Lett. **98** (2007) 222002, arXiv: `hep-ph/0703012` (cit. on p. 4).

[39] K. Hamilton, P. Nason, C. Oleari, and G. Zanderighi, *Merging H/W/Z + 0 and 1 jet at NLO with no merging scale: a path to parton shower + NNLO matching*, JHEP **1305** (2013) 082, arXiv: `1212.4504 [hep-ph]` (cit. on p. 4).

[40] J. Butterworth et al., *PDF4LHC recommendations for LHC Run II*, J. Phys. G **43** (2016) 023001, arXiv: `1510.03865 [hep-ph]` (cit. on p. 4).

[41] C. Anastasiou, C. Duhr, F. Dulat, F. Herzog, and B. Mistlberger, *Higgs Boson Gluon-Fusion Production in QCD at Three Loops*, Phys. Rev. Lett. **114** (2015) 212001, arXiv: `1503.06056 [hep-ph]` (cit. on p. 4).

[42] C. Anastasiou et al., *High precision determination of the gluon fusion Higgs boson cross-section at the LHC*, JHEP **1605** (2016) 058, arXiv: `1602.00695 [hep-ph]` (cit. on p. 4).

[43] S. Actis, G. Passarino, C. Sturm, and S. Uccirati, *NLO electroweak corrections to Higgs boson production at hadron colliders*, Phys. Lett. B **670** (2008) 12, arXiv: `0809.1301 [hep-ph]` (cit. on p. 4).

[44] C. Anastasiou, R. Boughezal, and F. Petriello, *Mixed QCD-electroweak corrections to Higgs boson production in gluon fusion*, JHEP **0904** (2009) 003, arXiv: `0811.3458 [hep-ph]` (cit. on p. 4).

[45] M. Grazzini and H. Sargsyan, *Heavy-quark mass effects in Higgs boson production at the LHC*, JHEP **1309** (2013) 129, arXiv: `1306.4581 [hep-ph]` (cit. on p. 4).

[46] P. Nason and C. Oleari, *NLO Higgs boson production via vector-boson fusion matched with shower in POWHEG*, JHEP **1002** (2010) 037, arXiv: `0911.5299 [hep-ph]` (cit. on p. 4).

[47] M. Ciccolini, A. Denner, and S. Dittmaier, *Strong and electroweak corrections to the production of Higgs + 2-jets via weak interactions at the LHC*, Phys. Rev. Lett. **99** (2007) 161803, arXiv: `0707.0381 [hep-ph]` (cit. on p. 4).

[48] M. Ciccolini, A. Denner, and S. Dittmaier, *Electroweak and QCD corrections to Higgs production via vector-boson fusion at the LHC*, Phys. Rev. D **77** (2008) 013002, arXiv: `0710.4749 [hep-ph]` (cit. on p. 4).

[49] P. Bolzoni, F. Maltoni, S.-O. Moch, and M. Zaro, *Higgs production via vector-boson fusion at NNLO in QCD*, Phys. Rev. Lett. **105** (2010) 011801, arXiv: `1003.4451 [hep-ph]` (cit. on p. 4).

[50] G. Cullen et al., *Automated One-Loop Calculations with GoSam*, Eur. Phys. J. **C72** (2012) 1889, arXiv: `1111.2034 [hep-ph]` (cit. on p. 4).

[51] K. Hamilton, P. Nason, and G. Zanderighi, *MINLO: Multi-Scale Improved NLO*, JHEP **10** (2012) 155, arXiv: `1206.3572 [hep-ph]` (cit. on p. 4).

[52] G. Luisoni, P. Nason, C. Oleari, and F. Tramontano, *$HW^{\pm}/HZ + 0$ and 1 jet at NLO with the POWHEG BOX interfaced to GoSam and their merging within MiNLO*, JHEP **10** (2013) 083, arXiv: `1306.2542 [hep-ph]` (cit. on p. 4).

[53] O. Brein, A. Djouadi, and R. Harlander, *NNLO QCD corrections to the Higgs-strahlung processes at hadron colliders*, Phys. Lett. B **579** (2004) 149, arXiv: `hep-ph/0307206 [hep-ph]` (cit. on p. 4).

[54] A. Denner, S. Dittmaier, S. Kallweit, and A. Muck, *Electroweak corrections to Higgs-strahlung off W/Z bosons at the Tevatron and the LHC with HAWK*, JHEP **1203** (2012) 075, arXiv: `1112.5142 [hep-ph]` (cit. on p. 4).

[55] L. Altenkamp, S. Dittmaier, R. V. Harlander, H. Rzehak, and T. J. E. Zirke, *Gluon-induced Higgs-strahlung at next-to-leading order QCD*, JHEP **1302** (2013) 078, arXiv: `1211.5015 [hep-ph]` (cit. on p. 4).

[56] J. Alwall, R. Frederix, S. Frixione, V. Hirschi, F. Maltoni, et al., *The automated computation of tree-level and next-to-leading order differential cross sections, and their matching to parton shower simulations*, JHEP **1407** (2014) 079, arXiv: `1405.0301 [hep-ph]` (cit. on p. 4).

[57] R. D. Ball et al., *Parton distributions for the LHC Run II*, JHEP **04** (2015) 040, arXiv: `1410.8849 [hep-ph]` (cit. on p. 4).

[58] W. Beenakker, S. Dittmaier, M. Krämer, B. Plumper, M. Spira, et al., *NLO QCD corrections to $t\bar{t}H$ production in hadron collisions*, Nucl. Phys. B **653** (2003) 151, arXiv: `hep-ph/0211352 [hep-ph]` (cit. on p. 4).

[59] S. Dawson, C. Jackson, L. Orr, L. Reina, and D. Wackeroth, *Associated Higgs production with top quarks at the large hadron collider: NLO QCD corrections*, Phys. Rev. D **68** (2003) 034022, arXiv: `hep-ph/0305087 [hep-ph]` (cit. on p. 4).

[60] Y. Zhang, W.-G. Ma, R.-Y. Zhang, C. Chen, and L. Guo, *QCD NLO and EW NLO corrections to $t\bar{t}H$ production with top quark decays at hadron collider*, Phys. Lett. B **738** (2014) 1, arXiv: `1407.1110 [hep-ph]` (cit. on p. 4).

[61] S. Frixione, V. Hirschi, D. Pagani, H. S. Shao, and M. Zaro, *Weak corrections to Higgs hadroproduction in association with a top-quark pair*, JHEP **1409** (2014) 065, arXiv: `1407.0823 [hep-ph]` (cit. on p. 4).

[62] M. Wiesemann et al., *Higgs production in association with bottom quarks*, JHEP **02** (2015) 132, arXiv: `1409.5301 [hep-ph]` (cit. on p. 4).

[63] S. Dawson, C. Jackson, L. Reina, and D. Wackeroth, *Exclusive Higgs boson production with bottom quarks at hadron colliders*, Phys. Rev. D **69** (2004) 074027, arXiv: `hep-ph/0311067 [hep-ph]` (cit. on p. 4).

[64] S. Dittmaier, M. Krämer, and M. Spira, *Higgs radiation off bottom quarks at the Tevatron and the CERN LHC*, Phys. Rev. D **70** (2004) 074010, arXiv: `hep-ph/0309204 [hep-ph]` (cit. on p. 4).

[65] R. V. Harlander and W. B. Kilgore, *Higgs boson production in bottom quark fusion at next-to-next-to leading order*, Phys. Rev. D **68** (2003) 013001, arXiv: `hep-ph/0304035 [hep-ph]` (cit. on p. 4).

[66] J. Pumplin et al., *New generation of parton distributions with uncertainties from global QCD analysis*, JHEP **07** (2002) 012, arXiv: `hep-ph/0201195 [hep-ph]` (cit. on p. 4).

[67] H.-L. Lai, M. Guzzi, J. Huston, Z. Li, P. M. Nadolsky, et al., *New parton distributions for collider physics*, Phys. Rev. D **82** (2010) 074024, arXiv: `1007.2241 [hep-ph]` (cit. on p. 4).

[68] F. Demartin, F. Maltoni, K. Mawatari, and M. Zaro, *Higgs production in association with a single top quark at the LHC*, Eur. Phys. J. C **75** (2015) 267, arXiv: `1504.00611 [hep-ph]` (cit. on p. 4).

[69] T. Sjöstrand, S. Mrenna, and P. Z. Skands, *A Brief Introduction to PYTHIA 8.1*, Comput. Phys. Commun. **178** (2008) 852, arXiv: `0710.3820 [hep-ph]` (cit. on p. 4).

[70] S. Gieseke, A. Ribon, M. H. Seymour, P. Stephens, and B. Webber, *Herwig++ 1.0: An Event generator for e+ e- annihilation*, JHEP **0402** (2004) 005, arXiv: `hep-ph/0311208` (cit. on p. 4).

[71] The ATLAS Collaboration, *Measurement of the* Z/γ^* *boson transverse momentum distribution in pp collisions at* $\sqrt{s} = 7$ *TeV with the ATLAS detector*, JHEP **09** (2014) 145, arXiv: `1406.3660 [hep-ex]` (cit. on p. 4).

[72] E. Bagnaschi, G. Degrassi, P. Slavich, and A. Vicini, *Higgs production via gluon fusion in the POWHEG approach in the SM and in the MSSM*, JHEP **1202** (2012) 088, arXiv: `1111.2854 [hep-ph]` (cit. on p. 4).

[73] F. Cascioli et al., *Precise Higgs-background predictions: merging NLO QCD and squared quark-loop corrections to four-lepton + 0,1 jet production*, JHEP **01** (2014) 046, arXiv: `1309.0500 [hep-ph]` (cit. on p. 5).

[74] T. Gleisberg et al., *Event generation with SHERPA 1.1*, JHEP **02** (2009) 007, arXiv: `0811.4622 [hep-ph]` (cit. on p. 5).

[75] F. Cascioli, P. Maierhofer, and S. Pozzorini, *Scattering Amplitudes with Open Loops*, Phys. Rev. Lett. **108** (2012) 111601, arXiv: `1111.5206 [hep-ph]` (cit. on p. 5).

[76] A. Denner, S. Dittmaier, and L. Hofer, *COLLIER - A fortran-library for one-loop integrals*, PoS **LL2014** (2014) 071, arXiv: `1407.0087 [hep-ph]` (cit. on p. 5).

[77] S. Schumann and F. Krauss, *A Parton shower algorithm based on Catani-Seymour dipole factorisation*, JHEP **03** (2008) 038, arXiv: `0709.1027 [hep-ph]` (cit. on p. 5).

[78] S. Agostinelli et al. (GEANT4 Collaboration), *GEANT4: a simulation toolkit*, Nucl. Instrum. Methods **506** (2003) 250 (cit. on p. 5).

[79] J. Allison et al. (GEANT4 Collaboration), *GEANT4 Developments and Applications*, IEEE Trans. Nucl. Sci. **53** (2006) 270 (cit. on p. 5).

[80] ATLAS Collaboration, *The ATLAS Simulation Infrastructure*, Eur. Phys. J. C **70** (2010) 823, arXiv: `1005.4568 [physics.ins-det]` (cit. on p. 5).

[81] A. Martin, W. Stirling, R. Thorne, and G. Watt, *Parton distributions for the LHC*, Eur. Phys. J. **C63** (2009) 189, arXiv: `0901.0002 [hep-ph]` (cit. on p. 5).

[82] ATLAS Collaboration, *Summary of ATLAS Pythia 8 tunes*, ATL-PHYS-PUB-2012-003, 2012, URL: `https://cds.cern.ch/record/1474107` (cit. on p. 5).

[83] ATLAS Collaboration, *Measurement of the photon identification efficiencies with the ATLAS detector using LHC Run 2 data collected in 2015 and 2016*, Eur. Phys. J. (2018), arXiv: `1810.05087 [hep-ex]` (cit. on p. 7).

[84] ATLAS Collaboration, *Topological cell clustering in the ATLAS calorimeters and its performance in LHC Run 1*, Eur. Phys. J. C **77** (2017) 490, arXiv: `1603.02934 [hep-ex]` (cit. on p. 7).

[85] ATLAS Collaboration, *Electron and photon reconstruction and performance in ATLAS using a dynamical, topological cell clustering-based approach*, ATL-PHYS-PUB-2017-022, 2017, URL: `https://cds.cern.ch/record/2298955` (cit. on p. 7).

[86] W. Lampl et al., *Calorimeter Clustering Algorithms: Description and Performance*, ATL-LARG-PUB-2008-002, 2008, URL: `https://cds.cern.ch/record/1099735` (cit. on p. 7).

[87] ATLAS Collaboration, *Electron efficiency measurements with the ATLAS detector using the 2015 LHC proton–proton collision data*, ATLAS-CONF-2016-024, 2016, URL: `https://cds.cern.ch/record/2157687` (cit. on p. 7).

[88] ATLAS Collaboration, *Muon reconstruction performance of the ATLAS detector in proton–proton collision data at* $\sqrt{s} = 13\,TeV$, Eur. Phys. J. C **76** (2016) 292, arXiv: `1603.05598 [hep-ex]` (cit. on p. 7).

[89] ATLAS Collaboration, *Jet energy scale measurements and their systematic uncertainties in proton–proton collisions at* $\sqrt{s} = 13\,TeV$ *with the ATLAS detector*, Phys. Rev. D **96** (2017) 072002, arXiv: `1703.09665 [hep-ex]` (cit. on p. 7).

[90] ATLAS Collaboration, *Measurements of b-jet tagging efficiency with the ATLAS detector using* $t\bar{t}$ *events at* $\sqrt{s} = 13\,TeV$, JHEP **08** (2018) 089, arXiv: `1805.01845 [hep-ex]` (cit. on p. 7).

[91] ATLAS Collaboration, *Performance of missing transverse momentum reconstruction with the ATLAS detector using proton–proton collisions at* $\sqrt{s} = 13\,TeV$, Eur. Phys. J. C **78** (2018) 903, arXiv: `1802.08168 [hep-ex]` (cit. on p. 7).

[92] ATLAS Collaboration, *Electron reconstruction and identification in the ATLAS experiment using the 2015 and 2016 LHC proton-proton collision data at* $\sqrt{s} = 13$ *TeV*, (2019), arXiv: `1902.04655 [physics.ins-det]` (cit. on p. 7).

[93] M. Cacciari, G. P. Salam, and G. Soyez, *The Anti-k(t) jet clustering algorithm*, JHEP **04** (2008) 063, arXiv: `0802.1189 [hep-ph]` (cit. on p. 12).

[94] N. Kauer and G. Passarino, *Inadequacy of zero-width approximation for a light Higgs boson signal*, JHEP **1208** (2012) 116, arXiv: `1206.4803 [hep-ph]` (cit. on pp. 12, 33).

[95] F. Caola and K. Melnikov, *Constraining the Higgs boson width with ZZ production at the LHC*, Phys. Rev. **D88** (2013) 054024, arXiv: `1307.4935 [hep-ph]` (cit. on pp. 12, 33).

[96] J. M. Campbell, R. K. Ellis, and C. Williams, *Bounding the Higgs width at the LHC using full analytic results for* $gg \to e^- e^+ \mu^- \mu^+$, JHEP **1404** (2014) 060, arXiv: `1311.3589 [hep-ph]` (cit. on p. 12).

[97] J. M. Campbell, R. K. Ellis, and C. Williams, *Bounding the Higgs width at the LHC: Complementary results from $H \to WW$*, Phys. Rev. **D89** (2014) 053011, arXiv: `1312.1628 [hep-ph]` (cit. on p. 12).

[98] C. Englert, Y. Soreq, and M. Spannowsky, *Off-Shell Higgs Coupling Measurements in BSM scenarios*, JHEP **05** (2015) 145, arXiv: `1410.5440 [hep-ph]` (cit. on p. 12).

[99] H. E. Logan, *Hiding a Higgs width enhancement from off-shell gg(→h*)→ZZ measurements*, Phys. Rev. D **92** (2015) 075038, arXiv: `1412.7577 [hep-ph]` (cit. on p. 12).

[100] ATLAS Collaboration, *Search for heavy ZZ resonances in the $\ell^+\ell^-\ell^+\ell^-$ and $\ell^+\ell^-\nu\bar{\nu}$ final states using proton–proton collisions at $\sqrt{s} = 13\,\text{TeV}$ with the ATLAS detector*, Eur. Phys. J. C **78** (2018) 293, arXiv: `1712.06386 [hep-ex]` (cit. on p. 12).

[101] R. J. Barlow and C. Beeston, *Fitting using finite Monte Carlo samples*, Comput. Phys. Commun. **77** (1993) 219 (cit. on p. 13).

[102] K. Cranmer, G. Lewis, L. Moneta, A. Shibata, and W. Verkerke, *HistFactory: A tool for creating statistical models for use with RooFit and RooStats*, CERN-OPEN-2012-016 (2012), URL: `http://cdsweb.cern.ch/record/1456844` (cit. on p. 13).

[103] G. Cowan, K. Cranmer, E. Gross, and O. Vitells, *Asymptotic formulae for likelihood-based tests of new physics*, Eur. Phys. J. C **71** (2011) 1554, Erratum in Eur. Phys. J. C73 (2013) 2501, arXiv: `1007.1727 [physics.data-an]` (cit. on p. 14).

[104] A. L. Read, *Presentation of search results: The CL(s) technique*, J. Phys. **G28** (2002) 2693 (cit. on p. 14).

[105] ATLAS Collaboration, *Measurements of the Higgs boson production and decay rates and coupling strengths using pp collision data at $\sqrt{s} = 7$ and $8\,\text{TeV}$ in the ATLAS experiment*, Eur. Phys. J. C **76** (2016) 6, arXiv: `1507.04548 [hep-ex]` (cit. on p. 19).

[106] ATLAS Collaboration, *Evaluation of theoretical uncertainties for simplified template cross section measurements of V-associated production of the Higgs boson*, ATL-PHYS-PUB-2018-035, 2018, URL: `https://cds.cern.ch/record/2649241` (cit. on p. 27).

[107] ATLAS Collaboration, *Constraints on the off-shell Higgs boson signal strength in the high-mass ZZ and WW final states with the ATLAS detector*, Eur. Phys. J. C **75** (2015) 335, arXiv: `1503.01060 [hep-ex]` (cit. on p. 33).

[108] C. Englert, M. McCullough, and M. Spannowsky, *Gluon-initiated associated production boosts Higgs physics*, Phys. Rev. **D89** (2014) 013013, arXiv: `1310.4828 [hep-ph]` (cit. on p. 34).

[109] ALEPH, CDF, D0, DELPHI, L3, OPAL, SLD Collaborations; LEP and Tevatron Electroweak Working Group; and SLD Electroweak and Heavy Flavour Groups, *Precision Electroweak Measurements and Constraints on the Standard Model*, (2010), arXiv: `1012.2367 [hep-ex]` (cit. on p. 43).

[110] T. Lee, *A Theory of Spontaneous T Violation*, Phys. Rev. D **8** (1973) 1226 (cit. on p. 44).

[111] J. F. Gunion and H. E. Haber, *The CP conserving two Higgs doublet model: The Approach to the decoupling limit*, Phys. Rev. D **67** (2003) 075019, arXiv: `hep-ph/0207010` (cit. on p. 44).

[112] G. Branco et al., *Theory and phenomenology of two-Higgs-doublet models*, Phys. Rept. **516** (2012) 1, arXiv: `1106.0034 [hep-ph]` (cit. on pp. 44, 45).

[113] Y. A. Gol'fand and E. P. Likhtman, *Extension of the Algebra of Poincare Group Generators and Violation of p Invariance*, JETP Lett. **13** (1971) 323, [Pisma Zh.Eksp.Teor.Fiz.13:452-455,1971] (cit. on p. 44).

[114] D. V. Volkov and V. P. Akulov, *Is the Neutrino a Goldstone Particle?* Phys. Lett. **B46** (1973) 109 (cit. on p. 44).

[115] J. Wess and B. Zumino, *Supergauge Transformations in Four-Dimensions*, Nucl. Phys. **B70** (1974) 39 (cit. on p. 44).

[116] J. Wess and B. Zumino, *Supergauge Invariant Extension of Quantum Electrodynamics*, Nucl. Phys. **B78** (1974) 1 (cit. on p. 44).

[117] S. Ferrara and B. Zumino, *Supergauge Invariant Yang-Mills Theories*, Nucl. Phys. **B79** (1974) 413 (cit. on p. 44).

[118] A. Salam and J. A. Strathdee, *Supersymmetry and Nonabelian Gauges*, Phys. Lett. **51B** (1974) 353 (cit. on p. 44).

[119] S. L. Glashow and S. Weinberg, *Natural Conservation Laws for Neutral Currents*, Phys. Rev. **D15** (1977) 1958 (cit. on p. 44).

[120] E. A. Paschos, *Diagonal Neutral Currents*, Phys. Rev. **D15** (1977) 1966 (cit. on p. 44).

[121] P. Fayet, *Supergauge Invariant Extension of the Higgs Mechanism and a Model for the electron and Its Neutrino*, Nucl. Phys. **B90** (1975) 104 (cit. on p. 45).

[122] P. Fayet, *Supersymmetry and Weak, Electromagnetic and Strong Interactions*, Phys. Lett. **B64** (1976) 159 (cit. on p. 45).

[123] P. Fayet, *Spontaneously Broken Supersymmetric Theories of Weak, Electromagnetic and Strong Interactions*, Phys. Lett. **B69** (1977) 489 (cit. on p. 45).

[124] L. Maiani, A. D. Polosa, and V. Riquer, *Bounds to the Higgs Sector Masses in Minimal Supersymmetry from LHC Data*, Phys. Lett. **B724** (2013) 274, arXiv: `1305.2172 [hep-ph]` (cit. on p. 45).

[125] A. Djouadi et al., *The post-Higgs MSSM scenario: Habemus MSSM?* Eur. Phys. J. **C73** (2013) 2650, arXiv: `1307.5205 [hep-ph]` (cit. on p. 45).

[126] A. Djouadi, L. Maiani, A. Polosa, J. Quevillon, and V. Riquer, *Fully covering the MSSM Higgs sector at the LHC*, JHEP **06** (2015) 168, arXiv: `1502.05653 [hep-ph]` (cit. on p. 45).

Auxiliary material

A Combined measurements of decay branching ratios

Table 13 and Figure 20 show the results of a fit to the data using as free parameters the ratios of the branching ratios into $\gamma\gamma$, ZZ^*, WW^*, $\tau\tau$ and $b\bar{b}$ to their values in the SM. The Higgs boson production processes are assumed to follow SM predictions.

Table 13: Best-fit values and uncertainties of the decay branching ratios of the Higgs boson, measured under SM assumptions for the Higgs boson production processes. The total uncertainties are decomposed into components for data statistics, experimental systematic uncertainties, and theory uncertainties on the modeling of the signal and background processes. SM predictions [26] are shown for the branching ratio into each decay channel. The five-dimensional compatibility with the SM hypothesis corresponds to a p-value of $p_{\mathrm{SM}} = 74\%$.

Branching ratio	Value	Uncertainty				
		Total	Stat.	Exp.	Sig. theo.	Bkg. theo.
$\mathrm{B}_{\gamma\gamma}/\mathrm{B}_{\gamma\gamma}^{\mathrm{SM}}$	1.06	±0.12	±0.08	$^{+0.08}_{-0.07}$	±0.05	±0.01
$\mathrm{B}_{ZZ}/\mathrm{B}_{ZZ}^{\mathrm{SM}}$	1.20	$^{+0.15}_{-0.14}$	±0.12	±0.05	$^{+0.07}_{-0.05}$	±0.02
$\mathrm{B}_{WW}/\mathrm{B}_{WW}^{\mathrm{SM}}$	1.05	$^{+0.17}_{-0.16}$	±0.09	±0.09	$^{+0.06}_{-0.05}$	±0.07
$\mathrm{B}_{\tau\tau}/\mathrm{B}_{\tau\tau}^{\mathrm{SM}}$	1.10	$^{+0.28}_{-0.26}$	±0.18	$^{+0.17}_{-0.16}$	$^{+0.12}_{-0.08}$	$^{+0.06}_{-0.05}$
$\mathrm{B}_{bb}/\mathrm{B}_{bb}^{\mathrm{SM}}$	1.17	$^{+0.24}_{-0.23}$	±0.15	±0.11	$^{+0.09}_{-0.06}$	$^{+0.13}_{-0.12}$

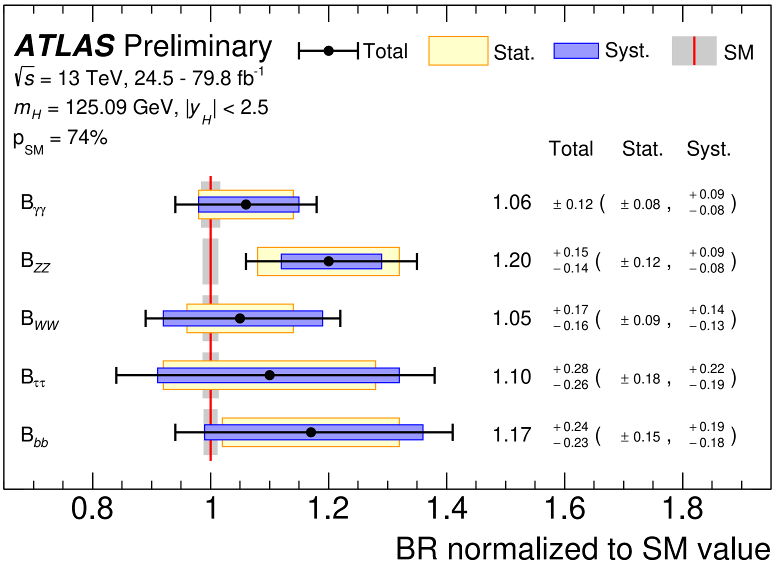

Figure 20: Branching ratios for $H\rightarrow\gamma\gamma$, $H\rightarrow ZZ^*$, $H\rightarrow WW^*$, $H\rightarrow\tau\tau$ and $H\rightarrow b\bar{b}$ normalized to their SM predictions, measured under SM assumptions for the Higgs boson production processes. The black error bars, blue boxes and yellow boxes show the total, systematic, and statistical uncertainties in the measurements, respectively. The blue bands indicate the theory uncertainties on the predictions.

B Additional figures for production cross section measurements

Figure 21 shows the same combined contours as shown in Figures 4, without the contours for the input analyses overlaid. The correlations between the parameters of the ratio model of Section 5.4 are summarized in Figure 22.

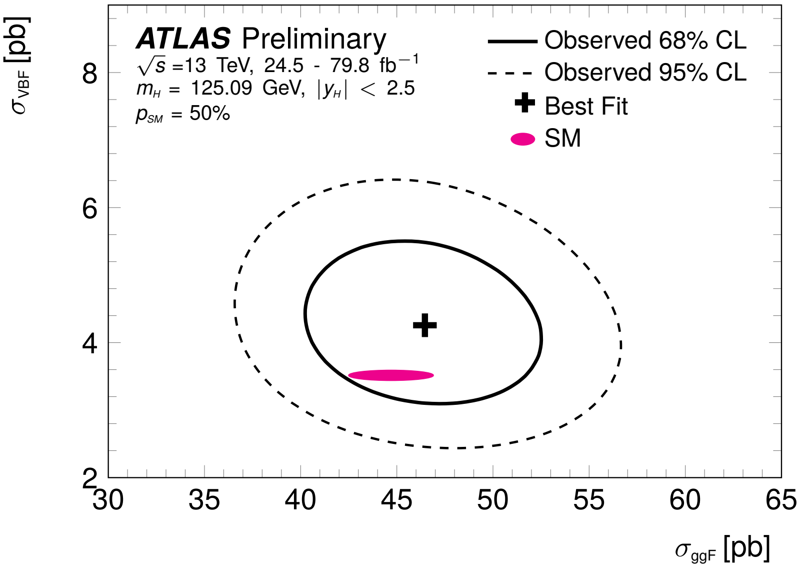

Figure 21: Observed contours at 68% and 95% CL in the plane of σ_{VBF} versus σ_{ggF}, defined in the asymptotic approximation by $-2\ln\Lambda = 2.28$ and 5.99, respectively. The cross indicates the best-fit value and the solid ellipse the SM prediction. The Higgs boson decay branching fractions are fixed to their SM values.

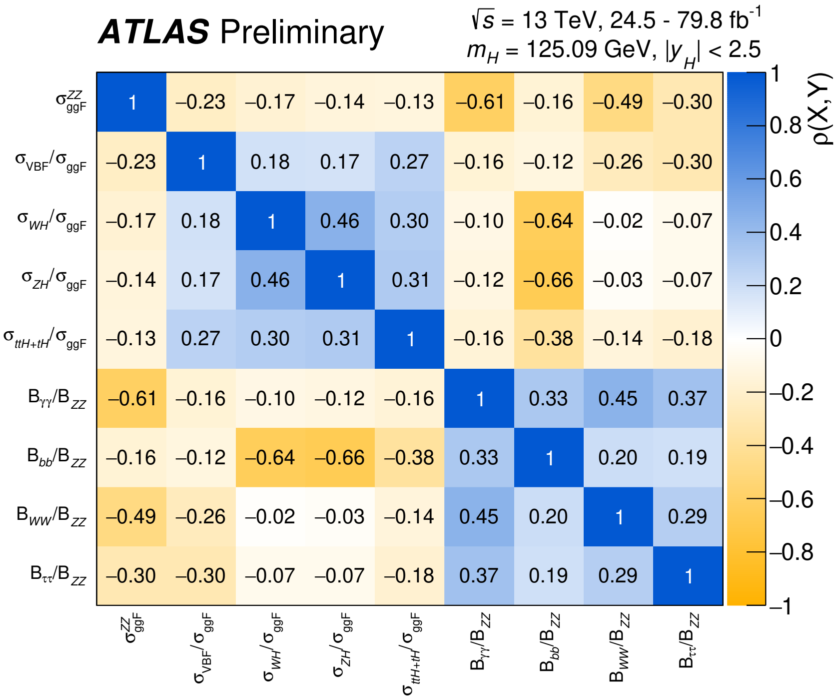

	σ^{ZZ}_{ggF}	$\sigma_{\text{VBF}}/\sigma_{\text{ggF}}$	$\sigma_{WH}/\sigma_{\text{ggF}}$	$\sigma_{ZH}/\sigma_{\text{ggF}}$	$\sigma_{ttH+tH}/\sigma_{\text{ggF}}$	$B_{\gamma\gamma}/B_{ZZ}$	B_{bb}/B_{ZZ}	B_{WW}/B_{ZZ}	$B_{\tau\tau}/B_{ZZ}$
σ^{ZZ}_{ggF}	1	−0.23	−0.17	−0.14	−0.13	−0.61	−0.16	−0.49	−0.30
$\sigma_{\text{VBF}}/\sigma_{\text{ggF}}$	−0.23	1	0.18	0.17	0.27	−0.16	−0.12	−0.26	−0.30
$\sigma_{WH}/\sigma_{\text{ggF}}$	−0.17	0.18	1	0.46	0.30	−0.10	−0.64	−0.02	−0.07
$\sigma_{ZH}/\sigma_{\text{ggF}}$	−0.14	0.17	0.46	1	0.31	−0.12	−0.66	−0.03	−0.07
$\sigma_{ttH+tH}/\sigma_{\text{ggF}}$	−0.13	0.27	0.30	0.31	1	−0.16	−0.38	−0.14	−0.18
$B_{\gamma\gamma}/B_{ZZ}$	−0.61	−0.16	−0.10	−0.12	−0.16	1	0.33	0.45	0.37
B_{bb}/B_{ZZ}	−0.16	−0.12	−0.64	−0.66	−0.38	0.33	1	0.20	0.19
B_{WW}/B_{ZZ}	−0.49	−0.26	−0.02	−0.03	−0.14	0.45	0.20	1	0.29
$B_{\tau\tau}/B_{ZZ}$	−0.30	−0.30	−0.07	−0.07	−0.18	0.37	0.19	0.29	1

Figure 22: Correlation matrix for the measured values of σ^{ZZ}_{ggF}, together with ratios of production cross sections normalized to σ_{ggF}, and ratios of branching fractions normalized to B_{ZZ}.

C Alternative parametrization for measuring ratios of cross sections and branching fractions

An alternative parametrization from the one introduced in Section 5.4 for measuring ratios of cross sections and branching fractions has been tested in order to reduce the correlations between the parameters of interest. The products $(\sigma \times \mathrm{B})_{if}$ measured in Section 5.3 can be expressed as follows: $\sigma^{ZZ}_{\mathrm{ggF}}$ is taken as the normalization for the ggF, VBF and $t\bar{t}H$ production modes, while $\sigma^{b\bar{b}}_{WH}$ and $\sigma^{b\bar{b}}_{ZH}$ are taken as normalization for the WH and ZH production modes, respectively:

$$(\sigma \times \mathrm{B})_{if} = \sigma^{ZZ}_{\mathrm{ggF}} \cdot \left(\frac{\sigma_i}{\sigma_{\mathrm{ggF}}}\right) \cdot \left(\frac{\mathrm{B}_f}{\mathrm{B}_{zz}}\right) \qquad \text{for } i = \mathrm{ggF}, \mathrm{VBF}, t\bar{t}H \tag{11}$$

$$(\sigma \times \mathrm{B})_{if} = \sigma^{bb}_{WH} \cdot \left(\frac{\sigma_i}{\sigma_{WH}}\right) \cdot \left(\frac{\mathrm{B}_f}{\mathrm{B}_{bb}}\right) \qquad \text{for } i = WH \tag{12}$$

$$(\sigma \times \mathrm{B})_{if} = \sigma^{bb}_{ZH} \cdot \left(\frac{\sigma_i}{\sigma_{ZH}}\right) \cdot \left(\frac{\mathrm{B}_f}{\mathrm{B}_{bb}}\right) \qquad \text{for } i = ZH. \tag{13}$$

Results are shown in Figure 23 and Table 14. The correlations between the measured parameters are summarized in Figure 24. The compatibility between the measurements and the SM predictions corresponds to a p-value of $p_{\mathrm{SM}} = 93\%$.

Table 14: Best-fit values and uncertainties of $\sigma^{ZZ}_{\mathrm{ggF}}$, $\sigma_{\mathrm{VBF}}/\sigma_{\mathrm{ggF}}$, $\sigma^{b\bar{b}}_{WH}$, $\sigma^{b\bar{b}}_{ZH}$, $\sigma_{t\bar{t}H+tH}/\sigma_{\mathrm{ggF}}$, together with ratios of production cross sections normalized to σ_{ggF}, and ratios of branching fractions normalized to B_{ZZ}. Uncertainties in the SM predictions are computed following the same method as for Ref. [3].

Quantity	Value	Uncertainty			SM prediction
		Total	Stat.	Syst.	
$\sigma^{ZZ}_{\mathrm{ggF}}$ [pb]	1.33	± 0.15	$(^{+0.14}_{-0.13}$	$\pm 0.07)$	1.181 ± 0.061
$\sigma_{\mathrm{VBF}}/\sigma_{\mathrm{ggF}}$	0.097	$^{+0.025}_{-0.021}$	$(^{+0.019}_{-0.017}$	$^{+0.017}_{-0.012})$	0.0786 ± 0.0043
$\sigma^{b\bar{b}}_{WH}$	910	$^{+290}_{-270}$	$(^{+200}_{-190}$	$^{+220}_{-200})$	700 ± 16
$\sigma^{b\bar{b}}_{ZH}$	490	$^{+150}_{-140}$	$(^{+120}_{-110}$	$^{+100}_{-90})$	463^{+20}_{-16}
$\sigma_{t\bar{t}H+tH}/\sigma_{\mathrm{ggF}}$	0.0159	$^{+0.0041}_{-0.0035}$	$(^{+0.0031}_{-0.0029}$	$^{+0.0026}_{-0.0021})$	$0.0131^{+0.0010}_{-0.0013}$
$\mathrm{B}_{\gamma\gamma}/\mathrm{B}_{ZZ}$	0.075	$^{+0.012}_{-0.010}$	$(^{+0.010}_{-0.009}$	$^{+0.006}_{-0.005})$	0.0860 ± 0.0010
$\mathrm{B}_{WW}/\mathrm{B}_{ZZ}$	6.8	$^{+1.5}_{-1.2}$	$(^{+1.1}_{-0.9}$	$^{+1.0}_{-0.9})$	$8.15 \pm < 0.01$
$\mathrm{B}_{\tau\tau}/\mathrm{B}_{ZZ}$	2.04	$^{+0.62}_{-0.52}$	$(^{+0.45}_{-0.40}$	$^{+0.40}_{-0.33})$	2.37 ± 0.02
$\mathrm{B}_{bb}/\mathrm{B}_{ZZ}$	20.2	$^{+8.4}_{-5.9}$	$(^{+5.9}_{-4.6}$	$^{+5.7}_{-4.0})$	22.0 ± 0.5

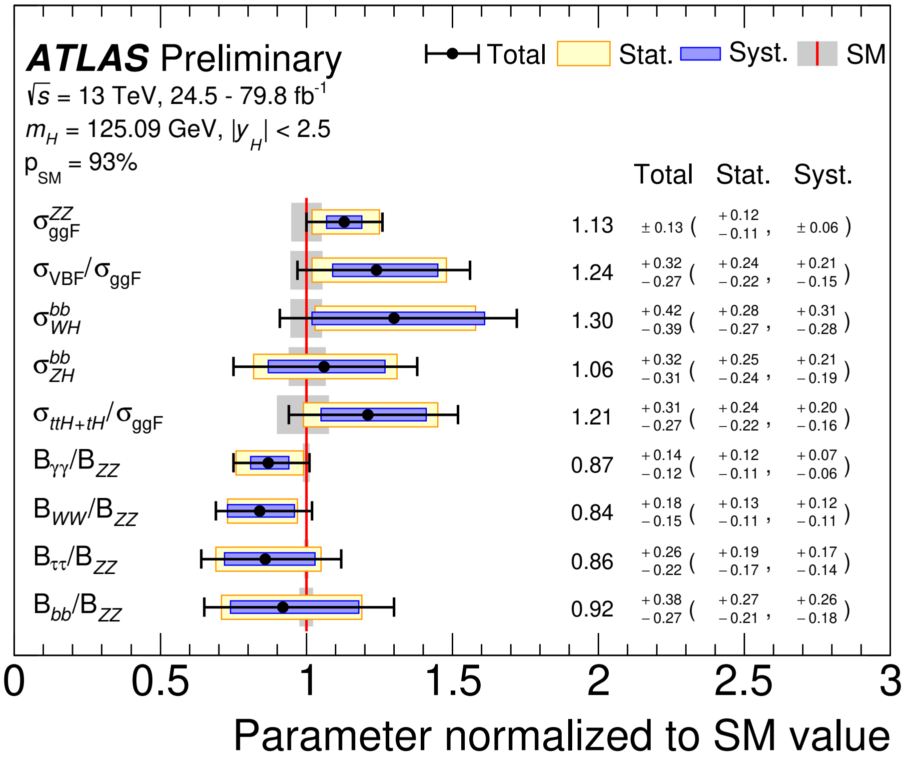

Figure 23: Results of a simultaneous fit for σ^{ZZ}_{ggF}, $\sigma_{\text{VBF}}/\sigma_{\text{ggF}}$, $\sigma^{b\bar{b}}_{WH}$, $\sigma^{b\bar{b}}_{ZH}$, $\sigma_{t\bar{t}H+tH}/\sigma_{\text{ggF}}$, $\text{B}_{\gamma\gamma}/\text{B}_{ZZ}$, $\text{B}_{WW}/\text{B}_{ZZ}$, $\text{B}_{\tau\tau}/\text{B}_{ZZ}$, and $\text{B}_{bb}/\text{B}_{ZZ}$. The fit results are normalized to the SM predictions. The black error bars, blue boxes and yellow boxes show the total, systematic, and statistical uncertainties in the measurements, respectively. The gray bands show the theory uncertainties in the predictions.

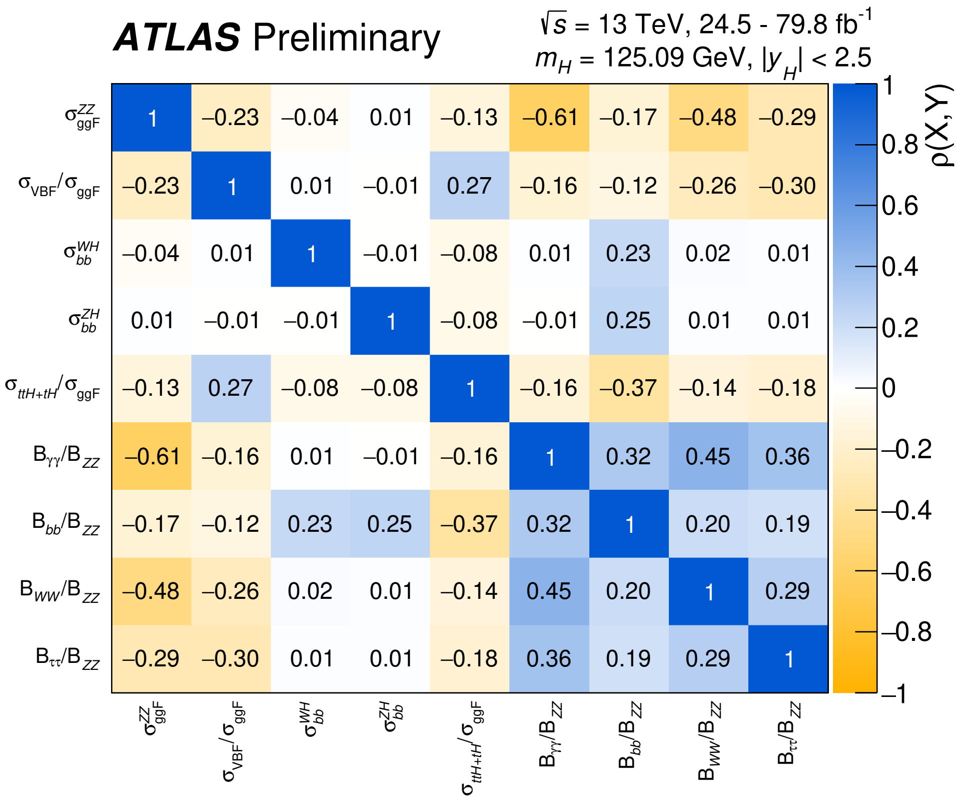

	σ_{ggF}^{ZZ}	$\sigma_{\text{VBF}}/\sigma_{\text{ggF}}$	σ_{bb}^{WH}	σ_{bb}^{ZH}	$\sigma_{ttH+tH}/\sigma_{\text{ggF}}$	$B_{\gamma\gamma}/B_{ZZ}$	B_{bb}/B_{ZZ}	B_{WW}/B_{ZZ}	$B_{\tau\tau}/B_{ZZ}$
σ_{ggF}^{ZZ}	1	−0.23	−0.04	0.01	−0.13	−0.61	−0.17	−0.48	−0.29
$\sigma_{\text{VBF}}/\sigma_{\text{ggF}}$	−0.23	1	0.01	−0.01	0.27	−0.16	−0.12	−0.26	−0.30
σ_{bb}^{WH}	−0.04	0.01	1	−0.01	−0.08	0.01	0.23	0.02	0.01
σ_{bb}^{ZH}	0.01	−0.01	−0.01	1	−0.08	−0.01	0.25	0.01	0.01
$\sigma_{ttH+tH}/\sigma_{\text{ggF}}$	−0.13	0.27	−0.08	−0.08	1	−0.16	−0.37	−0.14	−0.18
$B_{\gamma\gamma}/B_{ZZ}$	−0.61	−0.16	0.01	−0.01	−0.16	1	0.32	0.45	0.36
B_{bb}/B_{ZZ}	−0.17	−0.12	0.23	0.25	−0.37	0.32	1	0.20	0.19
B_{WW}/B_{ZZ}	−0.48	−0.26	0.02	0.01	−0.14	0.45	0.20	1	0.29
$B_{\tau\tau}/B_{ZZ}$	−0.29	−0.30	0.01	0.01	−0.18	0.36	0.19	0.29	1

Figure 24: Correlation matrix for the measured values of σ_{ggF}^{ZZ}, $\sigma_{\text{VBF}}/\sigma_{\text{ggF}}$, $\sigma_{WH}^{b\bar{b}}$, $\sigma_{ZH}^{b\bar{b}}$, $\sigma_{t\bar{t}H+tH}/\sigma_{\text{ggF}}$, $\text{B}_{\gamma\gamma}/\text{B}_{ZZ}$, $\text{B}_{WW}/\text{B}_{ZZ}$, $\text{B}_{\tau\tau}/\text{B}_{ZZ}$, and $\text{B}_{bb}/\text{B}_{ZZ}$.

D Simplified template cross section measurements with ratios of branching fractions set to their SM values

This section presents measurements of STXS parameters in a model similar to that of Section 6.2, but with the ratios of Higgs boson branching fractions $\mathrm{B}_f/\mathrm{B}_{ZZ}$ for final states f other than ZZ fixed to their SM values within uncertainties. The parameters of interest are thus the cross sections in each measurement region. The results are shown in Figure 25 and Table 15. The observed (expected) upper limits at 95% CL on the cross sections in the $qq \to Hqq$, $(V \to q\bar{q})H$ and $qq \to Hqq$, $p_T^j \geq 200$ GeV bins are set at 1.25 (1.32) pb and 0.47 (0.62) pb, respectively, using the CL_s method. The results show good overall agreement with the SM predictions in each region. The compatibility between the measurement and the SM prediction corresponds to a p-value of $p_{\mathrm{SM}} = 80\%$, computed using the procedure outlined in Section 4 with 15 degrees of freedom. The correlations between the measured parameters are shown in Figure 26.

Table 15: Best-fit values and uncertainties of the cross sections in each measurement region. The SM predictions [26] are shown for each quantity. The parameters directly extracted from the fit are σ_i. The ratios of Higgs boson branching fractions $\mathrm{B}_f/\mathrm{B}_{ZZ}$ for final states f other than ZZ fixed to their SM values within uncertainties.

Measurement region $\left(\sigma_i\right)$	Result [pb]	Uncertainty [pb]			SM prediction [pb]
		Total	Stat.	Syst.	
$gg \to H$, 0-jet	32.5	± 3.6	± 2.8	± 2.5	27.5 ± 1.7
$gg \to H$, 1-jet, $p_{\mathrm{T}}^{H} < 60$ GeV	3.5	$^{+2.6}_{-2.5}$	$^{+2.1}_{-2.0}$	± 1.4	6.6 ± 0.9
$gg \to H$, 1-jet, $60 \leq p_{\mathrm{T}}^{H} < 120$ GeV	3.7	$^{+1.5}_{-1.4}$	$^{+1.3}_{-1.2}$	$^{+0.8}_{-0.7}$	4.6 ± 0.6
$gg \to H$, 1-jet, $120 \leq p_{\mathrm{T}}^{H} < 200$ GeV	0.9	± 0.5	± 0.4	$^{+0.3}_{-0.2}$	0.75 ± 0.15
$gg \to H$, $\geq$ 1-jet, $p_{\mathrm{T}}^{H} \geq 200$ GeV	1.1	$^{+0.4}_{-0.3}$	± 0.3	± 0.2	0.59 ± 0.16
$gg \to H$, $\geq$ 2-jet, $p_{\mathrm{T}}^{H} < 200$ GeV	4.9	$^{+2.3}_{-2.2}$	$^{+1.9}_{-1.8}$	$^{+1.4}_{-1.2}$	4.8 ± 1.0
$qq \to Hqq$, VBF topo + Rest	5.6	$^{+1.3}_{-1.2}$	± 1.0	$^{+0.9}_{-0.7}$	4.07 ± 0.07
$qq \to Hqq$, VH topo	−0.06	$^{+0.61}_{-0.52}$	$^{+0.59}_{-0.51}$	$^{+0.15}_{-0.11}$	0.515 ± 0.018
$qq \to Hqq$, $p_T^j \geq 200$ GeV	−0.19	$^{+0.29}_{-0.28}$	$^{+0.25}_{-0.24}$	$^{+0.13}_{-0.14}$	0.220 ± 0.004
$qq \to H\ell\nu$, $p_T^V < 250$ GeV	0.67	$^{+0.30}_{-0.28}$	± 0.22	$^{+0.19}_{-0.17}$	0.393 ± 0.008
$qq \to H\ell\nu$, $p_T^V \geq 250$ GeV	0.014	$^{+0.009}_{-0.008}$	± 0.007	± 0.005	0.0122 ± 0.0005
$gg/qq \to H\ell\ell$, $p_T^V < 150$ GeV	0.17	± 0.16	$^{+0.13}_{-0.12}$	± 0.10	0.200 ± 0.008
$gg/qq \to H\ell\ell$, $150 \geq p_T^V < 250$ GeV	0.020	± 0.022	± 0.018	± 0.012	0.0324 ± 0.0040
$gg/qq \to H\ell\ell$, $p_T^V \geq 250$ GeV	0.015	$^{+0.008}_{-0.007}$	$^{+0.007}_{-0.006}$	$^{+0.004}_{-0.002}$	0.0083 ± 0.0009
$t\bar{t}H$+tH	0.70	$^{+0.15}_{-0.14}$	± 0.10	$^{+0.12}_{-0.11}$	$0.59^{+0.03}_{-0.05}$

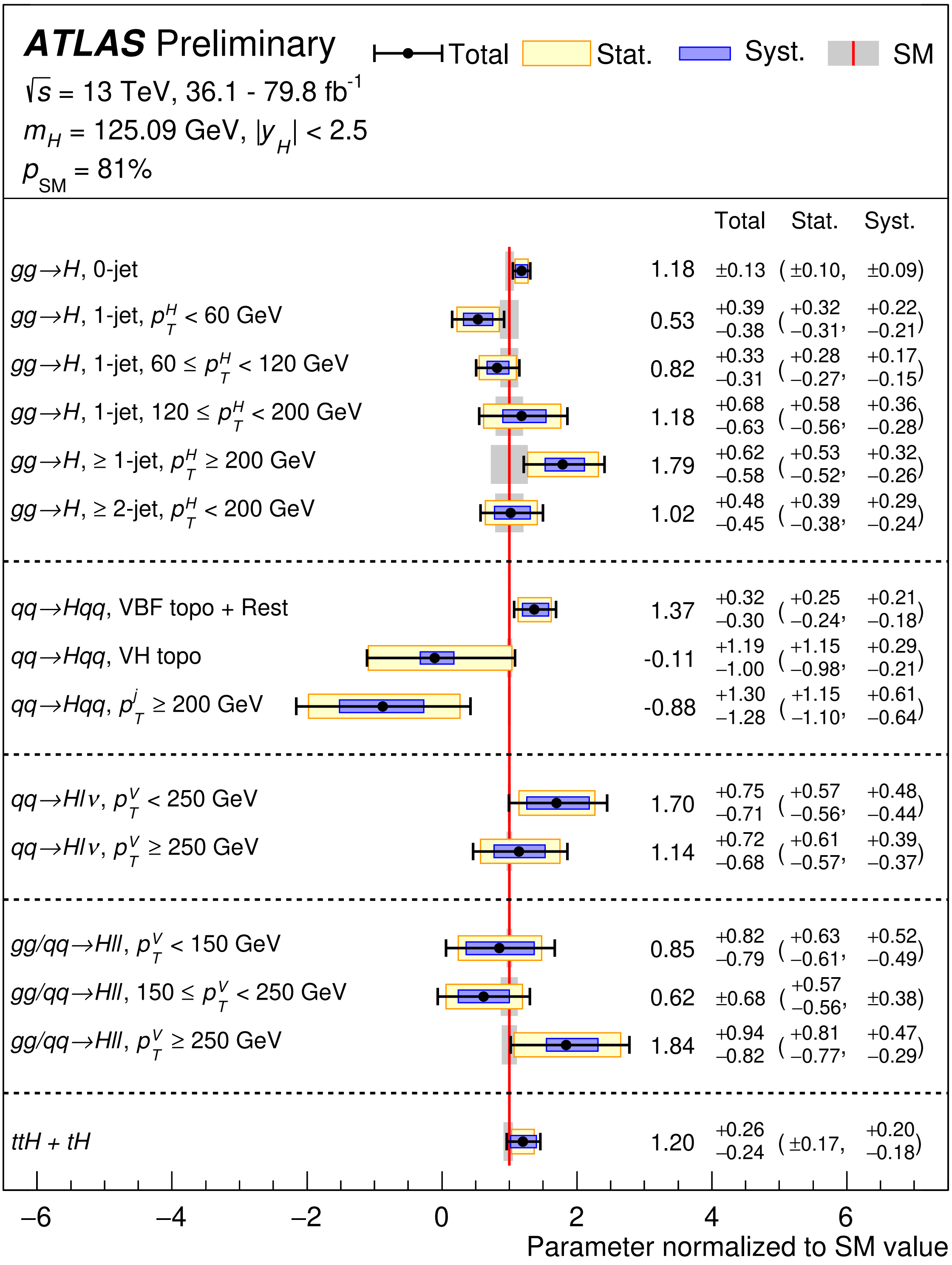

Figure 25: Best-fit values and uncertainties of the cross sections in each measurement region in a model where all the branching fractions are assumed to be as in the SM. The results are shown normalized to the SM predictions for the various parameters. The black error bar shows the total uncertainty on each measurement.

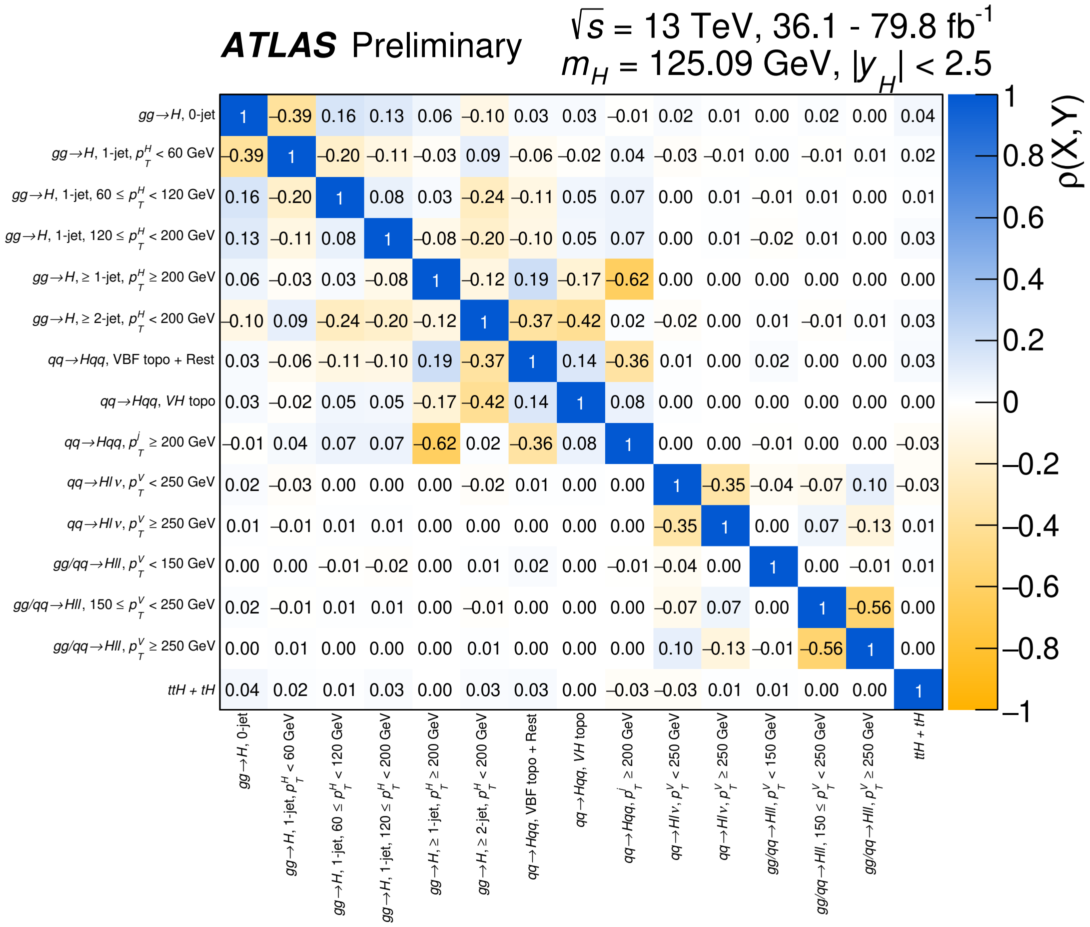

	$gg\to H$, 0-jet	$gg\to H$, 1-jet, $p_T^H < 60$ GeV	$gg\to H$, 1-jet, $60 \leq p_T^H < 120$ GeV	$gg\to H$, 1-jet, $120 \leq p_T^H < 200$ GeV	$gg\to H$, $\geq$ 1-jet, $p_T^H \geq 200$ GeV	$gg\to H$, $\geq$ 2-jet, $p_T^H < 200$ GeV	$qq\to Hqq$, VBF topo + Rest	$qq\to Hqq$, VH topo	$qq\to Hqq$, $p_T^j \geq 200$ GeV	$qq\to Hl\nu$, $p_T^V < 250$ GeV	$qq\to Hl\nu$, $p_T^V \geq 250$ GeV	$gg/qq\to Hll$, $p_T^V < 150$ GeV	$gg/qq\to Hll$, $150 \leq p_T^V < 250$ GeV	$gg/qq\to Hll$, $p_T^V \geq 250$ GeV	$ttH + tH$
$gg\to H$, 0-jet	1	−0.39	0.16	0.13	0.06	−0.10	0.03	0.03	−0.01	0.02	0.01	0.00	0.02	0.00	0.04
$gg\to H$, 1-jet, $p_T^H < 60$ GeV	−0.39	1	−0.20	−0.11	−0.03	0.09	−0.06	−0.02	0.04	−0.03	−0.01	0.00	−0.01	0.01	0.02
$gg\to H$, 1-jet, $60 \leq p_T^H < 120$ GeV	0.16	−0.20	1	0.08	0.03	−0.24	−0.11	0.05	0.07	0.00	0.01	−0.01	0.01	0.00	0.01
$gg\to H$, 1-jet, $120 \leq p_T^H < 200$ GeV	0.13	−0.11	0.08	1	−0.08	−0.20	−0.10	0.05	0.07	0.00	0.01	−0.02	0.01	0.00	0.03
$gg\to H$, $\geq$ 1-jet, $p_T^H \geq 200$ GeV	0.06	−0.03	0.03	−0.08	1	−0.12	0.19	−0.17	−0.62	0.00	0.00	0.00	0.00	0.00	0.00
$gg\to H$, $\geq$ 2-jet, $p_T^H < 200$ GeV	−0.10	0.09	−0.24	−0.20	−0.12	1	−0.37	−0.42	0.02	−0.02	0.00	0.01	−0.01	0.01	0.03
$qq\to Hqq$, VBF topo + Rest	0.03	−0.06	−0.11	−0.10	0.19	−0.37	1	0.14	−0.36	0.01	0.00	0.02	0.00	0.00	0.03
$qq\to Hqq$, VH topo	0.03	−0.02	0.05	0.05	−0.17	−0.42	0.14	1	0.08	0.00	0.00	0.00	0.00	0.00	0.00
$qq\to Hqq$, $p_T^j \geq 200$ GeV	−0.01	0.04	0.07	0.07	−0.62	0.02	−0.36	0.08	1	0.00	0.00	−0.01	0.00	0.00	−0.03
$qq\to Hl\nu$, $p_T^V < 250$ GeV	0.02	−0.03	0.00	0.00	0.00	−0.02	0.01	0.00	0.00	1	−0.35	−0.04	−0.07	0.10	−0.03
$qq\to Hl\nu$, $p_T^V \geq 250$ GeV	0.01	−0.01	0.01	0.01	0.00	0.00	0.00	0.00	0.00	−0.35	1	0.00	0.07	−0.13	0.01
$gg/qq\to Hll$, $p_T^V < 150$ GeV	0.00	0.00	−0.01	−0.02	0.00	0.01	0.02	0.00	−0.01	−0.04	0.00	1	0.00	−0.01	0.01
$gg/qq\to Hll$, $150 \leq p_T^V < 250$ GeV	0.02	−0.01	0.01	0.01	0.00	−0.01	0.00	0.00	0.00	−0.07	0.07	0.00	1	−0.56	0.00
$gg/qq\to Hll$, $p_T^V \geq 250$ GeV	0.00	0.01	0.00	0.00	0.00	0.01	0.00	0.00	0.00	0.10	−0.13	−0.01	−0.56	1	0.00
$ttH + tH$	0.04	0.02	0.01	0.03	0.00	0.03	0.03	0.00	−0.03	−0.03	0.01	0.01	0.00	0.00	1

Figure 26: Correlation matrix for the measured values of the simplified template cross sections in each measurement region in a model where the all the branching fractions are assumed to be as in the SM.

E Simplified template cross section measurement results with finer granularity

This section presents measurements of STXS parameters in a model with finer granularity compared to that of Section 6.2, and thus more close to the original proposal of Stage 1 STXS in Ref. [26, 27]. The results are shown in Figure 27 and 28

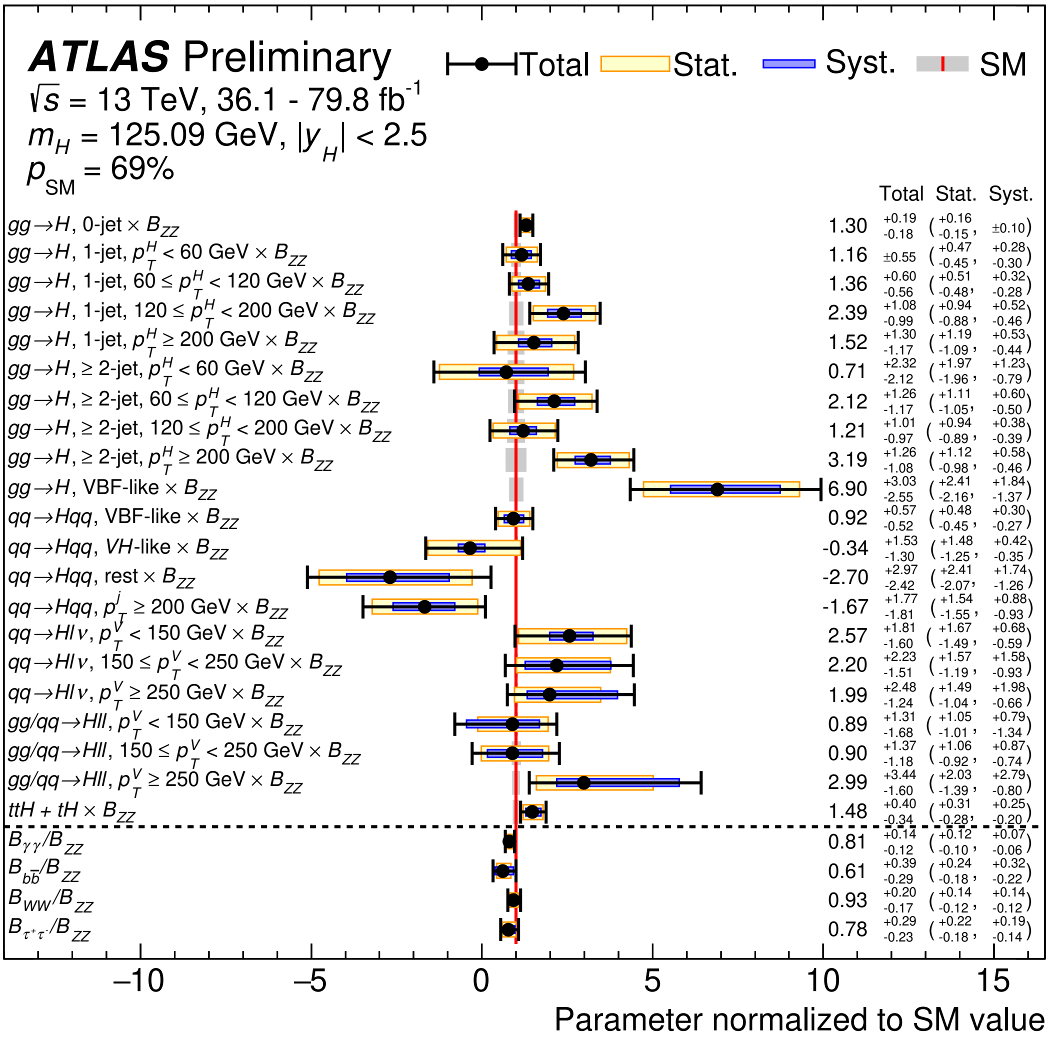

Figure 27: Best-fit values and uncertainties of the cross sections in each measurement region times the $H \to ZZ^*$ branching fraction in a model with finer granularity. The results are shown normalized to the SM predictions for the various parameters. The black error bar shows the total uncertainty on each measurement.

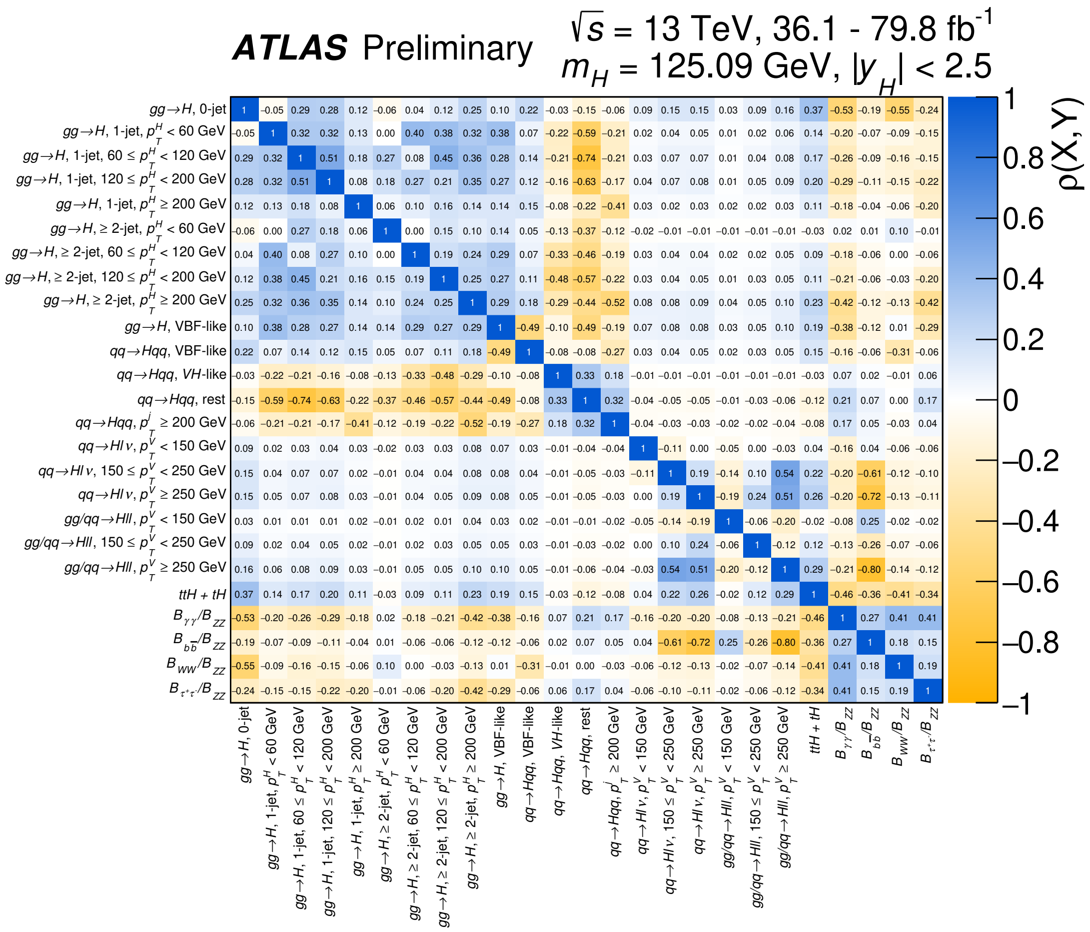

	$gg\to H$, 0-jet	$gg\to H$, 1-jet, $p_T^H < 60$ GeV	$gg\to H$, 1-jet, $60 \le p_T^H < 120$ GeV	$gg\to H$, 1-jet, $120 \le p_T^H < 200$ GeV	$gg\to H$, 1-jet, $p_T^H \ge 200$ GeV	$gg\to H$, $\ge$ 2-jet, $p_T^H < 60$ GeV	$gg\to H$, $\ge$ 2-jet, $60 \le p_T^H < 120$ GeV	$gg\to H$, $\ge$ 2-jet, $120 \le p_T^H < 200$ GeV	$gg\to H$, $\ge$ 2-jet, $p_T^H \ge 200$ GeV	$gg\to H$, VBF-like	$qq\to Hqq$, VBF-like	$qq\to Hqq$, VH-like	$qq\to Hqq$, rest	$qq\to Hqq$, $p_T^j \ge 200$ GeV	$qq\to Hl\nu$, $p_T^V < 150$ GeV	$qq\to Hl\nu$, $150 \le p_T^V < 250$ GeV	$qq\to Hl\nu$, $p_T^V \ge 250$ GeV	$gg/qq\to Hll$, $p_T^V < 150$ GeV	$gg/qq\to Hll$, $150 \le p_T^V < 250$ GeV	$gg/qq\to Hll$, $p_T^V \ge 250$ GeV	$ttH + tH$	$B_{\gamma\gamma}/B_{ZZ}$	$B_{b\bar{b}}/B_{ZZ}$	B_{WW}/B_{ZZ}	$B_{\tau^+\tau^-}/B_{ZZ}$
$gg\to H$, 0-jet	1	–0.05	0.29	0.28	0.12	–0.06	0.04	0.12	0.25	0.10	0.22	–0.03	–0.15	–0.06	0.09	0.15	0.15	0.03	0.09	0.16	0.37	–0.53	–0.19	–0.55	–0.24
$gg\to H$, 1-jet, $p_T^H < 60$ GeV	–0.05	1	0.32	0.32	0.13	0.00	0.40	0.38	0.32	0.38	0.07	–0.22	–0.59	–0.21	0.02	0.04	0.05	0.01	0.02	0.06	0.14	–0.20	–0.07	–0.09	–0.15
$gg\to H$, 1-jet, $60 \le p_T^H < 120$ GeV	0.29	0.32	1	0.51	0.18	0.27	0.08	0.45	0.36	0.28	0.14	–0.21	–0.74	–0.21	0.03	0.07	0.07	0.01	0.04	0.08	0.17	–0.26	–0.09	–0.16	–0.15
$gg\to H$, 1-jet, $120 \le p_T^H < 200$ GeV	0.28	0.32	0.51	1	0.08	0.18	0.27	0.21	0.35	0.27	0.12	–0.16	–0.63	–0.17	0.04	0.07	0.08	0.01	0.05	0.09	0.20	–0.29	–0.11	–0.15	–0.22
$gg\to H$, 1-jet, $p_T^H \ge 200$ GeV	0.12	0.13	0.18	0.08	1	0.06	0.10	0.16	0.14	0.14	0.15	–0.08	–0.22	–0.41	0.03	0.02	0.03	0.02	0.02	0.03	0.11	–0.18	–0.04	–0.06	–0.20
$gg\to H$, $\ge$ 2-jet, $p_T^H < 60$ GeV	–0.06	0.00	0.27	0.18	0.06	1	0.00	0.15	0.10	0.14	0.05	–0.13	–0.37	–0.12	–0.02	–0.01	–0.01	–0.01	–0.01	–0.01	–0.03	0.02	0.01	0.10	–0.01
$gg\to H$, $\ge$ 2-jet, $60 \le p_T^H < 120$ GeV	0.04	0.40	0.08	0.27	0.10	0.00	1	0.19	0.24	0.29	0.07	–0.33	–0.46	–0.19	0.03	0.04	0.04	0.02	0.02	0.05	0.09	–0.18	–0.06	0.00	–0.06
$gg\to H$, $\ge$ 2-jet, $120 \le p_T^H < 200$ GeV	0.12	0.38	0.45	0.21	0.16	0.15	0.19	1	0.25	0.27	0.11	–0.48	–0.57	–0.22	0.03	0.04	0.05	0.01	0.03	0.05	0.11	–0.21	–0.06	–0.03	–0.20
$gg\to H$, $\ge$ 2-jet, $p_T^H \ge 200$ GeV	0.25	0.32	0.36	0.35	0.14	0.10	0.24	0.25	1	0.29	0.18	–0.29	–0.44	–0.52	0.08	0.08	0.09	0.04	0.05	0.10	0.23	–0.42	–0.12	–0.13	–0.42
$gg\to H$, VBF-like	0.10	0.38	0.28	0.27	0.14	0.14	0.29	0.27	0.29	1	–0.49	–0.10	–0.49	–0.19	0.07	0.08	0.08	0.03	0.05	0.10	0.19	–0.38	–0.12	0.01	–0.29
$qq\to Hqq$, VBF-like	0.22	0.07	0.14	0.12	0.15	0.05	0.07	0.11	0.18	–0.49	1	–0.08	–0.08	–0.27	0.03	0.04	0.05	0.02	0.03	0.05	0.15	–0.16	–0.06	–0.31	–0.06
$qq\to Hqq$, VH-like	–0.03	–0.22	–0.21	–0.16	–0.08	–0.13	–0.33	–0.48	–0.29	–0.10	–0.08	1	0.33	0.18	–0.01	–0.01	–0.01	–0.01	–0.01	–0.01	–0.03	0.07	0.02	–0.01	0.06
$qq\to Hqq$, rest	–0.15	–0.59	–0.74	–0.63	–0.22	–0.37	–0.46	–0.57	–0.44	–0.49	–0.08	0.33	1	0.32	–0.04	–0.05	–0.05	–0.01	–0.03	–0.06	–0.12	0.21	0.07	0.00	0.17
$qq\to Hqq$, $p_T^j \ge 200$ GeV	–0.06	–0.21	–0.21	–0.17	–0.41	–0.12	–0.19	–0.22	–0.52	–0.19	–0.27	0.18	0.32	1	–0.04	–0.03	–0.03	–0.02	–0.02	–0.04	–0.08	0.17	0.05	–0.03	0.04
$qq\to Hl\nu$, $p_T^V < 150$ GeV	0.09	0.02	0.03	0.04	0.03	–0.02	0.03	0.03	0.08	0.07	0.03	–0.01	–0.04	–0.04	1	–0.11	0.00	–0.05	0.00	–0.03	0.04	–0.16	0.04	–0.06	–0.06
$qq\to Hl\nu$, $150 \le p_T^V < 250$ GeV	0.15	0.04	0.07	0.07	0.02	–0.01	0.04	0.04	0.08	0.08	0.04	–0.01	–0.05	–0.03	–0.11	1	0.19	–0.14	0.10	0.54	0.22	–0.20	–0.61	–0.12	–0.10
$qq\to Hl\nu$, $p_T^V \ge 250$ GeV	0.15	0.05	0.07	0.08	0.03	–0.01	0.04	0.05	0.09	0.08	0.05	–0.01	–0.05	–0.03	0.00	0.19	1	–0.19	0.24	0.51	0.26	–0.20	–0.72	–0.13	–0.11
$gg/qq\to Hll$, $p_T^V < 150$ GeV	0.03	0.01	0.01	0.01	0.02	–0.01	0.02	0.01	0.04	0.03	0.02	–0.01	–0.01	–0.02	–0.05	–0.14	–0.19	1	–0.06	–0.20	–0.02	–0.08	0.25	–0.02	–0.02
$gg/qq\to Hll$, $150 \le p_T^V < 250$ GeV	0.09	0.02	0.04	0.05	0.02	–0.01	0.02	0.03	0.05	0.05	0.03	–0.01	–0.03	–0.02	0.00	0.10	0.24	–0.06	1	–0.12	0.12	–0.13	–0.26	–0.07	–0.06
$gg/qq\to Hll$, $p_T^V \ge 250$ GeV	0.16	0.06	0.08	0.09	0.03	–0.01	0.05	0.05	0.10	0.10	0.05	–0.01	–0.06	–0.04	–0.03	0.54	0.51	–0.20	–0.12	1	0.29	–0.21	–0.80	–0.14	–0.12
$ttH + tH$	0.37	0.14	0.17	0.20	0.11	–0.03	0.09	0.11	0.23	0.19	0.15	–0.03	–0.12	–0.08	0.04	0.22	0.26	–0.02	0.12	0.29	1	–0.46	–0.36	–0.41	–0.34
$B_{\gamma\gamma}/B_{ZZ}$	–0.53	–0.20	–0.26	–0.29	–0.18	0.02	–0.18	–0.21	–0.42	–0.38	–0.16	0.07	0.21	0.17	–0.16	–0.20	–0.20	–0.08	–0.13	–0.21	–0.46	1	0.27	0.41	0.41
$B_{b\bar{b}}/B_{ZZ}$	–0.19	–0.07	–0.09	–0.11	–0.04	0.01	–0.06	–0.06	–0.12	–0.12	–0.06	0.02	0.07	0.05	0.04	–0.61	–0.72	0.25	–0.26	–0.80	–0.36	0.27	1	0.18	0.15
B_{WW}/B_{ZZ}	–0.55	–0.09	–0.16	–0.15	–0.06	0.10	0.00	–0.03	–0.13	0.01	–0.31	–0.01	0.00	–0.03	–0.06	–0.12	–0.13	–0.02	–0.07	–0.14	–0.41	0.41	0.18	1	0.19
$B_{\tau^+\tau^-}/B_{ZZ}$	–0.24	–0.15	–0.15	–0.22	–0.20	–0.01	–0.06	–0.20	–0.42	–0.29	–0.06	0.06	0.17	0.04	–0.06	–0.10	–0.11	–0.02	–0.06	–0.12	–0.34	0.41	0.15	0.19	1

Figure 28: Correlation matrix for the measured values of the simplified template cross sections in each measurement region times the $H \to ZZ^*$ branching fraction in a model with finer granularity.

F Additional figures and results for interpretations in the κ framework

Figure 29 shows the same combined contours as shown in Figure 12, without the contours for the inputs analyses overlaid.

Figure 30 shows the observed and expected negative log-likelihood scans of the κ_V and κ_F parameters from a combined fit excluding searches for off-shell Higgs production and for Higgs decays into invisible final states. Figure 31 shows the observed and expected negative log-likelihood scans of the κ_V and κ_F parameters from a combined fit excluding searches for off-shell Higgs production and for Higgs decays into invisible final states. Figure 32 shows the observed and expected negative log-likelihood scans of the κ_g, κ_γ, B_{inv} and B_{undet} parameters from a combined fit including searches for Higgs decays into invisible final states. Figure 33 shows the negative log-likelihood contours at 68% and 95% CL in the (B_{inv}, B_{undet}) plane obtained in this model. Figure 36 shows the observed and expected negative log-likelihood scans of the B_{inv} and B_{undet} parameters from a combined fit including searches for Higgs decays into invisible final states using a generic coupling parametrization. Figure 37 shows the observed and expected negative log-likelihood scans of the B_{BSM} parameter from a combined fit including searches for off-shell Higgs production using a generic coupling parametrization.

Figures 34, 35, 38 and 39 provide the correlation matrices obtained in fits to data using the models described respectively in Sections 7.2, 7.3, 7.4, 7.5 and 7.6.

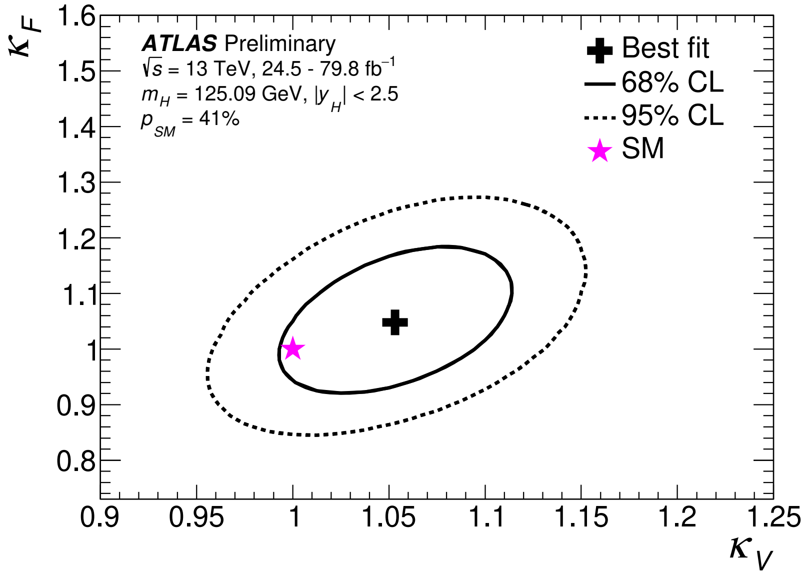

Figure 29: Observed contours at 68% and 95% CL in the (κ_{F}, κ_{V}) plane, defined in the asymptotic approximation by $-2\ln\Lambda = 2.28$ and 5.99, respectively. The cross indicates the best-fit value and the star the SM prediction.

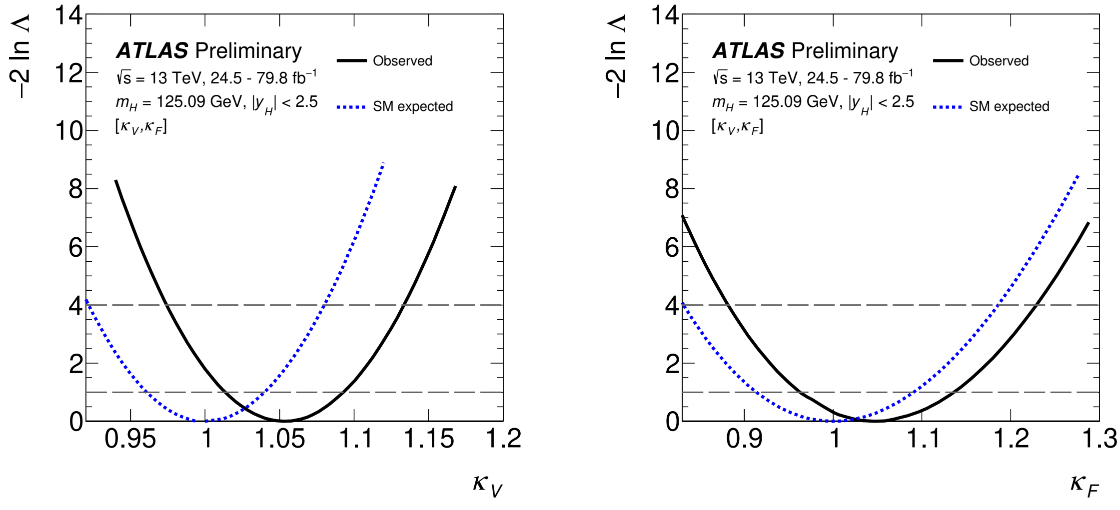

(a)

(b)

Figure 30: Observed (solid line) and expected (dotted line) negative log-likelihood scans of the (a) κ_V and (b) κ_F parameters from a combined fit excluding searches for off-shell Higgs production and for Higgs decays into invisible final states. All the other parameters of interest from the list in the legend are also varied in the minimization procedure. The dashed horizontal lines at $-2\ln\Lambda = 1$ ($-2\ln\Lambda = 4$) indicate the levels used to define the 1σ (2σ) confidence interval for the corresponding parameter, as described in Section 4.

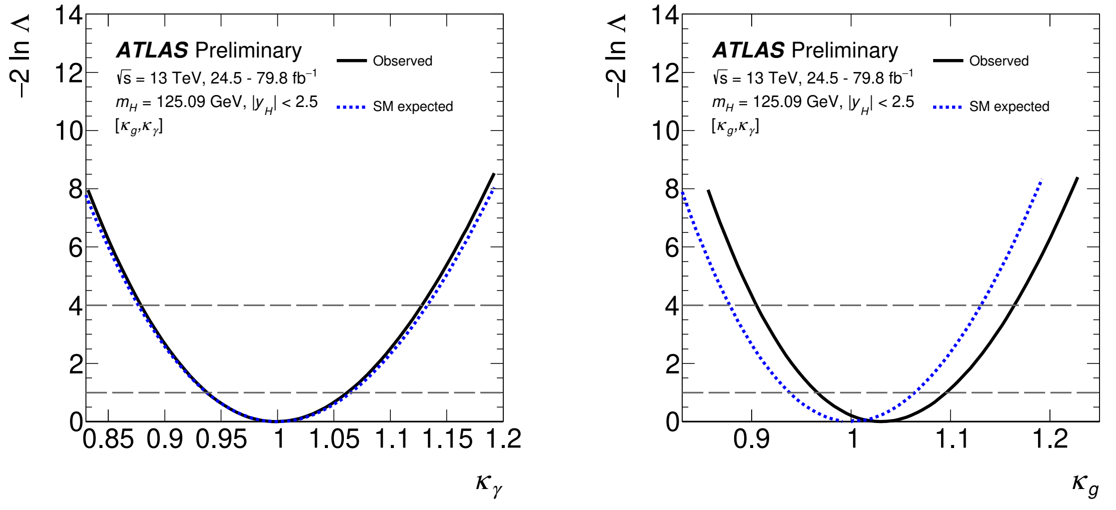

(a)

(b)

Figure 31: Observed (solid line) and expected (dotted line) negative log-likelihood scan of the (a) κ_γ and (b) κ_g parameters from a combined fit excluding searches for off-shell Higgs production and for Higgs decays into invisible final states. All the other parameters of interest from the list in the legend are also varied in the minimization procedure. The dashed horizontal lines at $-2\ln\Lambda = 1$ ($-2\ln\Lambda = 4$) indicate the levels used to define the 1σ (2σ) confidence interval for the corresponding parameter, as described in Section 4.

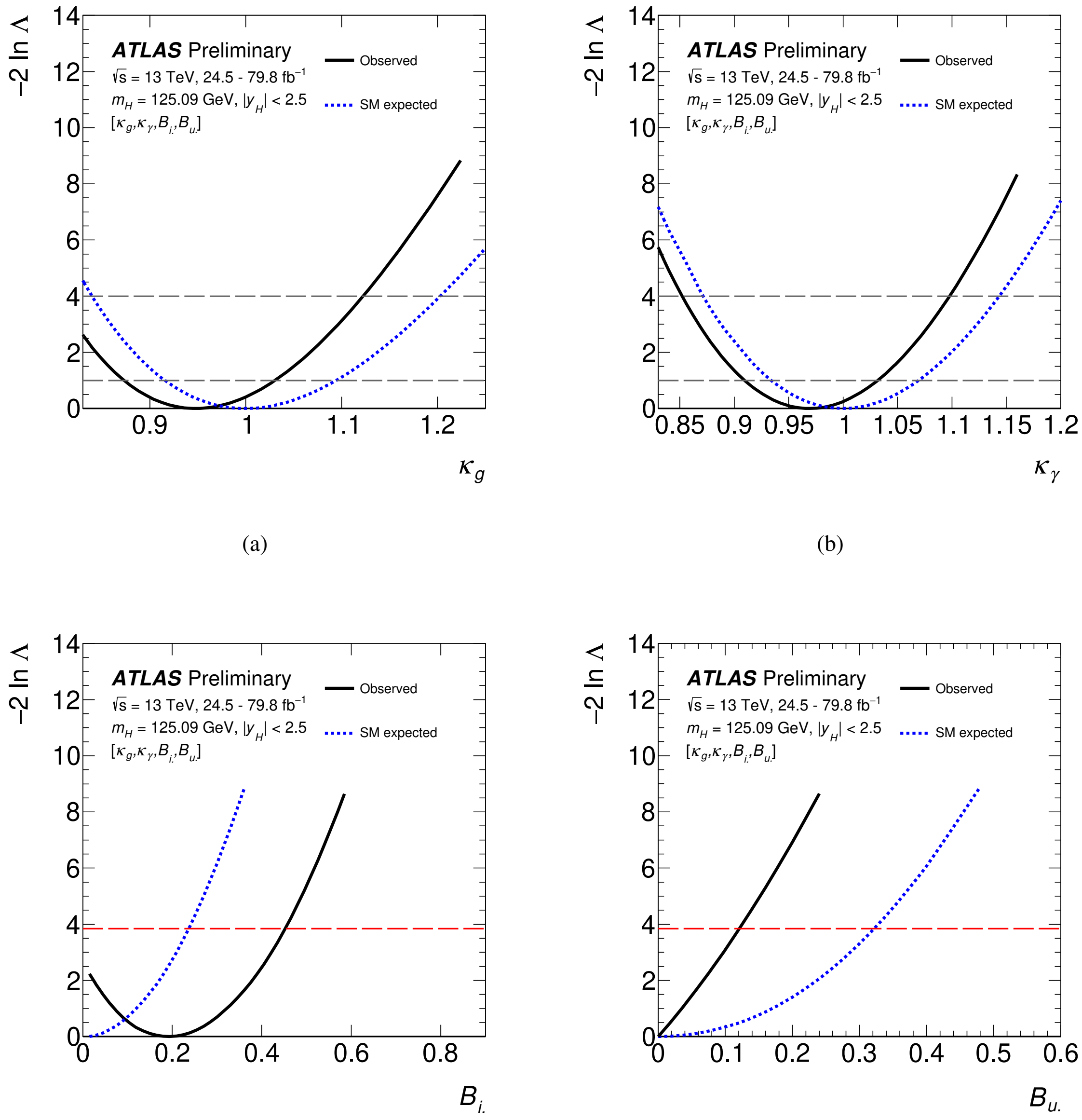

(a)

(b)

(c)

(d)

Figure 32: Observed (solid line) and expected (dotted line) negative log-likelihood scan of the (a) κ_g, (b) κ_γ, (c) $\mathrm{B}_{\mathrm{inv}}$ and (d) $\mathrm{B}_{\mathrm{undet}}$ parameters from a combined fit including searches for Higgs decays into invisible final states. All the other parameters of interest from the list in the legend are also varied in the minimization procedure. In (a) and (b), the dashed horizontal lines at $-2\ln\Lambda = 1$ ($-2\ln\Lambda = 4$) indicate the levels used to define the 1σ (2σ) confidence interval for κ_g and κ_γ, as described in Section 4. In (c) and (d), the dashed red line shows the level used to obtain the 95% CL upper limits on $\mathrm{B}_{\mathrm{inv}}$ and $\mathrm{B}_{\mathrm{undet}}$.

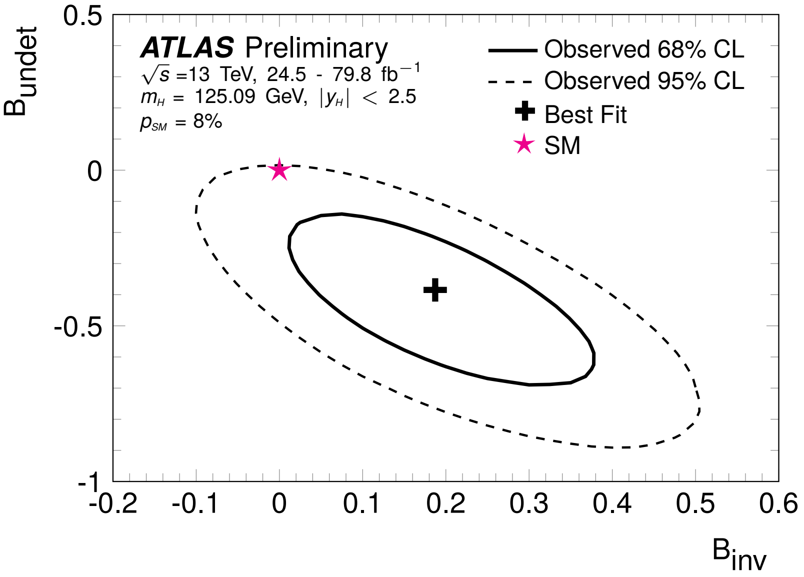

Figure 33: Negative log-likelihood contours at 68% and 95% CL in the (B_{inv}, B_{undet}) plane obtained in the model with BSM contributions to loop an decay processes described in the text. The κ_g and κ_γ parameters are profiled, while all other coupling strength modifiers are fixed to their SM values. The best fit value is indicated by a cross while the SM hypothesis is indicated by a star.

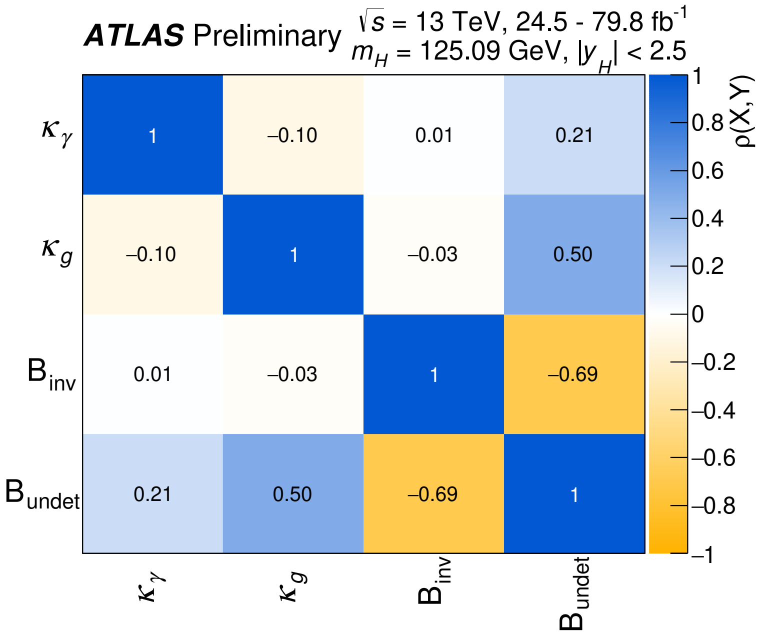

	κ_γ	κ_g	B_{inv}	B_{undet}
κ_γ	1	−0.10	0.01	0.21
κ_g	−0.10	1	−0.03	0.50
B_{inv}	0.01	−0.03	1	−0.69
B_{undet}	0.21	0.50	−0.69	1

Figure 34: Correlation matrix obtained in the fit to the data of a model that probes BSM contributions in loops and decays, with B_{BSM} included as a free parameter.

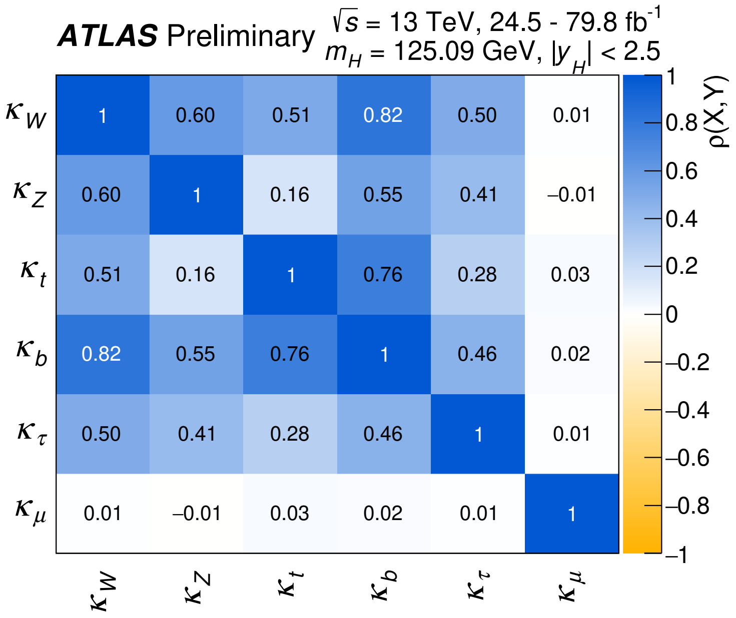

	κ_W	κ_Z	κ_t	κ_b	κ_τ	κ_μ
κ_W	1	0.60	0.51	0.82	0.50	0.01
κ_Z	0.60	1	0.16	0.55	0.41	−0.01
κ_t	0.51	0.16	1	0.76	0.28	0.03
κ_b	0.82	0.55	0.76	1	0.46	0.02
κ_τ	0.50	0.41	0.28	0.46	1	0.01
κ_μ	0.01	−0.01	0.03	0.02	0.01	1

Figure 35: Correlation matrix obtained in the fit to the data using a generic parametrization assuming no new particles in loops and decays.

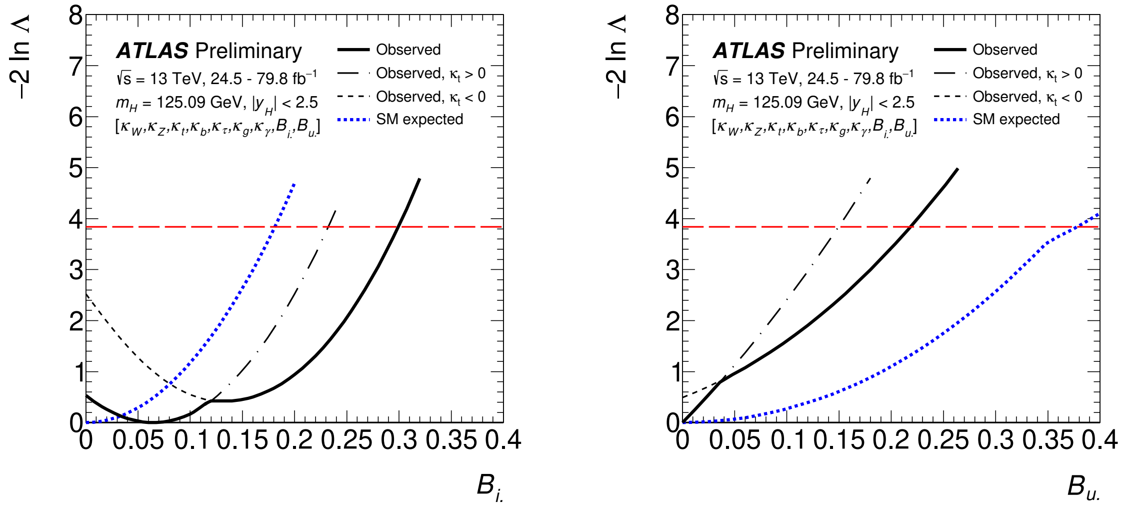

(a) (b)

Figure 36: Observed (solid line) and expected (dotted line) negative log-likelihood scan of the (a) B_{inv}, (b)B_{undet} parameters from a combined fit including searches for Higgs decays into invisible final states using a generic coupling parametrization. All the other parameters of interest from the list in the legend are also varied in the minimization procedure. The dashed red horizontal lines indicate the levels used to obtain the 95% CL upper limits on B_{inv} and B_{undet}, as described in Section 4.

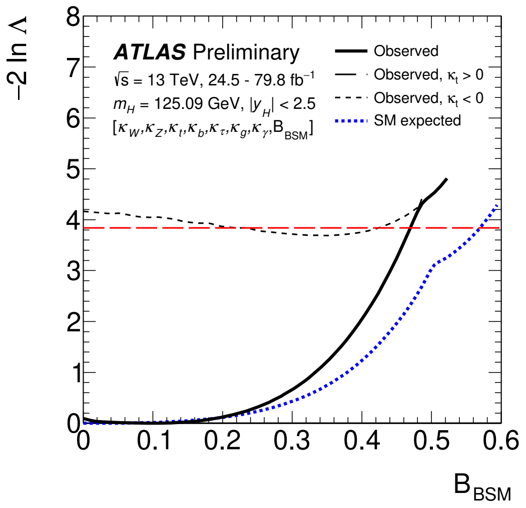

(a)

Figure 37: Observed (solid line) and expected (dotted line) negative log-likelihood scan of the B_{BSM} parameter from a combined fit including searches for off-shell Higgs production using a generic coupling parametrization. All the other parameters of interest from the list in the legend are also varied in the minimization procedure. The dashed red horizontal line indicates the level used to obtain the 95% CL upper limit on B_{BSM}, as described in Section 4.

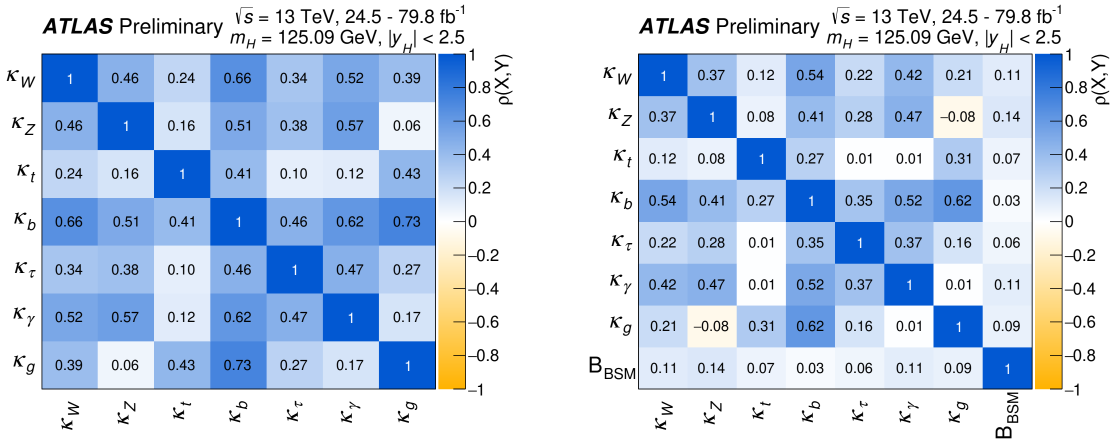

	κ_W	κ_Z	κ_t	κ_b	κ_τ	κ_γ	κ_g
κ_W	1	0.46	0.24	0.66	0.34	0.52	0.39
κ_Z	0.46	1	0.16	0.51	0.38	0.57	0.06
κ_t	0.24	0.16	1	0.41	0.10	0.12	0.43
κ_b	0.66	0.51	0.41	1	0.46	0.62	0.73
κ_τ	0.34	0.38	0.10	0.46	1	0.47	0.27
κ_γ	0.52	0.57	0.12	0.62	0.47	1	0.17
κ_g	0.39	0.06	0.43	0.73	0.27	0.17	1

(a)

	κ_W	κ_Z	κ_t	κ_b	κ_τ	κ_γ	κ_g	B_{BSM}
κ_W	1	0.37	0.12	0.54	0.22	0.42	0.21	0.11
κ_Z	0.37	1	0.08	0.41	0.28	0.47	−0.08	0.14
κ_t	0.12	0.08	1	0.27	0.01	0.01	0.31	0.07
κ_b	0.54	0.41	0.27	1	0.35	0.52	0.62	0.03
κ_τ	0.22	0.28	0.01	0.35	1	0.37	0.16	0.06
κ_γ	0.42	0.47	0.01	0.52	0.37	1	0.01	0.11
κ_g	0.21	−0.08	0.31	0.62	0.16	0.01	1	0.09
B_{BSM}	0.11	0.14	0.07	0.03	0.06	0.11	0.09	1

(b)

Figure 38: Correlation matrix obtained in the fit to the data using generic parameterizations including effective photon and gluon couplings with (a) $B_{inv} = B_{undet} = 0$ or (b) B_{inv} and B_{undet} included as free parameters, with the latter constrained using the off-shell analysis.

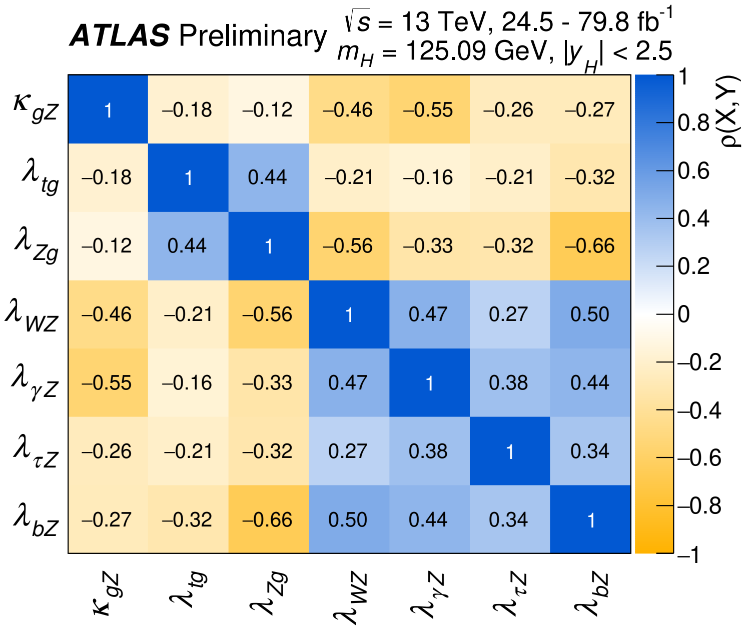

	κ_{gZ}	λ_{tg}	λ_{Zg}	λ_{WZ}	$\lambda_{\gamma Z}$	$\lambda_{\tau Z}$	λ_{bZ}
κ_{gZ}	1	−0.18	−0.12	−0.46	−0.55	−0.26	−0.27
λ_{tg}	−0.18	1	0.44	−0.21	−0.16	−0.21	−0.32
λ_{Zg}	−0.12	0.44	1	−0.56	−0.33	−0.32	−0.66
λ_{WZ}	−0.46	−0.21	−0.56	1	0.47	0.27	0.50
$\lambda_{\gamma Z}$	−0.55	−0.16	−0.33	0.47	1	0.38	0.44
$\lambda_{\tau Z}$	−0.26	−0.21	−0.32	0.27	0.38	1	0.34
λ_{bZ}	−0.27	−0.32	−0.66	0.50	0.44	0.34	1

Figure 39: Correlation matrix obtained in the fit to the data using a generic parameterization using ratios of coupling modifiers.

G Average number of SM Higgs bosons selected by input analyses from each fb^{-1} of 13 TeV data

Assume SM Higgs boson with $m_H = 125.09$ GeV, and all the nuisance parameters at nominal values, the average number of Higgs bosons selected by input analyses considered in this combination (except for $H \rightarrow$ invisible and Off-shell $H \rightarrow ZZ^* \rightarrow 4\ell$ and $H \rightarrow ZZ^* \rightarrow 2\ell 2\nu$) each fb^{-1} at 13 TeV is summarized in Table 16.

Table 16: Average number of SM Higgs bosons ($m_H = 125.09$ GeV) selected by input analyses considered in this combination (except for $H \rightarrow$ invisible and Off-shell $H \rightarrow ZZ^* \rightarrow 4\ell$ and $H \rightarrow ZZ^* \rightarrow 2\ell 2\nu$) from each fb^{-1} at 13 TeV. The numbers are reported for each main production mode as described in Section 5.2, as well as for each decay channel.

Decay	Total	ggF	VBF	WH	ZH	$t\bar{t}H$+tH
$H \rightarrow \gamma\gamma$	46.4	41.1	3.19	0.998	0.676	0.505
$H \rightarrow ZZ^*$	1.50	1.24	0.109	0.0316	0.0222	0.104
$H \rightarrow WW^*$	42.2	29.8	3.05	0.758	0.209	8.36
$H \rightarrow \tau\tau$	17.1	9.31	3.82	0.715	0.419	2.85
$H \rightarrow b\bar{b}$	66.0	9.68	9.68	4.81	6.30	35.5
$H \rightarrow \mu\mu$	6.67	5.96	0.474	0.143	0.0765	0.0112